NANYANG
TECHNOLOGICAL
UNIVERSITY

GROWTH AND FABRICATION OF INGAN/GAN LIGHT-EMITTING DIODES FROM PLANAR TO MICROWALL STRUCTURES: EPITAXIAL AND DEVICE DESIGNS, MODELLING AND CHARACTERIZATION

ZHU BINBIN

SCHOOL OF PHYSICAL AND MATHEMATICAL SCIENCES

2017

GROWTH AND FARICATION OF INGAN/GAN LIGHT-EMITTING DIODES ZHU BINBIN 2017

ZHU BINBIN

GROWTH AND FBRICATION OF INGAN/GAN LIGHT-EMITTING DIODES FROM PLANAR TO MICROWALL STRUCTURES: EPITAXIAL AND DEVICE DESIGNS, MODELLING AND CHARACTERIZATION

ZHU BINBIN

SCHOOL OF PHYSICAL ANDMATHEMATICAL SCIENCES

A thesis submitted to the Nanyang Technological University
in partial fulfilment of the requirement for the degree of
Doctor of Philosophy

2017

Acknowledgements

In the last four years, I am indebted to many people for their enthusiastic contribution to my research work. Without their help, my experience in NTU would not be so rewarding and unforgettable.

First, I want to express my wholehearted thanks to my supervisor, Prof. Hilmi Volkan Demir, who has given me constant insightful guidance with great patience and strong support during my PhD period. His great diligence, extreme enthusiasm, and steady efforts towards research have always been the inspiration and motivation for me.

Second, I want to thank my co-supervisor, Assoc Prof Xiong Qihua, who has given me experimental support, and Prof Sun Xiao Wei who has given me valuable suggestions on my research.

Then, I want to show my sincere gratitude to Dr Tan Swee Tiam and Dr Liu Wei. They have given me innovative inspiration, valuable suggestions and critical comments on my research, without which my PhD study would not be successful.

I also want to thank all my colleagues in our research group, Dr Kang Xuejun, Dr Ju Zhenggang, Dr Ji Yun, Dr Zhang Zihui, Dr Wang Liancheng, Dr Zabu Kyaw, Mr Zhang Xueliang, Mr Namig Hasanov, Mr Lu Shunpeng, and Mr Zhang Yiping, not only for their wholehearted support during experiments, but also for the fruitful discussion and valuable ideas from them, which made my research much easier.

Besides, I want to thank all the companions who have given me help on my research, Dr Yang Xuyong, Dr Wang Ning, Dr Wang Yue, Dr Chen Shi, Dr Liu Hongfei, Dr Xu Weigao, and Dr Zhao Xin, from whom I have learnt a lot during the experiment and discussion process.

I also want to show my gratitude to all the technicians, Ms Debbie Chia and Ms Vino Prabakaran from Luminous, Ms Chua Si Yun and Ms Selina Lee Shi Qin from PAP graduate office, Mr Mak Foo Wah, Mr. Mohamad Shamsul bin Mohamad, Mr. Soh Eng Hwa, and Ms. Chia Ai Lay Irene from N2FC-CR2, Dr Chong Gang Yih, Mdm Yang Xiaohong, Ms Ngo Ling Ling, and Mr Chung Kwok Fai from N2FC-CR1, Ms. Low Poh Chee, from Photonics Lab II and Mr Li Yuanqing from SPMS. Their professional support and continuous help have made my work move forward smoothly.

In addition to the above, I want to thank Nanyang Technological University for her scholarship, without which my PhD experience during the last four years would not be possible.

Last but not the least, I want to thank my families and friends for their love and encouragement. Especially for my parents, they never put too much pressure on me and gave me constant encouragement. I also want to thank my girlfriend Miao Huihui, who has accompanied and encouraged me during my research life.

TABLE OF CONTENTS

ACKNOWLEDGEMENTS I

LIST OF ABBREVIATIONS VII

LIST OF FIGURES........ IX

LIST OF TABLES XV

ABSTRACT........ XVI

CHAPTER 1 INTRODUCTION 1

1.1 HISTORY OF INGAN/GAN LIGHT-EMITTING DIODES (LEDS)........ 2
1.2 III-NITRIDE SEMICONDUCTOR MATERIALS AND LEDS 3
1.2.1 Properties of III-nitride materials 3
1.2.2 Advantages for III-nitride LEDs........ 10
1.2.3 Applications for III-nitride LEDs 12
1.2.4 Challenges for III-nitride LEDs........ 14
1.3 RESEARCH MOTIVATION AND OBJECTIVES........ 14
1.4 THESIS ORGANIZATION........ 15

CHAPTER 2 PHYSICAL PHENOMENA AND CONCEPTS FOR LEDS........ 18

2.1 RECOMBINATION MECHANISM IN LEDS 19
2.1.1 Radiative recombination........ 19
2.1.2 Shockley-Read-Hall (SRH) recombination 20
2.1.3 Auger recombination 20
2.2 EFFICIENCY DROOP IN LEDS 21
2.3 TUNNEL JUNCTION IN LEDS 22
2.4 REFLECTIVE OHMIC CONTACT IN LEDS........ 22

CHAPTER 3 EPITAXIAL GROWTH AND DESIGNS OF INGAN/GAN LEDS 24

3.1 EPITAXIAL GROWTH TECHNIQUES USING MOCVD 25
3.1.1 Epitaxy with MOCVD........ 25
3.1.2 Wafer-scale epitaxial material characterization 27
3.2 EPITAXIAL DESIGN USING TANDEM LEDS WITH TUNNEL JUNCTION 29

3.2.1 Introduction 29
3.2.2 Modeling...30
3.2.3 Results and discussions 30
3.2.4 Conclusions 34
3.3 EPITAXIAL DESIGN USING DOPED BARRIERS 34
3.3.1 Introduction 34
3.3.2 Experiments..35
3.3.3 Results and discussions 37
3.3.4 Conclusions 41
3.4 SUMMARY 41
CHAPTER 4 FABRICATION AND DEVICE DESIGNS OF LEDS............................43
4.1 DEVICE STRUCTURE FABRICATION AND CHARACTERIZATION.................................44
4.1.1 Device fabrication...44
4.1.2 Device characterization 48
4.2 DEVICE DESIGN USING DECOUPLED CONTACT AND MIRROR 52
4.2.1 Introduction 52
4.2.2 Experiments..53
4.2.3 Results and discussions 54
4.2.4 Conclusions 62
4.3 DEVICE DESIGN USING MODULATED OHMIC CONTACT 63
4.3.1 Introduction 63
4.3.2 Experiments..64
4.3.3 Results and discussions 65
4.3.4 Conclusions 74
4.4 SUMMARY 75
CHAPTER 5 DEVELOPMENT TOWARDS INGAN/GAN-BASED MICROWALL LEDS 76
5.1 MICROWALL STRUCTURED LEDS GROWN BY SELECTIVE-AREA GROWTH 77
5.2 STRUCTURAL AND OPTICAL PROPERTIES OF MICROWALLS 78
5.2.1 Introduction 78
5.2.2 Experiments..79

5.2.3 Results and discussions 81
5.2.4 Conclusions 90
5.3 SEMI-POLAR MICROWALLS 90
5.3.1 Introduction 90
5.3.2 Experiments 91
5.3.3 Results and discussions 91
5.3.4 Conclusions 93
5.4 SUMMARY 93
CHAPTER 6 CONCLUSIONS AND FUTURE PLAN 94
6.1. CONCLUSIONS 95
6.2. FUTURE PLAN 96
APPENDIX A EPITAXIAL GROWTH, MATERIAL CHARACTERIZATION AND NUMERICAL SIMULATION FOR INGAN/GAN-BASED LIGHT-EMITTING DIODES 98
A.1 METAL-ORGANIC CHEMICAL VAPOR DEPOSITION (MOCVD)..................................99
A.1.1 Reaction precursors 100
A.1.2 Gas diagram and handling system 101
A.1.3 Chamber design 105
A.1.4 Growth mechanism and reaction process 106
A.1.5 In-situ reflectance monitor...107
A.2 MATERIAL CHARACTERIZATION TECHNIQUES 110
A.2.1 Scanning electron microscopy (SEM)...110
A.2.2 Atomic force microscopy (AFM)...111
A.2.3 High-resolution x-ray diffraction (HRXRD)..111
A.2.4 Photoluminescence (PL) spectroscopy..112
A.2.5 Raman spectroscopy 112
A.2.6 Secondary ion mass spectroscopy (SIMS) 113
A.2.7 X-ray photoelectron spectroscopy (XPS)...113
A.3 NUMERICAL SIMULATION TECHNIQUE 114
A.3.1 Advanced physical models of semiconductor devices (APSYS) 114

LIST OF PUBLICATIONS..115

BIBLIOGRAPHY 119

List of Abbreviations

2D	2 Dimensional
3D	3 Dimensional
°C	Degree centigrade
AFM	Atomic Force Microscopy
AlGaN	Aluminum Gallium Nitride
BSF	Basal-plane Stacking Faults
Cp_2Mg	Bis-cyclopentadienyl Magnesium
CVD	Chemical Vapor Deposition
EQE	External Quantum Efficiency
EL	Electroluminescence
FWHM	Full Width at Half Maximum
GaN	Gallium Nitride
H_2	Hydrogen
HRXRD	High-Resolution X-Ray Diffraction
HT	High Temperature
HVPE	Hydride Vapor Phase Epitaxy
ICP	Inductively Coupled Plasma
IQE	Internal Quantum Efficiency
InGaN	Indium Gallium Nitride
LED	Light-Emitting Diode
MFC	Mass Flow Controller
MOCVD	Metal-Organic Chemical Vapor Deposition

MQWs	Multiple Quantum Wells
N_2	Nitrogen
NBE	Near Band Emission
NH_3	Ammonia
PECVD	Plasma-Enhanced Chemical Vapor Deposition
PL	Photoluminescence
QCSE	Quantum Confined Stark Effect
RIE	Reactive Ion Etching
RT	Room Temperature (300 K)
SAG	Selective Area Growth
SEM	Scanning Electron Microscopy
SiH_4	Silane
SIMS	Secondary Ion Mass Spectroscopy
SiN_x	Silicon Nitride
SSL	Solid-State Lighting
TCL	Transparent Conductive Layer
TD	Threading Dislocation
TEGa	Tri-ethyl Gallium
TMAl	Tri-methyl Aluminum
TMGa	Tri-methyl Gallium
TMIn	Tri-methyl Indium
XPS	X-ray Photoelectron Spectroscopy

List of Figures

Figure 1.1 Band gap, emission wavelength and lattice constant of III-nitride semiconductors at room temperature. [25] 5

Figure 1.2 Crystal structures for hexagonal III-nitride semiconductors (GaN), with atom arrangement along (a) [0001] and (b) [000-1] directions. [27]....................6

Figure 1.3 Generation of (a) compressive strain for InGaN, and (b) tensile strain for AlGaN, when the layer is grown on top of GaN substrate.....................7

Figure 1.4 Surface charges, direction of electric field and polarization field for spontaneous and piezoelectric polarizations in III-nitrides with both Ga and N faces. [29]....................7

Figure 1.5 Schematic band diagrams for (a) polarized and (b) non-polarized InGaN/GaN-based quantum well along C+ direction. 8

Figure 1.6 Longitudinal piezoelectric field in strained InGaN on GaN with different indium components under different polar angles from (0001). 9

Figure 1.7 Luminous efficiency of different lighting sources. [34]....................10

Figure 1.8 Total U.S. Lighting Energy Consumption Forecast, 2010 to 2030. [35] 11

Figure 1.9 Creating white light by three different techniques for LED. [37] 12

Figure 1.10 Applications of LEDs in indoor lighting, building lighting, traffic signals, automobile lights, and displays. [38-42]....................13

Figure 1. 11 Emerging applications of LEDs used in the fields of (a) horticulture [36] and (b) Li-Fi [45]....................13

Figure 2.1 Lattice models for (a) radiative recombination and non-radiative recombination.[29]....................20

Figure 3.1 (a) Typical as-grown InGaN/GaN-based LED epi-wafer achieved in my work, and the appearance after it is lighted up, (b) electroluminescence spectrum for the grown sample and (c) the wafer-scale output power and EQE versus current. 27
Figure 3.2 (a) wafer thickness and (b) PL peak wavelength mapping................................28
Figure 3.3 HRXRD rocking curves for LEDs along (a) the symmetrical (002) and asymmetrical (102) reflection planes. 29
Figure 3.4 (a) Schematic device structures for simulation, (b) output power density and (c) forward voltage vs. current density for all the simulated devices.......................................32
Figure 3.5 Distribution of carrier concentration at current density of 100 A/cm^2: electron concentration for the whole structure (a), first active region (b), and second active region(c), hole concentration for the whole structure (d), first active region (e), and second active region (f)...33
Figure 3.6 Electric field profile calculated across the tunnel junction from p+-GaN...........34
Figure 3.7 Schematic diagrams for studied LED structures, in which LED A is the reference and LED B is the sample with Mg doping in the quantum barriers. 37
Figure 3.8 *I-V* characteristics under temperatures from 25 °C to 150 °C for (a) LED A and (b) LED B. 38
Figure 3.9 (a) Capacitance-Voltage characteristics, and (b) simulated *I-V* characteristics for both samples at room temperature. 40
Figure 3.10 Measured forward voltage at different injection currents vs hot plate temperature, for (a) LED A and (b) LED B, with the dashed lines as linear fit for all the experimental data. 41
Figure 4.1 Schematic structure of top-up structure LED. 45
Figure 4.2 Process flow for top-up structure LED fabrication. 45

Figure 4.3 Schematic structure of flip-chip structure LED...46

Figure 4.4 Process flow for flip-chip structure LED fabrication...46

Figure 4.5 Schematic structure of vertical structure LED. 48

Figure 4.6 Process flow for vertical structure LED fabrication...48

Figure 4.7 (a) the appearance of fabricated device with top-up structure, before and after being lighted up, (b) *I-V* characteristics, (c) output power and EQE for the fabricated device. 49

Figure 4.8 (a) the appearance of fabricated flip-chip structure, before and after being lighted up, (b) *I-V* characteristics, (c) output power and EQE for the fabricated devices. 50

Figure 4.9 (a) the appearance of fabricated vertical structure LED, before and after being lighted up, (b) *I-V* characteristics, (c) output power and EQE for the fabricated devices. ...51

Figure 4.10 SEM images of the samples with a thin annealed (a) Ni (1 nm)/Ag (0 nm), (b) Ni (1 nm)/Ag (1 nm), (c) Ni (1 nm)/Ag (3 nm), and (d) Ni (1 nm)/Ag (5 nm) contact layer on top. 55

Figure 4.11 SEM images of the samples with (a) conventional mirror and (b) proposed mirror with annealed Ni (1 nm)/Ag (1 nm) as contact layer, and SIMS depth profiles of the samples with (c) conventional mirror and (d) proposed mirror with annealed Ni(1nm)/Ag(1nm) as contact layer. 56

Figure 4.12 Illustration for one-step mirror and decoupled mirror......................................57

Figure 4.13 Reflectivity measured for the samples of the conventional contact mirror and the decoupled contact mirrors with thin annealed layer of Ni (1 nm)/Ag(1 nm), Ni (1 nm)/Ag (3 nm) and Ni (1 nm)/Ag (5 nm), respectively. 58

Figure 4. 14 Output power measured for LEDs with the conventional contact mirror and the decoupled contact mirrors with thin annealed layer of Ni (1 nm)/Ag (1 nm), Ni (1 nm)/Ag (3

nm) and Ni (1 nm)/Ag (5 nm), respectively. 58

Figure 4.15 Current-voltage (I-V) curves measured for the LEDs with the conventional contact mirror and the decoupled contact mirrors with thin annealed layer of Ni (1 nm)/Ag (1 nm), Ni (1 nm)/Ag (3 nm) and Ni (1 nm)/Ag (5 nm), respectively. The intercepts of the dashed lines on the X-axis indicate the turn-on voltages..59

Figure 4.16 SIMS depth profiles of the decoupled contact mirrors with thin annealed layer of (a) Ni (1 nm)/Ag (1 nm), (b) Ni (1 nm)/Ag (3 nm) and (c) Ni (1 nm)/Ag (5 nm), respectively. 62

Figure 4.17 (a) Reflectivity for ITO thin layers with different thicknesses after annealing and silver mirror deposition and (b) *I-V* curve of flip-chip LEDs with different thicknesses of ITO. 66

Figure 4.18 (a) Optical output power and (b) wall-plug efficiency enhancement ratio for samples with different ITO layers when compared with the reference, with inset showing the same curve at low current range from 30 mA to 100 mA. 67

Figure 4.19 AFM images of p-GaN surface after ITO deposition with 1 nm ITO (a) before and (d) after annealing, 5 nm ITO (b) before and (e) after annealing, 10 nm ITO (c) before and (f) after annealing..69

Figure 4.20 XPS wide scan of all the elements (a), Ga 2p core spectra (b), N 1s core spectra (c) and In 3d core spectra (d) for the samples with different ITO thickness after annealing. 72

Figure 4.21 Schematic diagrams of element mixing for contact mirror with (a) no ITO layer, (b) 1 nm annealed ITO layer, with a formation of island-like $InGa_xN_yO_z$ layer, (c) 5 nm annealed ITO layer, with a formation of $InGa_xN_yO_z$ layer, and (d) 10 nm annealed ITO layer. 73

Figure 4.22 Schematic band diagrams of silver and p-GaN contact with (a) no interfacial layer, and (b) $InGa_xN_yO_z$ interfacial layer. 74

Figure 5.1 Selective area growth of GaN. [121] 78

Figure 5.2 Schematic illustration of the process used to prepare the starting substrates for GaN microwall growth. 80

Figure 5.3 SEM images grown by continuous MOCVD techniques under different temperatures for both top views at (a) 1135 ℃, (b) 1185 ℃, (c) 1235 ℃, (d) 1285 ℃ and cross section views at (e) 1135 ℃, (f) 1185 ℃, (g) 1235 ℃, (h) 1285 ℃. 82

Figure 5.4 Raman spectrum of E_2 (high) phonon peaks for samples grown at (a) 1135℃, (b) 1185℃, (c) 1235℃ and (d) 1285 ℃ respectively. 84

Figure 5.5 HRXRD rocking curves of (a) the symmetrical (002) reflection and (b) the asymmetrical (102) reflection planes for GaN microwalls grown at temperature of 1185 ℃ and 1285 ℃. 85

Figure 5.6 Room temperature photoluminescence for samples grown under different temperatures, with planar structure grown as reference. 86

Figure 5.7 SEM images grown by continuous MOCVD techniques under different NH_3 flow rates for both top view (a) 400 sccm, (b) 700 sccm, (c) 1000 sccm, (d) 4000 sccm and cross section view (e) 400 sccm, (f) 700 sccm, (g) 1000 sccm, (h) 4000 sccm. 87

Figure 5. 8 Raman spectra of E2 (high) phonon peaks for samples grown with NH_3 at (a) 400 sccm, (b) 700 sccm, (c) 1000 sccm and (d) 4000 sccm, respectively. 88

Figure 5.9 HRXRD rocking curves of (a) the symmetrical (002) reflection and (b) the asymmetrical (102) reflection planes for GaN microwalls grown under flow rate of NH_3 at 4000 sccm and 400 sccm. 89

Figure 5.10 Room-temperature photoluminescence for all the samples with different NH_3 flow rates....90

Figure 5.11 SEM morphologies for the grown semi-polar microwall structures, from (a) the top view and (b) the cross section view....92

Figure 5.12 Electroluminescence of as-grown microwall LED, with inset showing the lighted up appearance at two different positions....93

Figure. A1 Appearance of 3×2″ AIXTRON CCS MOCVD system in our group....100

Figure. A2 Gas diagram for III-nitride material growth. [157]....103

Figure. A3 Gas lines for an MO source with double dilution. [157]....104

Figure. A4 (a) The cross section and (b) the detailed view for the showerhead, (c) the holder for substrates. [157]....105

Figure. A5 Tungsten filament for substrate heating, with three colors denoting three heating zones. [157]....106

Figure. A6 General reaction process in MOCVD. [159]....106

Figure. A7 Schematic diagram for the setup of interferometer....108

Figure. A8 Variation of reflectivity with time for the deposition of GaN on sapphire.[161]....109

Figure. A9 AFM images of GaN film at different growth stages. [161]....110

Figure. A10 Typical rocking curves of GaN measured along (a) (002) and (b) (102) reflection planes....112

List of Tables

Table 1.1 Lattice constants, thermal expansion, thermal conductivity and melting point for III-nitride materials, and growth substrates including sapphire, 6H-SiC and Si (111)...........4

Table 3.1 Growth parameters during the whole process for all the layers 26

Table 4. 1 Sheet square resistance of thin contact layers on top of p-GaN before and after annealing (Ω/□). 62

Table 4.2 Sheet resistance of ITO layers on top of p-GaN before and after annealing (Ω/□). 70

Table 5.1 Sets of experiments carried out and parameters used in this work. 81

Abstract

InGaN/GaN-based light-emitting diodes (LEDs) are gradually replacing traditional lighting techniques, such as incandescent and fluorescent lamps. They have many advantages, such as high efficiency, long lifespan, compact size and color diversity. However, their efficiency decreases substantially with increasing current, which is due to the efficiency droop. Although the exact reasons accounting for the efficiency droop are still under debate, some proposals have been put forward to explain this phenomenon. Auger recombination is identified as one of the most critical reasons, since it is the cube of carrier concentration and gradually dominates with increasing current. Polarization effect, electron overflow and poor hole injection efficiency are also considered as the most critical reasons for causing the efficiency droop.

In order to address the problem of efficiency droop and improve the device performance, this thesis has systematically reported the investigation on the InGaN/GaN-based LEDs, mainly from the following three parts.

In the first part, the effort has been focused on the layer structures and doping profile in the quantum barriers for the LED epi-wafers. In our group, a platform of high quality epitaxial growth and versatile characterization methods has been established which provides the guarantee to the reliability and repeatability of the results. As a novel design of epi-wafers, the tandem LEDs, in which multiple active regions are connected by tunnel junctions, have been studied theoretically in both optical and electrical aspects. The simulated results show extraordinary efficiency improvement when compared with the traditional LEDs, which is attributed to a relatively reduced forward voltage and more uniform carrier distribution. Then, both experimental and simulated investigations have been conducted on the devices

with Mg doping in the barriers. In this work, the devices with Mg doped barriers show reduced forward voltage and improved electrical thermal stability when compared with the reference without doping. The mechanism for the superior electrical performance achieved in the control devices is due to the reduced depletion length and relatively increased acceptor concentration.

In the second part, based on the standard fabrication process for the three commonly used LED structures, which can achieve decent optical and electrical properties, the focus is put on the improvement of the mirror performance of the flip-chip structure LEDs. Two methods are proposed to improve its property in this thesis. One is the decoupled contact mirror, which is realized through two-step deposition method. The ohmic contact is firstly formed by depositing and annealing an extremely thin layer of Ni/Ag on top of p-GaN. The mirror construction is then carried out by depositing thick layer of Ag/Ti/Au without any subsequent annealing. Compared with the conventional mirror fabrication techniques, the optical output power is improved by more than 70% at 350 mA without compromising the electrical performance. Another method is through modulating the surface component of p-GaN. We report the improved performance of InGaN/GaN-based LEDs through the design and formation of $InGa_xN_yO_z$ interfacial layer, which maintains high reflectivity of silver and forms good ohmic contact between pristine silver and p-GaN. The interfacial layer was designed and formed by depositing a thin layer of indium tin oxide (ITO) on top of p-GaN, followed by thermal annealing to enable the inter-diffusion and inter-mixing of In, Sn, Ga, O and N atoms. Both electrical and optical performances of the LED with the optimized $InGa_xN_yO_z$ interfacial layer are improved, thus achieving the highest wall-plug efficiency compared to those LEDs with common ITO layer or without ITO layers at operation current.

In the third part, microwall LEDs, which expose different crystal facets, are

epitaxially grown by the MOCVD system. GaN microwalls with different morphologies are achieved through modifying growth temperature and NH_3 flow rate on c-plane sapphire substrates, which are characterized by a series of techniques. As indicated from the characterization results, the strain is determined by different plane facets, the defects are mainly determined by the growth temperature, and the optical quality is determined by both of the growth temperature and NH_3 flow rate. After the optimization of GaN microwall structures, a full structure microwall LED is grown and some preliminary results are achieved, which is a good start for future work.

In summary, the thesis has reported the detailed study on InGaN/GaN-based LEDs systematically, from planar structure growth and typical fabrication methods, to novel structure design and characterization. The performance of the proposed samples always showed superior properties in both optical and electrical aspects. This thesis provides new ideas about growth, fabrication and design techniques, which makes a big step forward to realize the high efficiency InGaN/GaN-based LEDs.

Chapter 1

Introduction

1.1 History of InGaN/GaN light-emitting diodes (LEDs)

Gallium nitride (GaN) was firstly synthesized in powder form by Johnson et al. in 1932 [1], which was formed through reacting metallic Ga with NH_3 gas. After the first synthesis of GaN, little attention was paid to this promising optoelectronic material until the epitaxial growth technology was developed for which high quality films could be grown on appropriate substrates. In 1969, the first GaN film was epitaxially grown by hydride vapor phase epitaxy (HVPE) on sapphire substrate [2]. However, the as-grown samples were all unintentionally n-doped with electron concentrations ranging from 10^{18} to 10^{20} cm^{-3}. The most persuasive explanation for the high background doping was the incorporation of oxygen atoms during the growth process [3, 4]. In order to achieve p-n junction by GaN material, p-GaN was required and the magnesium (Mg) was proposed as the p-dopant [5, 6]. Maruska et al. grew the first GaN-based LED by HVPE in 1972 with emitting wavelength at 430 nm [7]. This result laid the foundation for the modern GaN-based LEDs. During the following two decades, GaN film with high crystal quality was required to achieve better performance LEDs. However, there was no breakthrough achieved until the appearance of modern growth techniques, such as metal-organic chemical vapor deposition (MOCVD). In order to improve the crystal quality, a low temperature AlN [8] or GaN [9] buffer layer was required to grow on top of sapphire substrates, after which we could achieve the high-quality GaN. Concerning about p-type doping, it was very difficult to detect any positive carriers into GaN during the MOCVD growth, and the p-GaN was highly resistive, even a large amount of Mg atoms were incorporated. The reason for the above two phenomena were due to the formation of Mg:H complexes and high acceptor activation energy [10]. In 1989, Amano et al. [11] happened to find the resistivity and hole concentration of as-grown p-GaN was greatly improved after treated with low-energy electron beam irradiation (LEEBI) and high-efficiency GaN-based

LED was made possible. In 1992, Nakamura et al. [12] achieved p-GaN films using post-thermal annealing process in N_2 ambient. A hole concentration as high as 3×10^{17} cm^{-3} was achieved with a resistivity of only 2 Ω·cm. These advances led to the realization of the first commercial GaN-based p-n junction LED in 1993 [13]. Finally, Nakamura demonstrated high-brightness blue, green, and yellow LEDs with InGaN quantum-well (QW) structures in 1995 [14], which was the basis for the state-of-the-art InGaN/GaN-based LED technology.

1.2 III-nitride semiconductor materials and LEDs

Group III-nitride compounds are semiconductors, including aluminum nitride (AlN), gallium nitride (GaN), indium nitride (InN), their ternary alloys and quaternary alloys, which are the most promising candidates for optoelectronic application. In the following part, properties of III-nitride materials, advantages and challenges of III-nitride LEDs are discussed in detail.

1.2.1 Properties of III-nitride materials

1.2.1.1 Physical properties

There are three different crystal structures found in III-nitride materials, which are zincblende, rock salt and wurtzite structures [15]. Among them, wurtzite structure exists in thermal dynamic stable state, which is predominantly used in solid-state lighting applications [16, 17]. In order to grow high-quality III-nitride films, the lattice structure for the substrate should be coincident and both lattice constant and thermal expansion coefficient should be comparable. Besides, properties of substrates, including surface finish, composition, reactivity, chemical, thermal, and electrical properties, are important in determining the quality of the epitaxial layers [18].

Below in Table 1.1 shows the commonly used physical parameters for III-nitride materials and related growth substrates.

Table 1.1 Lattice constants, thermal expansion, thermal conductivity and melting point for III-nitride materials, and growth substrates including sapphire, 6H-SiC and Si (111).

Material	Lattice constant [10^{-10} m]	Thermal expansion [$10^{-6}K^{-1}$]	Thermal conductivity [W $cm^{-1}K^{-1}$]	Melting point [K]
InN	a=3.54 [19]	5.7	0.8	1373 [20]
	c=5.705	3.7		
GaN	a=3.189	5.59	1.3	2791 [17]
	c=5.185	3.17		
AlN	a=3.112	4.15 [21]	2.0	3487
	c=4.982	5.27 [21]		
Sapphire	a=4.758 [22]	7.5	3.5	2303
	c=12.991	8.5		
6H-SiC	a=3.08	4.2	4.9	3102
	c=15.12	4.68		
Si (111)	a_{111}^{**}=3.84	2.6	1.3	1412

1.2.1.2 Bandgap properties

All of III-nitride materials have direct band gap with the value ranging from 0.7 eV (InN), through 3.4 eV (GaN) to 6.2 eV (AlN) [23, 24]. The formed ternary and quaternary alloys can span the whole visible spectrum, extending into the infrared and ultraviolet (UV) region, from 1.7 μm to 200 nm, as shown in Figure 1.1. Therefore, the emitting wavelength can be precisely controlled by changing the alloy components, which makes them ideal candidates for optoelectronic devices.

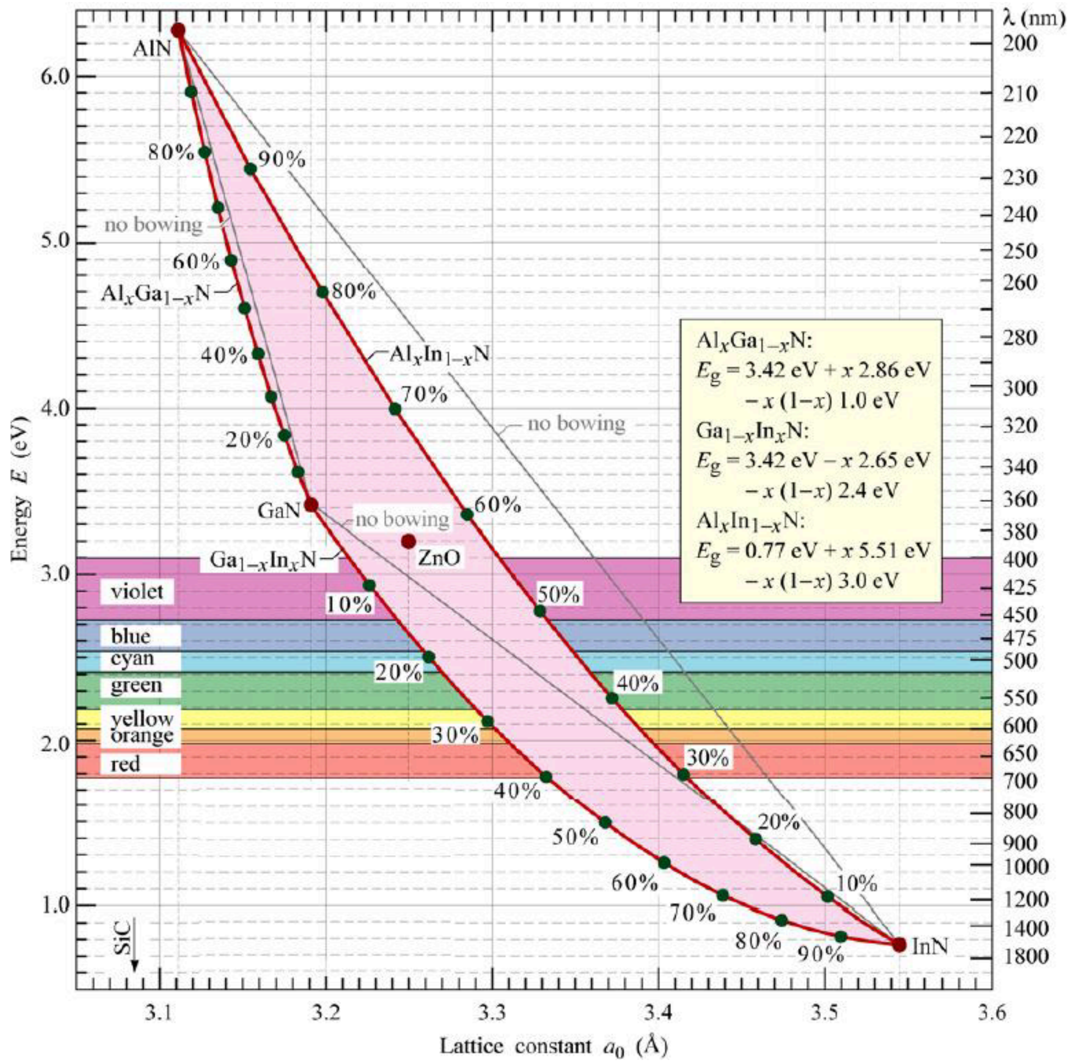

Figure 1.1 Band gap, emission wavelength and lattice constant of III-nitride semiconductors at room temperature. [25]

1.2.1.3 Polarization effect

When the III-nitride semiconductor materials are grown by MOCVD system on the above stated substrates as shown in Table 1.1, they crystallize in hexagonal wurtzite phase, as shown in Figure 1.2 with GaN as an example. Gallium and nitrogen atoms are arranged layer by layer, and thus the spontaneous polarization is generated along the growth direction [26].

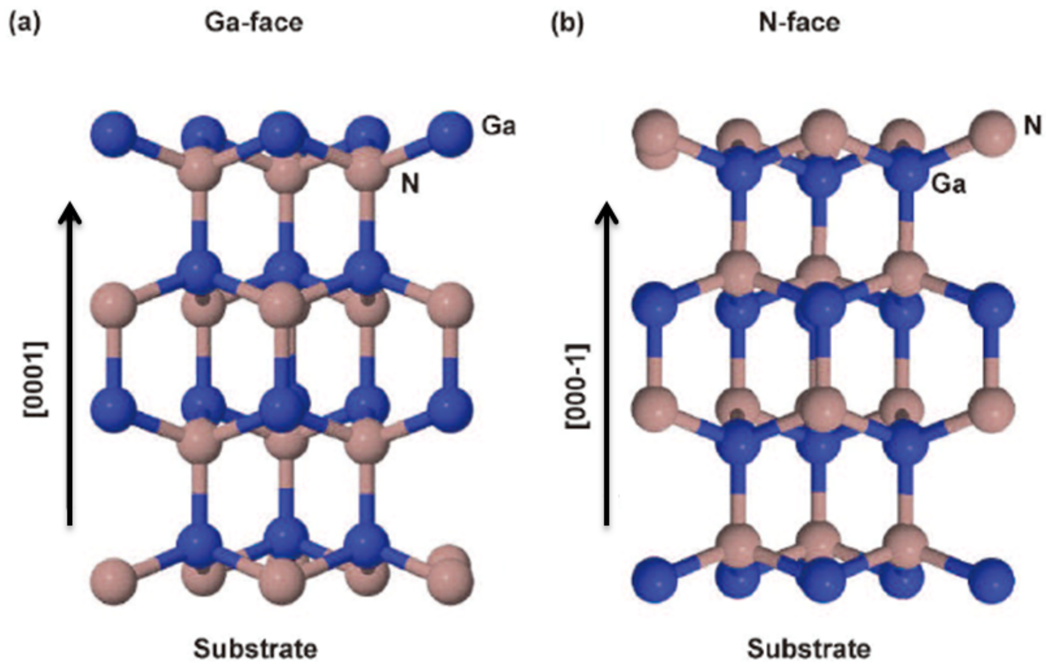

Figure 1.2 Crystal structures for hexagonal III-nitride semiconductors (GaN), with atom arrangement along (a) [0001] and (b) [000-1] directions. [27]

Besides the spontaneous polarization, there still exists piezoelectric polarization caused by biaxial stress [28]. When grown on bulk GaN substrate, the InGaN has larger lattice constant and is under compressive strain, while the AlGaN has smaller lattice constant and is under tensile strain, as shown in Figure 1.3. Thus, the piezoelectric polarization is generated due to the generation of strain in the growth process.

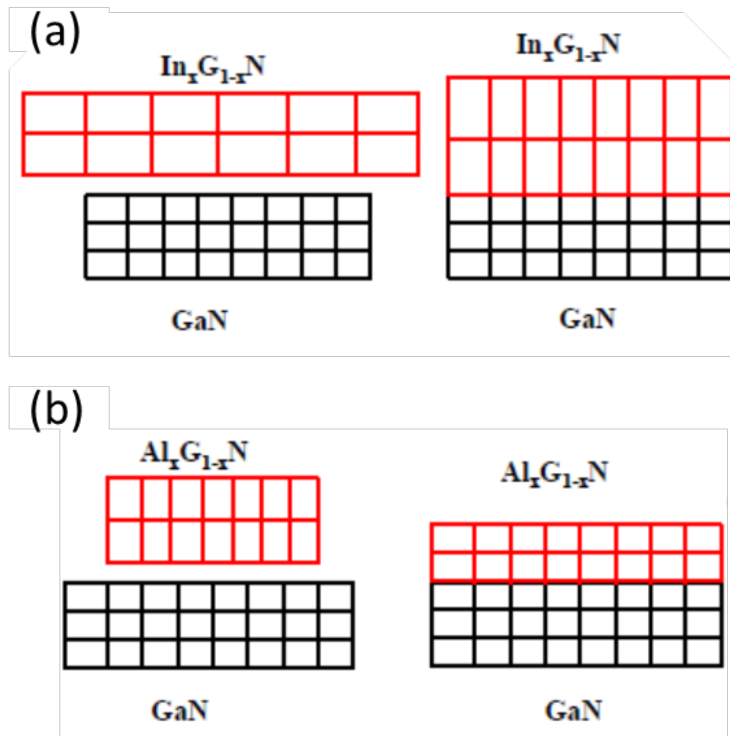

Figure 1.3 Generation of (a) compressive strain for InGaN, and (b) tensile strain for AlGaN, when the layer is grown on top of GaN substrate.

For both of the spontaneous and piezoelectric polarizations, the polarized charges are accumulated at the material interfaces. The direction of internal polarized electric field is determined by both the strain and growth direction, which is summarized in Figure 1.4.

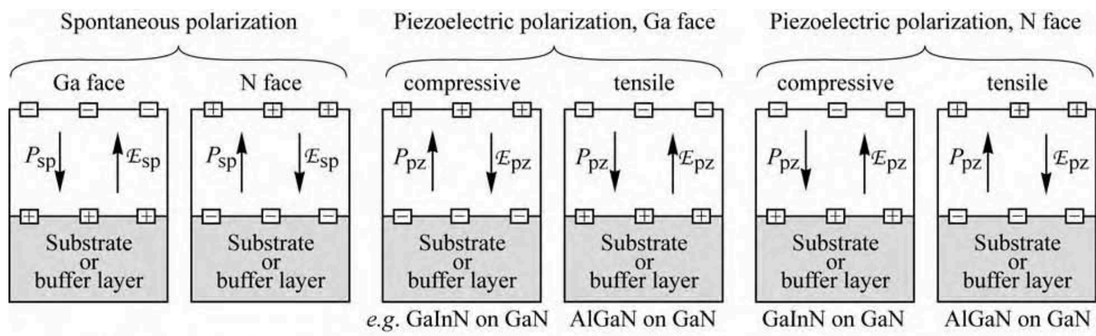

Figure 1.4 Surface charges, direction of electric field and polarization field for spontaneous and piezoelectric polarizations in III-nitrides with both Ga and N faces. [29]

For InGaN/GaN-based multiple quantum wells (MQWs) in our case, thin InGaN is inserted between GaN layers and the compressive strain is formed, which results in upward polarization. The polarized electric field tilts the energy band, through which the spatial overlap of electrons and holes can be decreased, as shown in Figure 1.5 (a), thus the recombination rate [30]. If the electric field inside the quantum wells can be decreased, even totally eliminated as shown in Figure 1.5 (b), the carrier wave-function overlap can be increased and thus the efficiency.

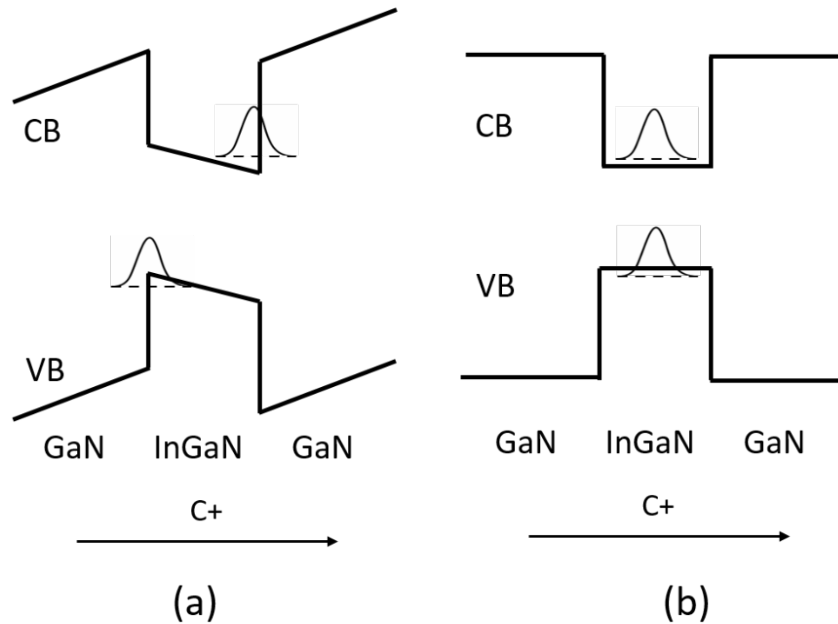

Figure 1.5 Schematic band diagrams for (a) polarized and (b) non-polarized InGaN/GaN-based quantum well along C+ direction.

Besides the polar InGaN/GaN-based LEDs grown on c-plane substrates, there still exist semi-polar and non-polar LEDs, which are grown on semi-polar and non-polar substrates. For InGaN/GaN-based quantum wells, since the spontaneous polarization effect is almost the same between GaN and InN [31], piezoelectric polarization is the main reason causing the electric field inside the quantum wells. The polarization intensity strongly depends on the growth orientations, which

has been reported by Takeuchi et al [28], with the relation as shown in Figure 1.6. When the polar angle is 90º, there is no piezoelectric field, which corresponds to non-polar plane. When the polar angle is between 0 and 90º, it corresponds to one semi-polar orientation and the polarization field can be minimized by adjusting the polar angle.

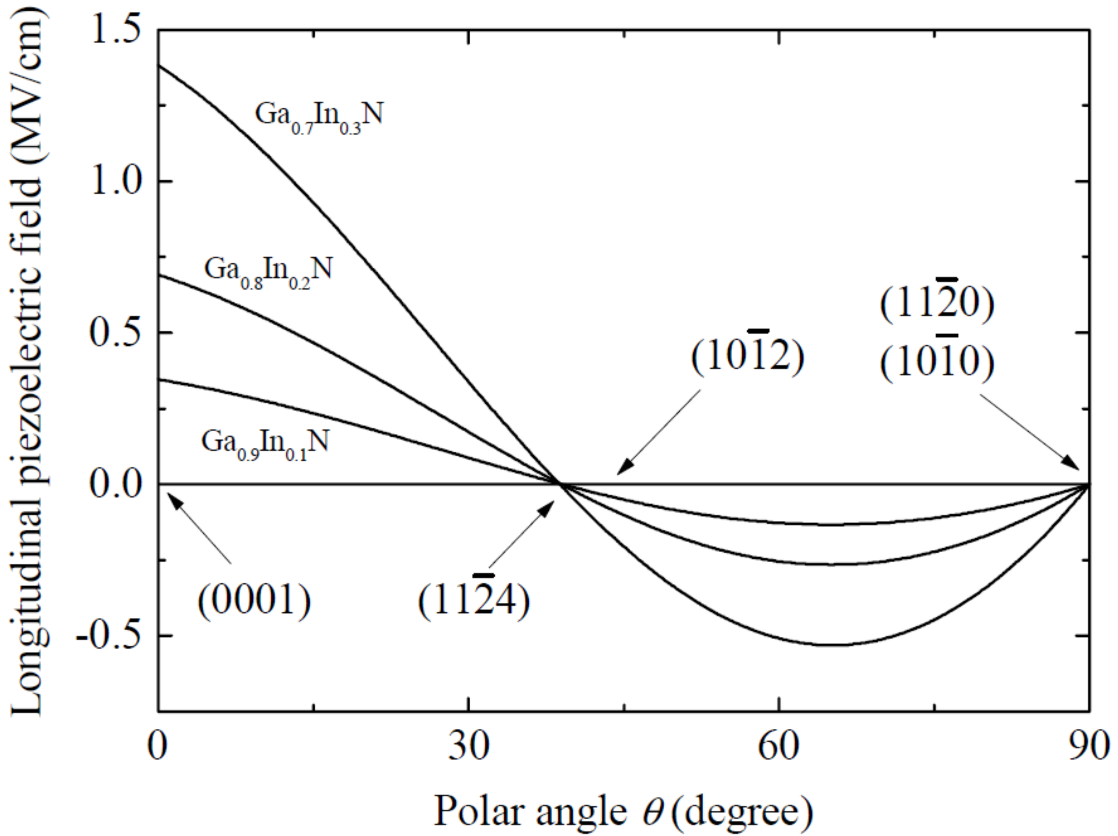

Figure 1.6 Longitudinal piezoelectric field in strained InGaN on GaN with different indium components under different polar angles from (0001).

1.2.1.4 Doping property

N-type GaN is realized through Si doping, while p-type GaN is realized by Mg doping. However, p-doping is a major obstacle due to the formation of Mg:H complexes and the passivation of the Mg dopant [32]. Even though the problem has been solved as mentioned previously, the deep acceptor level of Mg (0.125 – 0.215 eV) [33] still results in

a low percentage of dopant activation and pronounced temperature dependence of conductivity.

1.2.2 Advantages for III-nitride LEDs

When compared with the traditional incandescent and fluorescent lighting techniques, III-nitride LEDs possess many advantages as discussed below.

1.2.2.1 High efficiency

The energy conversion efficiency from electrical to optical is very high for LEDs since a photon would emit for each electron injected into the quantum wells in a direct band gap semiconductor. Under the condition of perfect crystal quality of semiconductors, no phonons would emit, which means no extra energy is wasted on heat generation when compared with the traditional incandescent lighting. Figure 1.7 shows the efficiency development of the commonly used lighting sources, and the efficiency of white LEDs increases rapidly, which has surpassed many of other lighting sources in recent years.

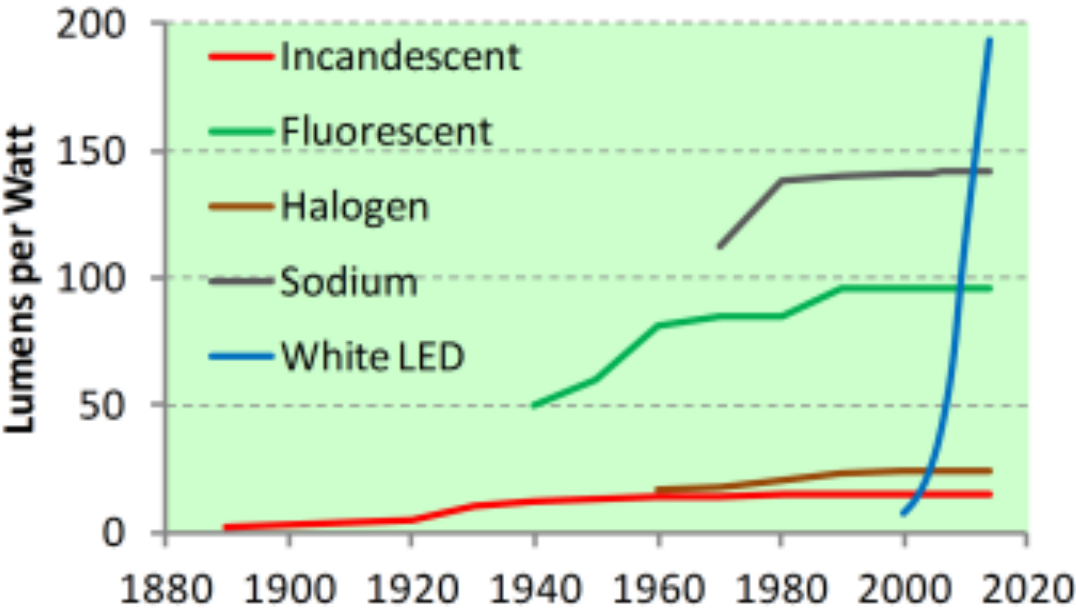

Figure 1.7 Luminous efficiency of different lighting sources. [34]

According to the report from department of energy (DOE) [35], lighting technologies are responsible for 18% of electricity use in USA, which is approximate 694 terawatt-hours in 2010. By applying LED lighting, it indicates that about 20% of electricity consumption in 2020 and nearly 50% in 2030 can be reduced, as shown in Figure 1.8.

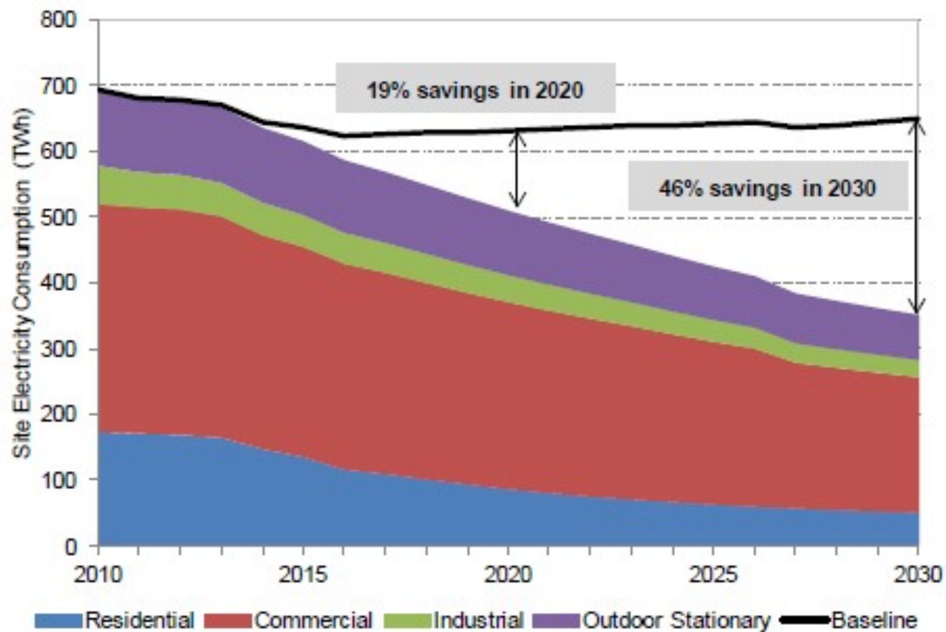

Figure 1.8 Total U.S. Lighting Energy Consumption Forecast, 2010 to 2030. [35]

1.2.2.2 Long lifespan

The lifetime of an LED is expected to be around 25000 to 100000 working hours [36], much longer than that of both incandescent and fluorescent lightings. Longer lifespan can reduce the maintenance and replacement frequency of LED bulbs, and thus the cost for lamp fixtures.

1.2.2.3 Color diversity

By selecting the proper material, LED can emit light of various wavelengths, from infrared, visible to ultraviolet with very high brightness, as mentioned previously. For the most commonly used white light LED, it can be realized in the following three methods,

phosphor-converted LED, color-mixed LED, and hybrid of previous two methods. A schematic generation principle is as shown in Figure 1.9 [37].

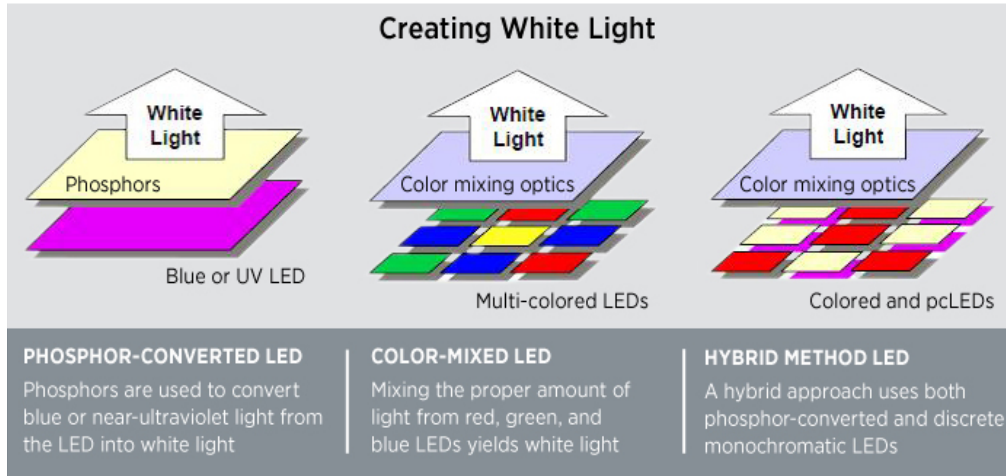

Figure 1.9 Creating white light by three different techniques for LED. [37]

1.2.2.4 Compact

The size of LED chips is at millimeter level, which increases the flexibility of its usage, and can be made possible for fitting into hard to reach and compact areas.

1.2.2.5 High-reliability

The physical properties of III-nitride materials are very robust and they are expected to be used in many harsh environments such as a wider temperature range from -40 to 85 ^{O}C, with humidity below 65%.

1.2.3 Applications for III-nitride LEDs

Owing to advantages as stated above, the III-nitride LEDs have been widely used in our daily life for lighting and display purpose, including indoor lighting, building lighting, traffic signals, automobile lights and displays, as shown in Figure 1.10 [38-42].

Besides the lighting property, LEDs also have many functional properties. As emerging applications, they can be used in the field of horticulture [43, 44], which can replace

the sunlight through mimicking the color components to make the plants grow faster, as shown in Figure 1.11(a). They can also be used in the field of Li-Fi [44], which can complement the wireless communication technology, as shown in Figure 1.11(b).

Figure 1.10 Applications of LEDs in indoor lighting, building lighting, traffic signals, automobile lights, and displays. [38-42]

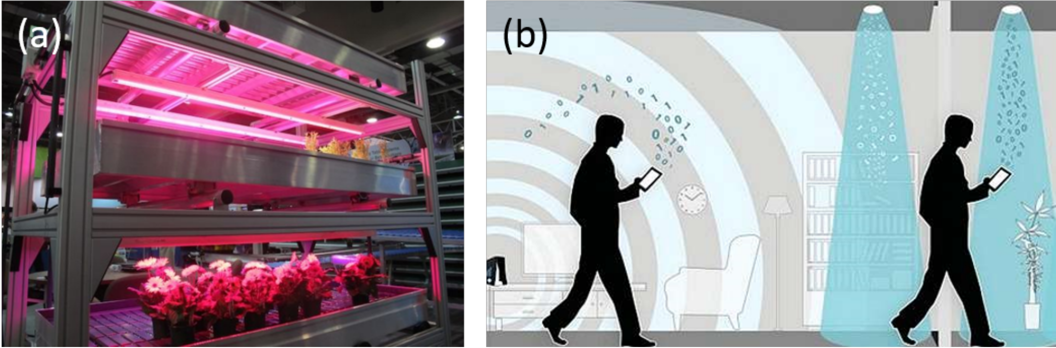

Figure 1.11 Emerging applications of LEDs used in the fields of (a) horticulture [36] and (b) Li-Fi [45].

1.2.4 Challenges for III-nitride LEDs

External quantum efficiency (EQE) is defined by the number of photons emitted for each pair of injected electron-hole carriers. In common sense, if we want to increase the output power and decrease the cost-per-watt, we would increase the injection current to generate more photons for each sample. However, this method is not applicable due to a phenomenon called efficiency droop, in which the EQE only peaks at low current and then drops substantially with increasing current, while high current is required in many high-power application fields [46]. Even this obstacle has frustrated this field for decades, the exact reasons causing the efficiency droop are still under debate. Many proposals have been put forward for discussions, including auger recombination [47], polarized electric field [48], electron overflow [49], and inefficient hole injection [50, 51].

In addition to the efficiency droop, which mainly originates from the internal device operation, factors in the fabrication process also affect the performance of LEDs, such as the current spreading layer and the reflective ohmic contact.

Besides the parameters that can be optimized to improve the performance of the planar structure LEDs in both growth and fabrication aspects, there are still some intact problems that can't be avoided, such as the polarization charges and limited quantum well thickness in the polar InGaN/GaN-based LEDs grown on sapphire substrates.

1.3 Research motivation and objectives

In order to maximize the efficiency of the state-of-the-art InGaN/GaN-based LEDs, several technological difficulties have to be overcome when designing structures of the InGaN/GaN-based LEDs, including the Auger recombination, polarized electric field, electron overflow, and low hole injection.

In addition to the growth process optimization, the efficiency can also be increased

through modifying the fabrication parameters during standard fabrication process, such as decreasing the contact resistance, increasing the transparency of transparent conductive layer (TCL) and the reflectivity of the mirror layer.

Besides the conventional growth and fabrication techniques, novel structures of InGaN/GaN-based LEDs, such as microwall structure, can also be designed, grown and fabricated, in which the polarization effect can be alleviated and the thickness of quantum wells can be increased due to the strain relaxing in the semi-polar/non-polar facets.

1.4 Thesis organization

We have arranged the thesis into seven chapters as follows.

Chapter 1: This chapter briefs a historical background and general introduction about III-nitride LEDs. Properties, advantages and applications for III-nitride LEDs have also been briefed to provide a general idea about why we choose this topic. Countering the obstacles met in the application process, we proposed corresponding motivations and objectives for the thesis considering InGaN/GaN-based LEDs.

Chapter 2: This chapter describes different physical concepts used in the thesis. Firstly, three different recombination mechanisms are described and this concept is most essential to LEDs. Then the underlying mechanisms about efficiency droop are elaborated after the introduction of the recombination mechanism. The tunnel junction, which is applied in the tandem LEDs, is then introduced, which lets us understand the following work better. At last, the situation of reflective ohmic contact to p-GaN is discussed.

Chapter 3: In this chapter, firstly we describe the growth process for planar InGaN/GaN-based LEDs through MOCVD system, accompanied by some conventional problems met by this method. Then, two ideas are proposed to improve the performance of InGaN/GaN-based LEDs during my research work. In the first work, the concept of tandem

LEDs is introduced, in which more than one active region is connected by tunnel junctions and proves to be effective to improve LED performance. In the second work, the quantum barriers of InGaN/GaN-based LEDs are doped with Mg, which results in reduced forward voltage and increased electrical thermal stability.

Chapter 4: In this chapter, we firstly introduce the fabrication process for the three typical device structures. Based on the fabricated devices, reflective ohmic contact is required for both flip-chip and vertical structure LEDs, and two methods are proposed to improve their performance. In the first work, a decoupled mirror deposition method is discussed which can realize the ohmic contact by thin Ni/Ag annealing and maintain the high reflectivity of intact silver. In the second work, the surface of p-GaN is modified by combining with ITO elements through high-temperature annealing, and best wall-plug efficiency is achieved at operation current through optimizing the $InGa_xN_yO_z$ interfacial layer.

Chapter 5: Before studying how the microwall structure can improve the efficiency droop of InGaN/GaN-based LEDs, this chapter introduces some preliminary work about GaN micromicrowall growth, in which different morphologies of GaN structures are achieved by modulating the growth parameters, accompanied by some related characterization results. Then, some basic results are achieved for the as-grown micromicrowall LEDs, which is a good start for the future work in this field.

Chapter 6: This chapter gives the conclusions for all the work included in this thesis and presents prospective for the future work.

Appendix A: The first part of this chapter introduces the general information about MOCVD growth, including the precursors, system design and growth mechanism. The second part of this chapter describes some characterization techniques, including scanning electron microscopy (SEM), atomic force microscopy (AFM), high-resolution x-ray

diffraction (HRXRD), photoluminescence (PL), Raman spectroscopy, x-ray photoelectron spectroscopy (XPS) and secondary ion mass spectroscopy (SIMS), etc. The last part of this chapter gives us a simple introduction about APSYS simulation methodology.

Chapter 2

Physical Phenomena and Concepts for LEDs

In this chapter, some physical concepts, which are used in the thesis, will be described. When it comes to the efficiency droop, the recombination mechanism is required to be understood firstly. The tunnel junction is also necessary to improve the performance of LEDs and the underlying physical properties of the tunnel junction will be introduced here. As stated in the first chapter, as the thesis is focused on the final performance of LEDs, reflective ohmic contact to p-GaN is critically important during the fabrication process, which will also be explained.

2.1 Recombination mechanism in LEDs

There are mainly three kinds of recombination mechanism in the LEDs, which are radiative recombination, Shockley-Read-Hall (SRH) recombination and Auger recombination. The processes for each of them will be described in the following part.

2.1.1 Radiative recombination

Radiative recombination means that light will be emitted after the recombination of electrons and holes in the LEDs. The recombination process is illustrated in Figure 2.1(a). The energy of the emitted photons equals to the energy band gap of the semiconductors. Since one pair of electron and hole is involved in the recombination process, the radiative recombination rate is expressed as equation 2.1 [29]:

$$R_{Radiative} = Bn^2 \quad (2.1)$$

where B is the radiative recombination coefficient and n is the carrier concentration,

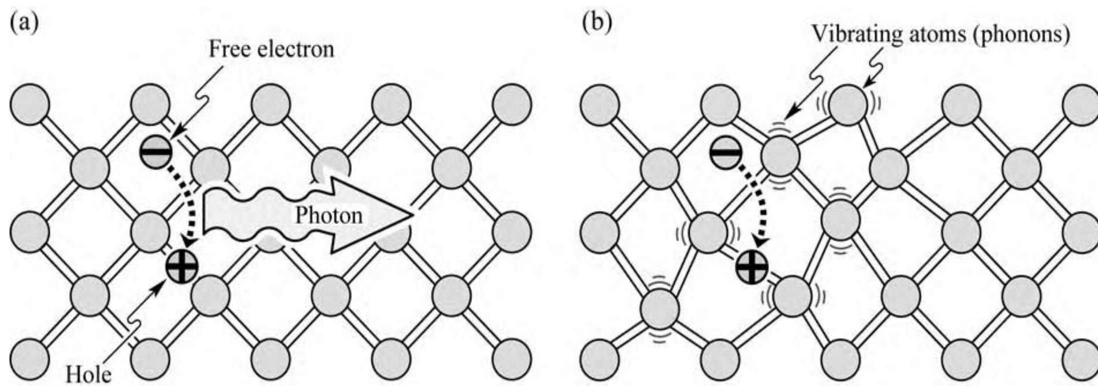

Figure 2.1 Lattice models for (a) radiative recombination and (b) non-radiative recombination. [29]

2.1.2 Shockley-Read-Hall (SRH) recombination

Competing with radiative recombination, InGaN/GaN-based LEDs suffer from SRH recombination [29]. This kind of recombination mainly originates from defects. During the SRH nonradiative recombination process, the recombination energy is converted to vibration of lattice atoms instead of photons, as shown in Figure 2.1(b). The SRH recombination rate is given in equation 2.2:

$$R_{SRH} = An \quad (2.2)$$

where A is the SRH recombination coefficient and n is the carrier concentration,

2.1.3 Auger recombination

Auger recombination is another important nonradiative recombination mechanism. In the Auger recombination process, the recombination of carriers will generate energy instead of photons and the energy will be used to excite a free electron into the conduction band or a hole into the valence band [29]. Since there are three carriers involved in this recombination process, the recombination rate is expressed as equation 2.3 [52]:

$$R_{Auger} = Cn^3 \quad (2.3)$$

where C is the Auger coefficient and n is the carrier concentration.

2.2 Efficiency droop in LEDs

As discussed previously, efficiency droop means that the EQE peaks only at low current density and then starts to decline when the current increases [52]. In this part, the mechanism of efficiency droop will be described.

The EQE is defined by the product of the light extraction efficiency (LEE) and the internal quantum efficiency (IQE), where the LEE is constant for a definite structure. When we talk about the total recombination rate [52, 53], we have:

$$R_{total} = An + Bn^2 + Cn^3 + k(n - n_0)^m + f(n) \quad (m>2) \quad (2.4)$$

where A is the SRH non-radiative recombination coefficient, B is the radiative recombination coefficient, C is the Auger recombination rate, k is the non-radiative loss mechanism accounting for the carrier delocalization and f (n) is the carrier leakage.

From the recombination mechanism, the IQE can be calculated through equation 2.5,

$$\text{IQE} = \frac{R_{radiative}}{R_{total}} = \frac{Bn^2}{An + Bn^2 + k(n - n_0)^m + f(n)} = \frac{B}{\frac{A}{n} + B + k(n - n_0)^{m-2} + f(n)/n^2} \quad (m>2) \quad (2.5)$$

As indicated from equation 2.5, the IQE is influenced by SRH recombination, the Auger recombination and the other recombination. Since the coefficient A is much larger than C and k, the effect of the Auger recombination and the other recombination become negligible at low current, and the value of IQE increase with the increasing carrier density. However, when the carrier concentration increases much, the Auger recombination and the

other recombination start to dominate and the SRH recombination can be neglected when compared with them. Under this condition, the IQE will decrease with further increasing the current density and so will the EQE.

2.3 Tunnel junction in LEDs

Tunnel junction, which is also called tunnel diode here, is composed of heavily doped p- and n- semiconductors [54]. In this thesis, it is composed of heavily doped p-GaN and n-GaN. When the tunnel junction is reversely biased, carriers will tunnel through the junction.

In LEDs, it can be used to replace p-GaN, since it is much easier to realize ohmic contact for heavily doped n-GaN [55]. When it is used to connect different active regions, the function of the tunnel junction is to draw electrons from the valence band of the p-type material into the n-type material through the inter-band tunneling, and holes in the valence band on the p-side into the active region [56]. Thus, the carriers can be repeatedly used and eventually increase the efficiency of LEDs.

2.4 Reflective ohmic contact in LEDs

In order to achieve high performance InGaN/GaN-based LEDs, it is critically important to form low-resistance ohmic contact for them because larger voltage drop across GaN/contact interface will greatly decrease their stability [37]. To achieve ohmic contact, the barrier height between GaN and contact should be small, or the GaN should be heavily doped, by the means of which, the carriers can pass through the barriers more easily.

The barrier height is determined by the workfunction between GaN and contacts. For n-GaN, the ohmic contact can be formed when the workfunction of metals is smaller than that of the n-GaN, so there are a lot of choices. For p-GaN, the ohmic contact can be formed only when the workfunction of metals is larger than that of p-GaN. However, this is very difficult to realize since the workfunction of p-GaN is much larger than those of the most

metals. Furthermore, due to the large activation energy of Mg dopant in p-GaN, the doping concentration is always limited and the tunneling of holes become difficult.

In order to realize the ohmic contact with p-GaN, a lot of techniques have been applied, including surface treatment and annealing. In addition to ohmic p-contact, reflective contact is required for flip-chip and vertical LEDs, and it is difficult to maintain the high reflectivity and realize ohmic contact at the same time. In this thesis, new methods are proposed to maintain high reflectivity and low-resistance ohmic contact simultaneously to realize high performance InGaN/GaN-based LEDs.

Chapter 3

Epitaxial Growth and Designs of InGaN/GaN LEDs

In this chapter, we will study the design and growth of InGaN/GaN-based LEDs, which are realized through MOCVD technique. Firstly, the epitaxial growth procedure for InGaN/GaN-based LEDs through MOCVD system is briefed. Then, LEDs with different designs will be studied both experimentally and theoretically. For the tandem LEDs, theoretical study is conducted and improved performance is demonstrated, which is attributed to increased carrier concentration and relatively reduced forward voltage. Besides the theoretical study of tandem LEDs, the LEDs with Mg doping in the quantum barriers are studied in both experimental and theoretical aspects. Reduced forward voltage and increased electrical thermal stability are observed, which are caused by decreased depletion length at equilibrium and relatively improved acceptor concentration.

3.1 Epitaxial growth techniques using MOCVD

3.1.1 Epitaxy with MOCVD

During the growth process, the sapphire was chosen as the substrate for III-nitride materials growth. Before the substrates were loaded, the chamber was cleaned by H_2 at high temperature. Then, nitridation was initiated on top of sapphire substrates by the flowing NH_3, and the resulted AlN or AlO_xN_{1-x} was formed as strain relaxation layer [57], hence facilitating the formation of the following low temperature nucleation layer. Later, a high temperature unintentionally doped GaN buffer layer was grown, which was followed by Si-doped n-type GaN. During the process stated above, TMGa was the precursor for Ga, NH_3 was the precursor for N, SiH_4 was used for Si dopant and H_2 was the carrier gas. Then the InGaN/GaN multiple quantum wells (MQWs) were grown, during which process the carrier gas was switched to N_2, the Ga precursor was switched to TEGa and the temperature was decreased to enhance the indium incorporation. After the growth of MQWs, the carrier gas was switched back to H_2 and the Ga precursor was changed back to TMGa. For the growth of p-

type AlGaN electron-blocking layer (EBL), TMAl provided Al source and Cp_2Mg provided Mg dopant. P-type GaN was grown after EBL, followed by a thin layer of highly p-doped GaN, which was the capping layer to make the ohmic contact easier. After all the growth process, the samples were annealed in N_2 atmosphere at 700 ℃ to activate the Mg dopant since its activation energy was very high. The detailed growth parameters are as listed in Table 3.1, in which T is the thermocouple reading in the susceptor. The as-grown epi-wafer consists of un-doped GaN buffer layer, 2 μm thick n-GaN with doping concentration of $5\times10^{24}\ m^{-3}$, eight pairs of $In_{0.15}GaN_{0.85}$/GaN quantum wells, with the thicknesses of the barrier and the well being 12 nm and 3 nm, 15 nm thick $Al_{0.2}Ga_{0.8}N$ electron blocking layer, with p-doping concentration of $3\times10^{23}\ m^{-3}$ and 200 nm thick p-GaN layer with doping concentration of $3\times10^{23}\ m^{-3}$.

Table 3.1 Growth parameters during the whole process for all the layers

Parameter	Carrier	T (℃)	Pressure (mbar)	Ga	N	In	Al	Si	Mg
Bake	H_2	1270	150						
Nitridation	H_2	693	600		NH_3				
Nucleation	H_2	693	600	TMGa	NH_3				
Un-doped	H_2	1281	675	TMGa	NH_3				
N-GaN	H_2	1281	250	TMGa	NH_3		SiH_4		
QB	N_2	999	340	TEGa	NH_3				
QW	N_2	939	340	TEGa	NH_3	TMIn			
EBL	H_2	1220	100	TMGa	NH_3	TMAl			Cp_2Mg

P-GaN	H_2	1180	160	TMGa	NH_3				Cp_2Mg

3.1.2 Wafer-scale epitaxial material characterization

Figure 3.1 (a) shows the as-grown epi-wafer for InGaN/GaN-based LEDs and the appearance after it is lighted up. From this figure, we can see the surface is quite smooth and it can be lighted up at any point. Besides the appearance, Figure 3.1 (b) presents the electroluminescence spectrum for the as-grown sample. The wavelength peaks at 449 nm and the FWHM is 18.4 nm which indicates good quality of the epi-wafer [58]. The optical output power and EQE are as shown in Figure 3.1 (c), while the efficiency peaks at 15%

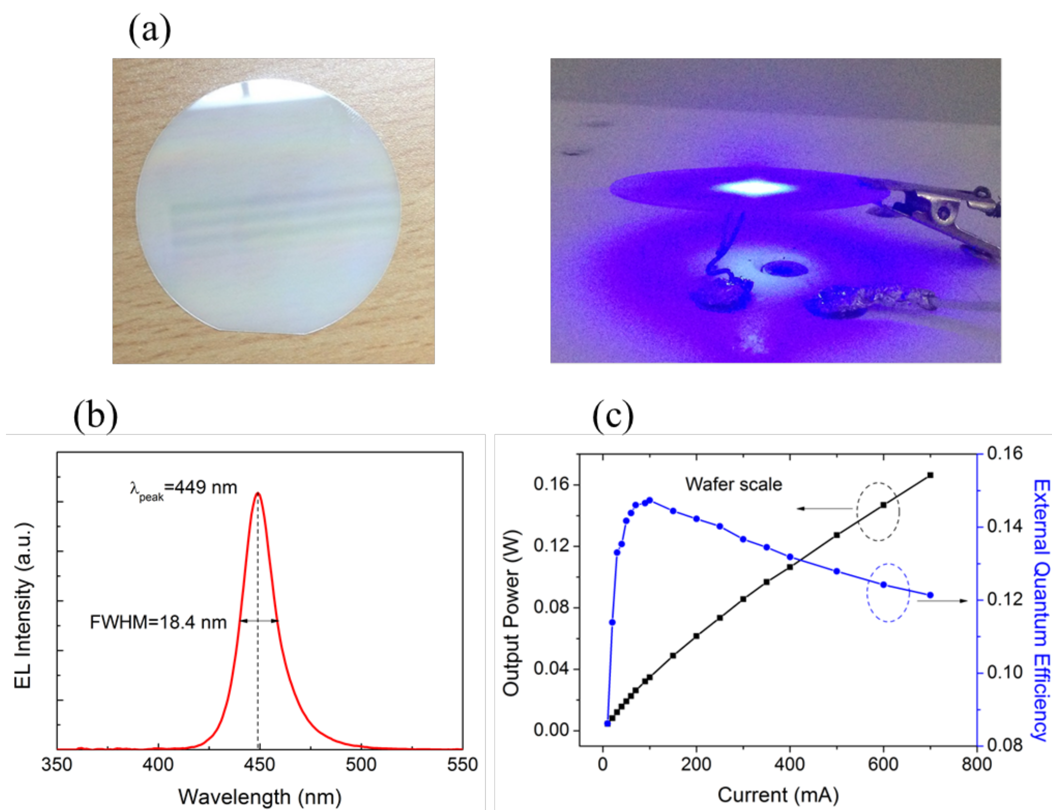

Figure 3.1 (a) Typical as-grown InGaN/GaN-based LED epi-wafer achieved in my work, and the appearance after it is lighted up, (b) electroluminescence spectrum for the grown sample and (c) the wafer-scale output power and EQE versus current.

Figure 3.2 (a) shows the thickness mapping, which measured the thickness of the epi-wafer using optical interference. Figure 3.2 (b) shows the peak wavelength mapping, which gives us an idea about the distribution of peak wavelength over the entire wafer. The uniformities of both the thickness and the peak wavelength are acceptable.

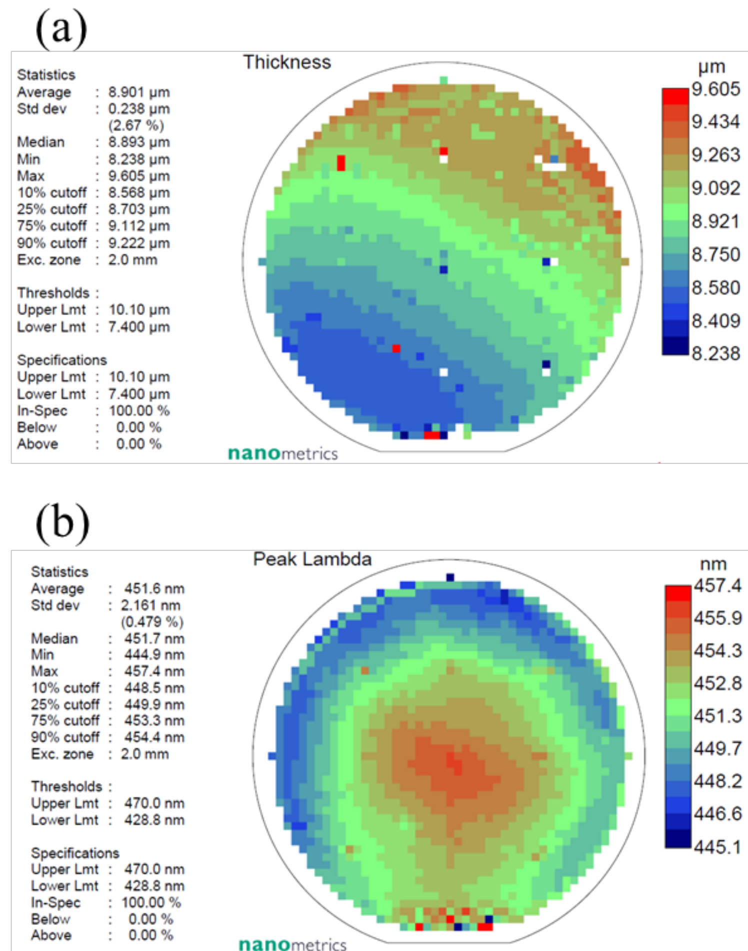

Figure 3.2 (a) wafer thickness and (b) PL peak wavelength mapping.

Figure 3.3 shows the HRXRD rocking curve (RC) for both the symmetric (002) and asymmetric (102) reflecting planes. The FWHM of the RC for the symmetric (002) reflecting plane only reflects the screw and mixed-type dislocations with the value of 0.08 degree, while

the FWHM for the asymmetric (102) reflecting plane corresponds to all threading dislocations with the value of 0.09 degree [59, 60]. The small values indicate their superior quality when compared with InGaN/GaN-based LEDs grown by other groups [61, 62].

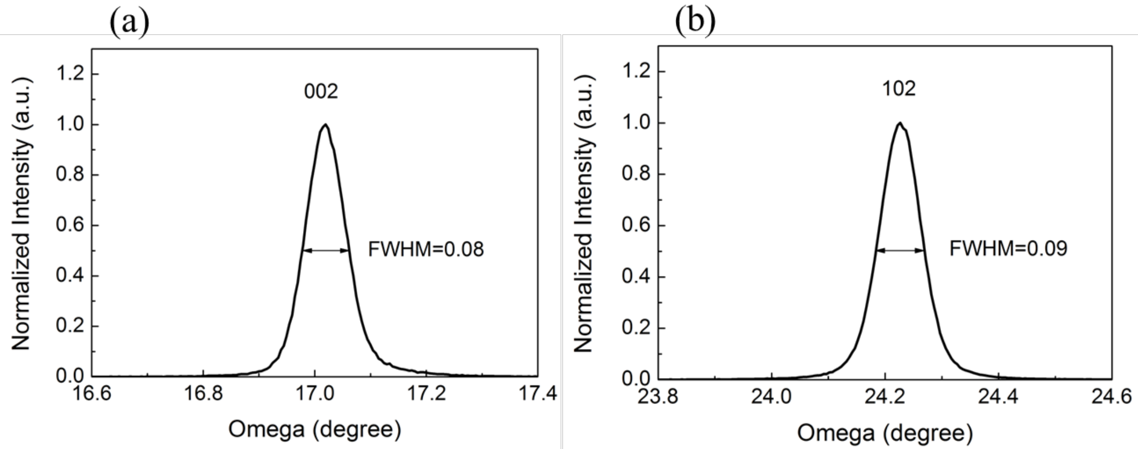

Figure 3.3 HRXRD rocking curves for LEDs along (a) the symmetrical (002) and asymmetrical (102) reflection planes.

Even though the material quality of the as-grown samples is well above the acceptance level of common device requirements, there are still large room to further improve the performance of the InGaN/GaN-based LEDs. Optical property, which is affected by the efficiency droop, is one of the biggest obstacles for the development of high-brightness and high-efficiency LEDs [63-67]. Besides the efficiency droop, the electrical property is also one of the key parameters that affect the performance of InGaN/GaN-based LEDs.

In the following part, we will introduce two designs of structures, which will improve both of the optical and electrical properties of InGaN/GaN-based LEDs.

3.2 Epitaxial design using tandem LEDs with tunnel junction

3.2.1 Introduction

LEDs have achieved widespread applications in recent years, but their efficiency decreases significantly at high power operation, which hinders the penetration of high power LEDs into the general lighting markets. Tandem LEDs have more than one active regions which are connected by tunnel junctions in series [68]. They have the potential to achieve high output power through high voltage instead of high current, which can help alleviate the efficiency droop [68]. In this work, the performance of the tandem LEDs is studied by APSYS simulation and compared with the traditional LEDs. An extraordinary efficiency improvement is observed and the mechanisms for the improvement are analyzed.

3.2.2 Modeling

APSYS software is based on the drift-diffusion model, which solves Poisson equation, continuity equation and Schrödinger equation self-consistently.

The Auger recombination coefficient was set as 1×10^{-30} cm^6s^{-1} and the band offset between the conduction and valence band was set as 0.7:0.3. Considering the crystal relaxation, 40% of the theoretical polarization charge was assumed. All the parameters were set according to the experimental conditions [69]. For the tandem LEDs, two active regions were connected by the tunnel junction. For each active region, it was composed of three quantum wells, with the thicknesses of the barrier and the well being 12nm and 3nm respectively. For the tunnel junction, doping concentrations of both n-GaN and p-GaN in the normal tunnel junction were 1×10^{27} m^{-3}, and the thickness of both n-GaN and p-GaN was 20 nm. For the InGaN tunnel junction, a 3 nm thick $In_{0.15}Ga_{0.85}N$ layer was inserted between the n-GaN and the p-GaN. The details of the simulated structures can be seen in Figure 3.4(a). The other parameters can be found in the related reference [70].

3.2.3 Results and discussions

Figures 3.4 (b) and (c) show the calculated results of the output power and the forward

voltage for all the simulated devices. In the figures, reference, TJ and TJ with InGaN stand for the traditional LED, the tandem LED with the normal tunnel junction, and the tandem LED with the InGaN tunnel junction, respectively. As shown in Figure 3.4 (b), the output power densities at 100 A/cm^2 for the three devices are 74.5 W/cm^2, 220 W/cm^2 and 236 W/cm^2, respectively. The values for the tandem LEDs are more than three times of the traditional LED, though the active regions are just double in volume. The tandem LED with the InGaN tunnel junction has even better performance. From Figure 3.4 (c), the forward voltage at 100 A/cm^2 for the traditional LED is 5.76 V, while the value is 9.98 V for the tandem LED with TJ and 9.94 V for the tandem LED with InGaN TJ, respectively. According to Figure 3.4 (b) and Figure 3.4 (c), the efficiencies for the three devices are 12.93%, 22.04% and 23.74%, respectively. The possible reasons for the efficiency improvement include reduced forward voltage per active region and improved carrier distribution uniformity. As can be seen, the forward voltage per active region for the tandem LEDs is 4.99 V and 4.97 V, respectively, which is lower than the 5.76 V of the traditional LED. This is due to the nature of the tunnel junctions, which can reduce the voltage drop when two active regions are connected in series. The improved carrier distribution uniformity in the tandem LEDs is analyzed in the following.

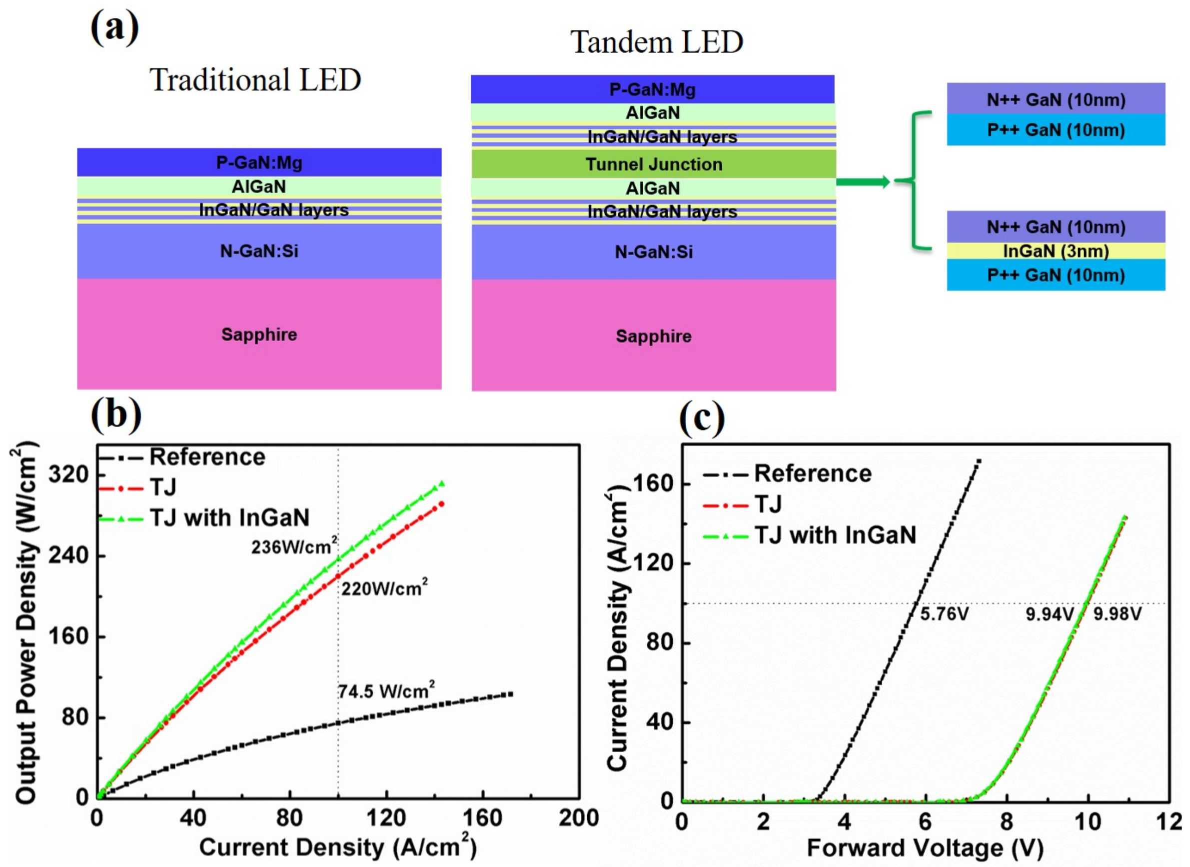

Figure 3.4 (a) Schematic device structures for simulation, (b) output power density and (c) forward voltage vs. current density for all the simulated devices.

The distributions of carrier concentration are illustrated in Figure 3.5. Electron concentration of the reference in Figure 3.5 (a) is not uniform, much higher in the last well and lower in the first well. However, the distribution of electron concentration is more uniform for the tandem LEDs as shown in Figure 3.5 (b) and 3.5 (c). The distribution characteristics for the hole concentration are quite similar. Higher internal quantum efficiency can be promoted by the more uniform carrier distribution which helps alleviate Auger recombination rate and electron leakage, and generate light from a larger effective recombination volume. The difference between the tandem LEDs with different tunnel junctions appears mainly in the last quantum well in the second active region. For the tandem

LED with InGaN-based tunnel junction, both the electron concentration and the hole concentration are higher in the last well which is caused by the higher transmission probability of the tunnel junction which will be explained in the following.

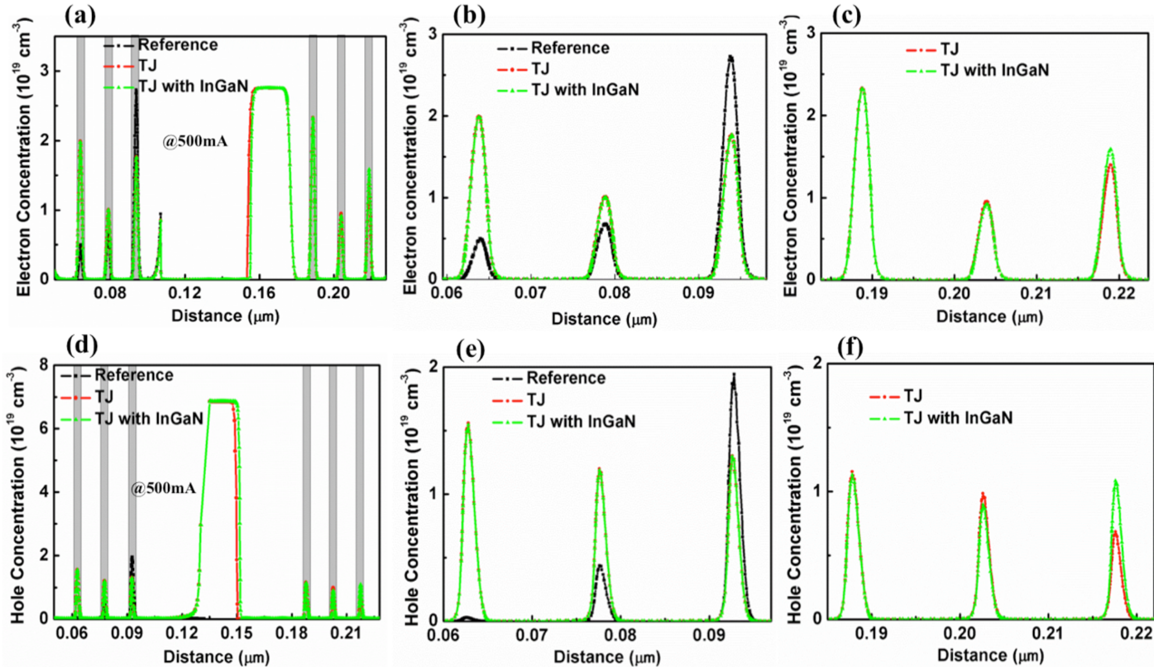

Figure 3.5 Distribution of carrier concentration at current density of 100 A/cm^2: electron concentration for the whole structure (a), first active region (b), and second active region(c), hole concentration for the whole structure (d), first active region (e), and second active region (f).

Since the insertion of InGaN between heavily doped tunnel junctions can generate polarization charges due to piezoelectric polarization, the electric field in the tunnel junction is greatly enhanced when compared with the GaN tunnel junction, as shown in Figure 3.6. Tunneling probability is therefore significantly increased by the enhanced electric field in the tunnel junction [71].

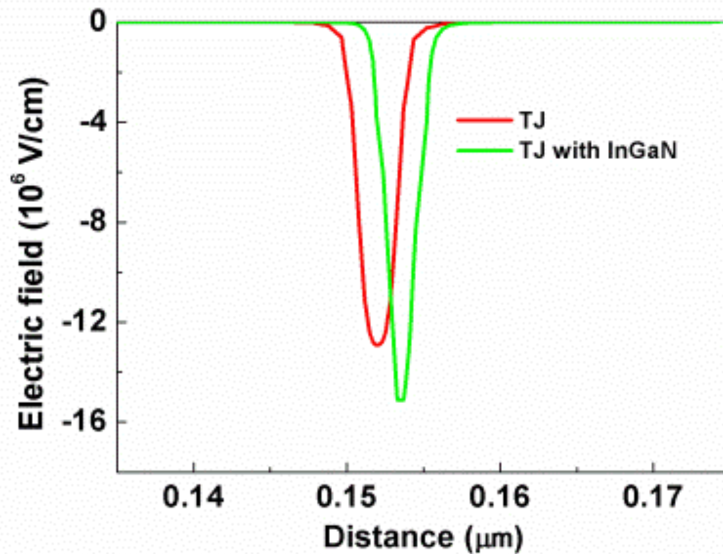

Figure 3.6 Electric field profile calculated across the tunnel junction from p+-GaN.

Even through the tandem LEDs show superior performance in the theoretical studies, it is difficult to present such better performance in experimental results since heavily p-doping is not easy to realize due high activation energy of Mg dopant. If p-doping concentration can be enhanced further, the tandem LEDs will become very promising in the application of high efficiency LEDs.

3.2.4 Conclusions

In conclusion, we have proposed the tandem LEDs, which consist of more active regions and investigated their property numerically. Substantial improvement of the efficiency has been achieved when compared with the traditional LED. The reduced forward voltage per active region and the more uniform carrier distribution are the reasons behind the improvement. We also compared tandem LEDs with different junctions, and it shows that TJ with InGaN has larger tunneling possibility and enhances the performance further.

3.3 Epitaxial design using doped barriers

3.3.1 Introduction

During the last few decades, due to many advantages such as long lifetime, durable quality and high efficiency, InGaN/GaN-based LEDs have achieved widespread applications in many aspects, such as general lighting, LCD backlights and automobile lighting [72]. However, plenty of research in this field was focused on their optical properties in the last few years, and the investigation on electrical properties is not conducted carefully [73, 74]. As one of the most important parameters, worse electrical property can directly lead to more heat generation, which will cause the degradation of LED performance and the decrease of the wall-plug efficiency simultaneously [75]. Besides, studies on the electrical properties can help to uncover the inherent physics of LED devices [73, 76]. For example, the capacitance-voltage (C-V) characteristics can be used to reveal the depletion region widths at various biases [77]. Besides, it has been reported that Mg doping in the quantum barriers is promising to improve the LED external quantum efficiency effectively [78]. However, the impact about how the Mg doping in the quantum barriers affects the electrical property is not fully studied yet.

In this work, we compare the electrical characteristics of InGaN/GaN-based LEDs for the sample with Mg doping in the barriers and the reference without Mg doping in barriers. The mechanism for the reduced turn-on voltage and improved thermal stability is studied and analyzed through capacitance-voltage characteristics and self-consistent simulation.

3.3.2 Experiments

The LED epi-layers were grown on c-plane sapphire substrates by metal-organic chemical vapor deposition (MOCVD) system, with schematic diagrams as illustrated in Figure 3.7. For LED A, the growth was initiated on a 30 nm-thick GaN nucleation layer [71]. Then, a 2-μm-thick undoped GaN was grown as the buffer layer, which was then followed

by a 4-μm-thick n-doped GaN layer with an electron concentration of 5×10^{18} cm^{-3}. Then, four pairs of $In_{0.15}Ga_{0.85}N$/GaN quantum wells were grown and the thicknesses of quantum barriers and quantum wells were 12 nm and 3nm, respectively. Finally, a p-type electron blocking layer (EBL) of 20-nm-thick $Al_{0.15}Ga_{0.85}N$ was grown and it was then capped by a 200-nm-thick p-type GaN with a hole concentration of 3×10^{17} cm^{-3}. After the growth, LED A was annealed at the temperature of 700 ℃ in N_2 ambient to activate p-type dopants. LED B is the proposed sample with Mg doping in the quantum barriers, the growth of which was the same as LED A except that the middle 6 nm region in each quantum barriers was doped by Mg dopants with a doping concentration of 3×10^{17} cm^{-3}. The structure for selectively Mg doping in each quantum barrier was to suppress the Mg diffusion into quantum wells. After epitaxial growth, both LED A and LED B were fabricated into standard LED chips. Ni (5 nm)/Au (5 nm) layer was deposited and annealed firstly which acted as the current spreading layer. Then, the mesa area with the size of 1 mm×1 mm was obtained by inductively coupled plasma (ICP) etching, and Ti/Ag/Ti/Au was deposited as electrodes for both n and p contacts. Then, the current-voltage characteristic was measured by the SC-200-mm prober station, and the temperature was controlled by the hot plate in the range from 25 ℃ to 150 ℃. The capacitance-voltage characteristic was also measured by the SC-200-mm prober station, with the AC signal voltage of 20 mV and frequency of 1 MHz.

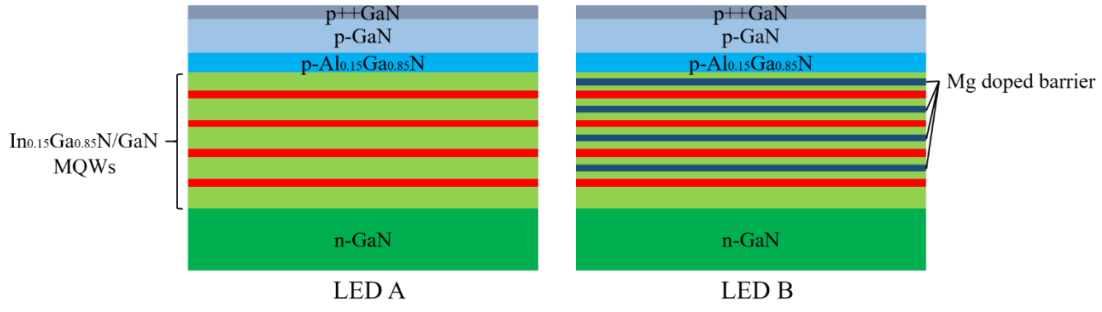

Figure 3.7 Schematic diagrams for studied LED structures, in which LED A is the reference and LED B is the sample with Mg doping in the quantum barriers.

Furthermore, in order to reveal the physical insights, we also performed numerical simulations by APSYS software, which self-consistently solves the Poisson equation, continuity equation and Schrödinger's equation with proper boundary conditions. In our simulation, the Auger recombination coefficient is taken to be 1×10^{-30} cm^6s^{-1} [79] and the SRH lifetimes for both electron and hole are 43 ns [79, 80]. The polarization charge is set as 40% of theoretical value due to crystal relaxation [11]. The other parameters can be found in the reference [70].

3.3.3 Results and discussions

Figure 3.8 (a) shows the experimental *I-V* characteristics for both devices measured under different temperatures. Here, we choose the current of 20 mA as the reference for electrical analysis. The forward voltage at room temperature for LED A is 3.37 V and for LED B is 2.95V, which means the voltage is decreased by 0.42 V for LED B. For the temperature dependent *I-V* curve, temperatures are chosen as 25°C, 50 °C, 75 °C, 100 °C, and 150 °C. The forward voltages for LED A at different temperatures are 3.37, 3.26, 3.15, 3.04 and 2.86 V respectively, while the values for LED B are 2.95, 2.88, 2.82, 2.76 and 2.63 V respectively. The decreasing values of the forward voltages are 0.11, 0.11, 0.11 and 0.18

V with increasing temperature for LED A, while those of LED B are 0.07, 0.06, 0.06 and 0.13 V respectively. Thus, we can conclude the thermal stability of electrical property is better for LED B than that for LED A. The reduced forward-voltage and improved thermal stability for LED B will be explained as follows.

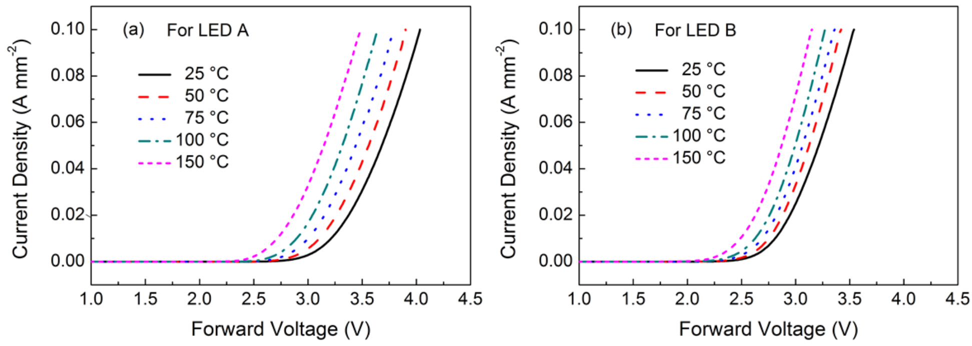

Figure 3.8 *I-V* characteristics under temperatures from 25 °C to 150 °C for (a) LED A and (b) LED B.

Figure 3.9 (a) shows the capacitance-voltage characteristics for both samples at room temperature. At zero bias voltage, the capacitance of the LEDs is mainly composed of the junction capacitance, which can be expressed as

$$C = \varepsilon A / L \quad , \qquad (3.1)$$

in which ε represents the permittivity with the value of 8.5 ε_0, A is the area of the junction with the value of 1×1 mm^2, and L is the length of the depletion region [77]. From the experimental data based on Figure 3.9 (a), the junction capacitance is 0.94 nF for LED A, and 2.98 nF for LED B. Then we can calculate the depletion length based on equation 3.1, which is 76.5 nm for LED A and 23.7 nm for LED B. In the simulation, the voltage was set at 0.1 V, which could be compared with zero bias. The depletion length was extracted from the calculated capacitance at 1 MHz which is 76 nm for LED A and 33 nm for LED B. The trend for the change of the depletion length is consistent with the experimental results. From

Figure 3.9 (a), we can also see that the capacitance starts to decrease when the voltage increases to a certain value and even becomes negative when the forward voltage is large enough. The decrease of capacitance is caused by the carriers' recombination in the quantum wells [81], and the voltages at peak capacitances for both samples are 2.65 V and 2.26 V, respectively. The difference between the carriers' recombination onset voltages for the two samples is similar with the difference between the forward voltages at 20 mA, which is a direct evidence for the reduced forward voltage. Since the doping concentration in n-GaN is much higher than that in p-GaN, the LED can be treated as a model of donor and acceptor doping with concentration N_D on the n$^+$-side and N_A on the p-side, respectively. The acceptor concentration, N_A, can be calculated by the following equation [82],

$$N_A = -\frac{2}{\varepsilon e A^2}\left[d\left(\frac{1}{C^2}\right)/dV\right]^{-1}, \text{ if } N_D \gg N_A, \qquad (3.2)$$

in which C is the measured capacitance, V is the forward voltage and the meaning of other parameters can be found above. The acceptor doping concentration is 1.75×10^{22} m^{-3} for LED A, and 1.22×10^{23} m^{-3} for LED B, which are resulted from the calculation. When $N_D \gg N_A$, the equation for the diffusion voltage can be expressed as equation 3.3 [29],

$$V_D = \frac{W_D^2}{2\varepsilon} N_A, \qquad (3.3)$$

in which V_D is the diffusion voltage, W_D is the depletion length and N_A is the acceptor concentration. After we substitute both values into equation 3.3, the following relation can be achieved, while the subscript 1 and 2 denote LED A and LED B.

$$V_{D1} > V_{D2}, \qquad (3.4)$$

Figure 3.9 (b) shows the simulated *I-V* characteristics for both samples at room temperature, from which we can see that the forward voltage is also smaller for the proposed

Mg doped sample, and this is consistent with the shown experimental results.

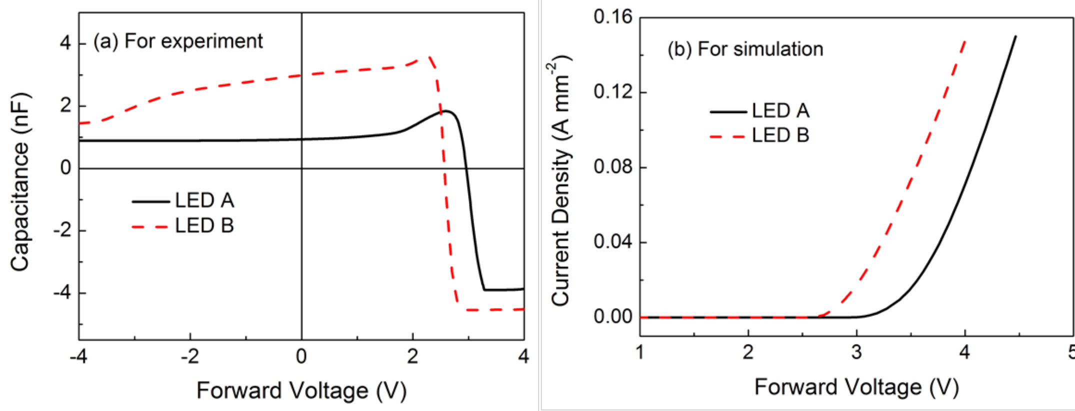

Figure 3.9 (a) Capacitance-Voltage characteristics, and (b) simulated *I-V* characteristics for both samples at room temperature.

Figure 3.10 depicts the forward voltage vs temperature under different injection currents. The dashed lines are linear fit for all the experimental results. According to the reference [83], a linear relationship between the junction temperature and forward voltage is found, while

$$\frac{dV_f}{dT} \approx \frac{k}{T}\ln(\frac{N_D N_A}{N_C N_V}) - \frac{\alpha T(T+2\beta)}{e(T+\beta)^2} - \frac{3k}{e}, \qquad (3.5)$$

in which k is the Boltzmann constant, T is the temperature, α, β are constants, N_C, N_v are effective density of states, and N_D, N_A are donor and acceptor concentrations. N_C, N_v are determined by the temperature [84]. Equation 3.5 is a lower limit for the magnitude of dV_f/dT, because the junction voltage is less than the built-in voltage in all practical cases [84]. According to the donor-acceptor model mentioned previously, they have the same donor concentration and the acceptor concentration is larger in the Mg doped sample. The value of dV_f/dT should be larger in LED B. From Figures 3.10 (a) and (b), the temperature

coefficients of the forward voltages at low current are -4.17 mV/K and -2.72 mV/K for LED A and LED B, repsectively, which is consistent with the analysis.

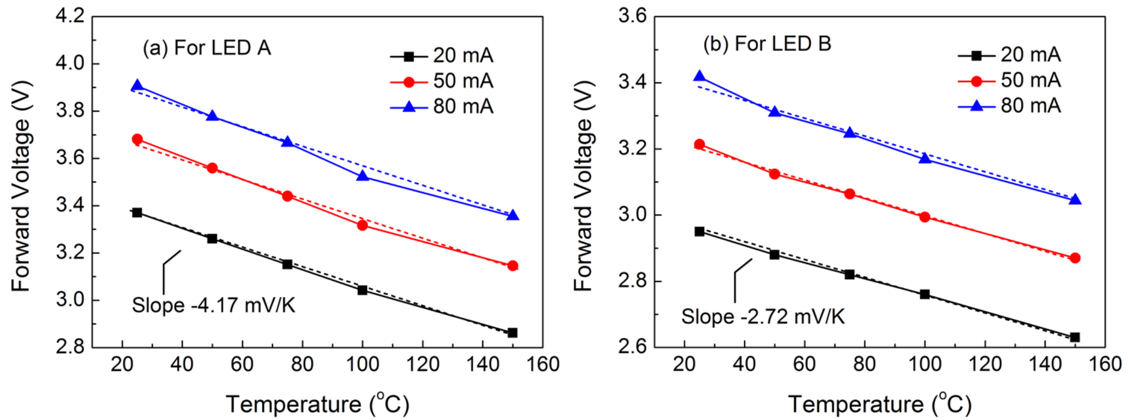

Figure 3.10 Measured forward voltage at different injection currents vs hot plate temperature, for (a) LED A and (b) LED B, with the dashed lines as linear fit for all the experimental data.

3.3.4 Conclusions

In conclusion, InGaN/GaN-based LEDs with Mg doped barriers have been prepared and the improved electrical performance was realized and investigated. Temperature dependent *I-V* characteristics and *C-V* characteristics were analyzed and decreased depletion length was observed in the proposed sample. A donor-acceptor model was proposed and increased acceptor concentration was achieved. Based on the above analysis, our results offer meaningful physical insights on the mechanism how the Mg doped barrier affects the electrical performance of InGaN/GaN-based LEDs.

3.4 Summary

In summary, this chapter has studied the growth and design of InGaN/GaN-based LEDs. The growth procedure and material quality for our epi-wafer were introduced and characterized. After the growth procedure, two kinds of structures were designed. The first

structure was tandem LEDs in which more than one active regions were connected by tunnel junctions. In this structure, substantial improvement of the efficiency was achieved when compared with the traditional LEDs. The reduced forward voltage per active region and more uniform carrier distribution were the reasons behind the improvement. We also compared tandem LEDs with different junctions, and it showed that TJ with InGaN had larger tunneling possibility and enhanced the performance further. In another structure, the quantum barriers were doped with Mg and electrical performance was improved. Both of the reduced turn-on voltage and improved electrical thermal stability were attributed to the reduced depletion length at equilibrium and relatively increased acceptor concentration.

Chapter 4

Fabrication and Device Designs of LEDs

In this chapter, LED chips with different configurations are fabricated, and their properties and applications are firstly described. Then, the focus is on the study of the reflective ohmic contact (mirror) to p-GaN, which can be applied in both flip-chip and vertical LED structures, and two different fabrication techniques are proposed and investigated to improve the LED performance. The first method to optimize the contact mirror is realized through a contact-mirror decoupled deposition, while the second method is achieved by engineering the $InGa_xN_yO_z$ interfacial layer between the contact mirror and the p-GaN, both of which are promising to realize the good ohmic contact and maintain high reflectivity of pristine silver mirror.

4.1 Device structure fabrication and characterization

4.1.1 Device fabrication

After InGaN/GaN-based LEDs are epitaxially grown on the sapphire substrates in MOCVD system, they will be fabricated into separate chips with various structures using standard processing techniques. The fabrication process defines the active light emission area and prepares metal electrodes in contact with the n-GaN and p-GaN. According to their light-emitting areas and contact geometries, there are mainly three kinds of structures existed in the market, which are top-up structure, flip-chip structure and vertical structure LEDs.

Figure 4.1 shows the fabricated top-up structure LEDs and Figure 4.2 presents us the fabrication process flow. During the fabrication process, firstly a transparent conductive layer (TCL) was deposited on top of p-GaN to spread the current uniformly, since the conductivity of p-GaN is poor caused by high acceptor activation energy of Mg [85]. Then the area of mesa was patterned by photolithography and etched by inductively coupled plasma (ICP) to expose the n-GaN for n-electrode deposition. After the etching process, electrodes for both of n-GaN and p-GaN were deposited. For this type of LED structure, the fabrication process

is simple and the cost is low. However, there are many disadvantages as stated below. First, since both n-electrode and p-electrode for GaN contact are on the same side and n-GaN is much more conductive than p-GaN [86], the current crowding effect is very easy to happen. More heat will be generated in a small region, which limits the device performance under high driving current. Besides, sapphire substrate has poor heat conductivity, thus resulting in heat accumulation, and degrading the device performance further [87]. The fabricated chips with top-up structure occupied most of shares in the market since the fabrication cost is cheap. This kind of LEDs is designed for medium power demand due to the limitation of current crowding effect and thermal effect [29].

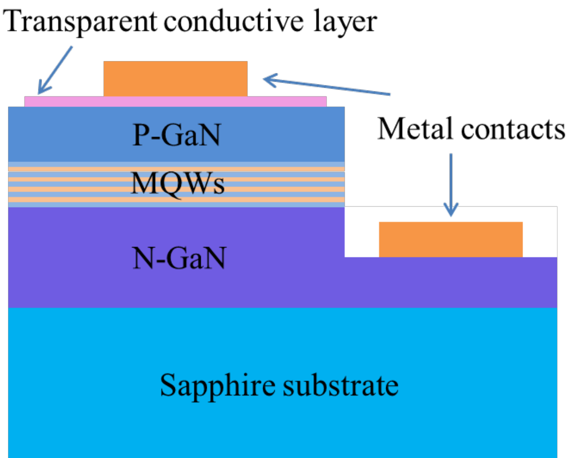

Figure 4.1 Schematic structure of top-up structure LED.

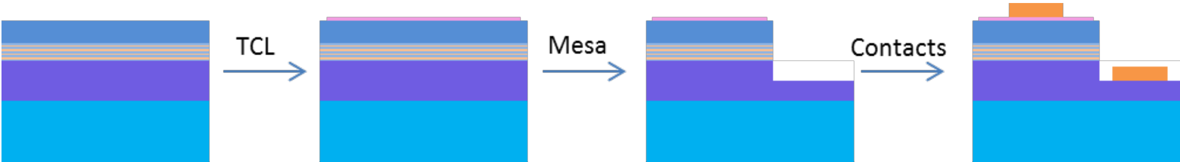

Figure 4.2 Process flow for top-up structure LED fabrication.

Figure 4.3 shows the fabricated flip-chip LED structure and Figure 4.4 shows the

correspondence fabrication process flow. Different from the top-up structure, the reflective mirror contact was deposited on top of p-GaN. In this case, the photons were reflected by the mirror and extracted out from the backside. The soldering process made contact for LEDs with flip-chip structure. When compared with the top-up structure, the lighting area was increased and the heat dissipation ability was enhanced due to the better thermal conductivity of the bonded substrate. The flip-chip structure LEDs tend to provide customs products with high power, medium cost and best reliability.

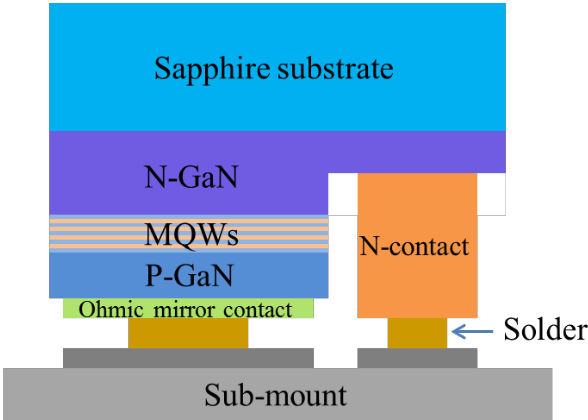

Figure 4.3 Schematic structure of flip-chip structure LED.

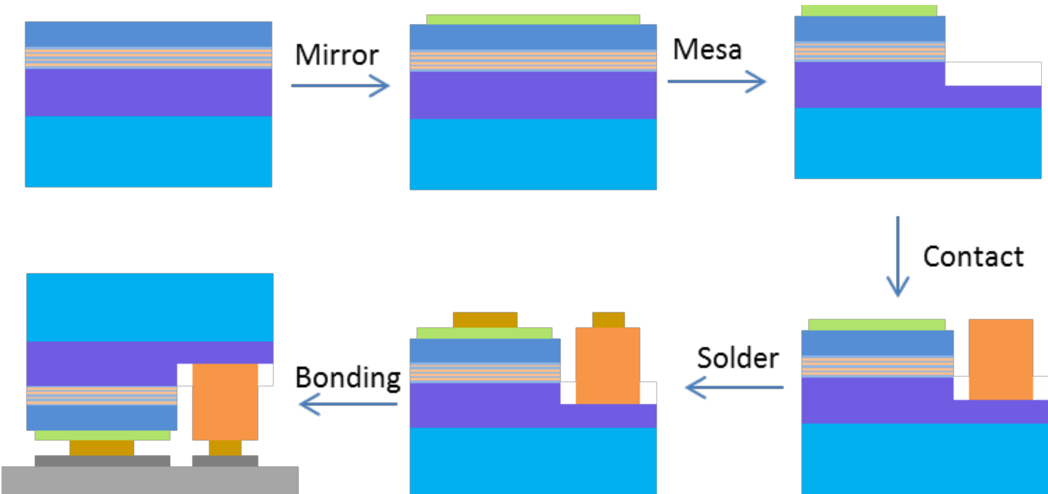

Figure 4.4 Process flow for flip-chip structure LED fabrication.

As shown in Figure 4.5 is the vertical structure LED. Similarly, Figure 4.6 presents the simplified fabrication process. From the process flow, we can see the mirror was deposited firstly on top of p-GaN, which served the same function as that in flip-chip LED structure. Then the bonding process was prepared and conducted to make the new substrates for LED devices, which were usually made of copper or silicon. After the new substrate was formed, the sapphire substrates were removed by the laser lift-off process, during which excimer laser would decompose the GaN at the interface between GaN and sapphire. After the sapphire removal, the buffer layer of un-doped GaN was etched out by ICP and the exposed n-GaN was textured by KOH to increase the light extraction efficiency (LEE). At last, the contact was deposited on top of n-GaN, while the new substrate, which was made of conductive material, acted as p-contact. When compared with top-up structure LED and flip-chip structure LED, the current crowding effect is avoided since the contacts are distributed vertically. Besides, the sapphire substrate, which processes low thermal conductivity property, is removed and the heat dissipation ability is greatly improved. Since the thickness of n-GaN is much larger than that of p-GaN, the texture process was more promising for the vertical LEDs and the LEE will be greatly improved. However, for the fabrication process, the vertical LED underwent more steps and the yield pass rate was low, which resulted in higher fabrication cost. In the market, only limited companies can produce vertical LEDs, which oriented to high-power applications.

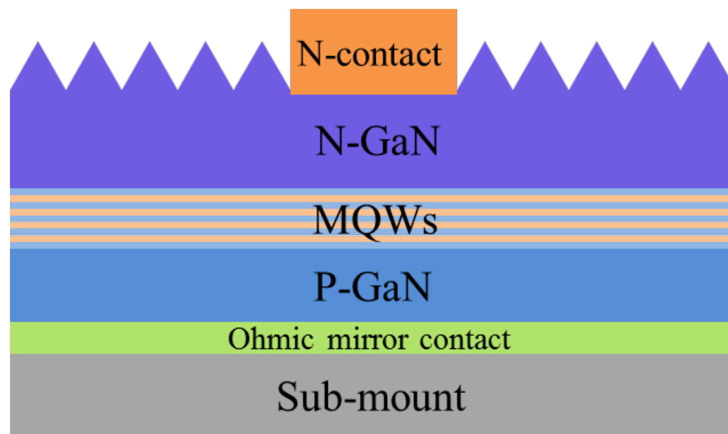

Figure 4.5 Schematic structure of vertical structure LED.

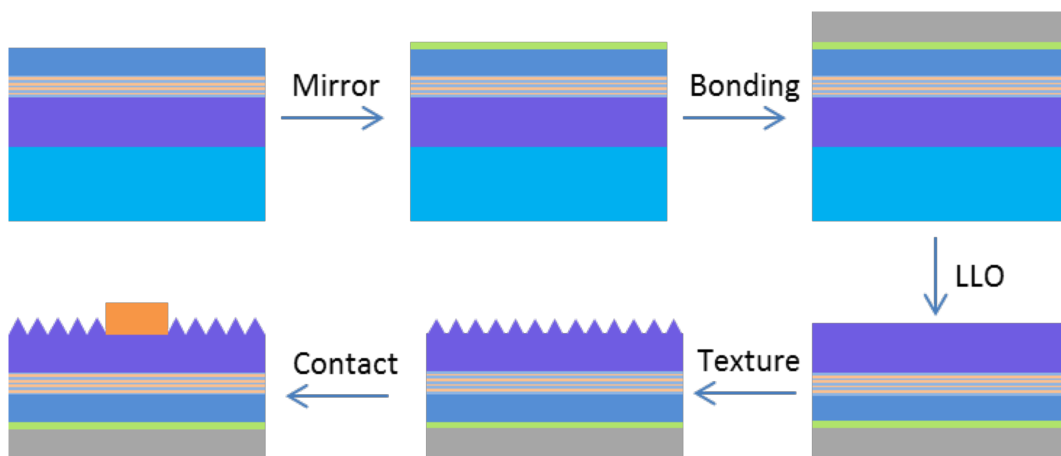

Figure 4.6 Process flow for vertical structure LED fabrication.

4.1.2 Device characterization

As shown in Figure 4.7 are the characterization results for top-up structure LEDs. Figure 4.7 (a) shows the appearance of the fabricated chips, while the left one is before and the right one is after being lighted up. Both of the beautiful appearance of the fabricated device and uniform light distribution over the entire die are observed, which demonstrated our superior fabrication capability. Figure 4.7 (b) shows the current-voltage characteristics and the forward voltage is 3.0 V at an injection current of 20 mA. Figure 4.7 (c) shows the

optical output power and EQE for top-up structure LEDs, from which we can see the EQE peaks at 13%, while the efficiency droop is quite severe, which is due to the intrinsic problems of epi-wafers and the thermal effect.

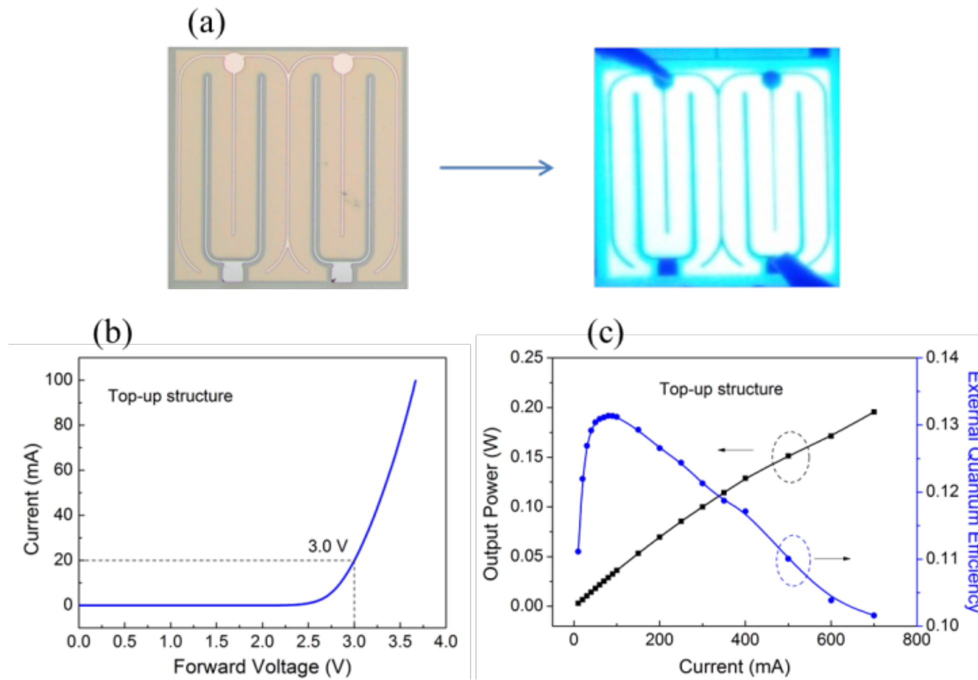

Figure 4.7 (a) the appearance of fabricated device with top-up structure, before and after being lighted up, (b) *I-V* characteristics, (c) output power and EQE for the fabricated device.

As shown in Figure 4.8 are the fabrication results for flip-chip structure LEDs. Figure 4.8 (a) shows the appearance of the fabricated chips, as left one is before and right one is after being lighting up. Since the contact for flip-chip structure LEDs is on the front and the light extraction is on the backside, the front image does not show patterns after the device is lighted up. Figure 4.8 (b) shows the current-voltage characteristics, while the forward voltage is 3.1 V at an injection current of 20 mA. Figure 4.8 (c) shows the optical output power and EQE for flip-chip structure LEDs, with the peak EQE at 36%, which is much larger than that in top-up structure LEDs.

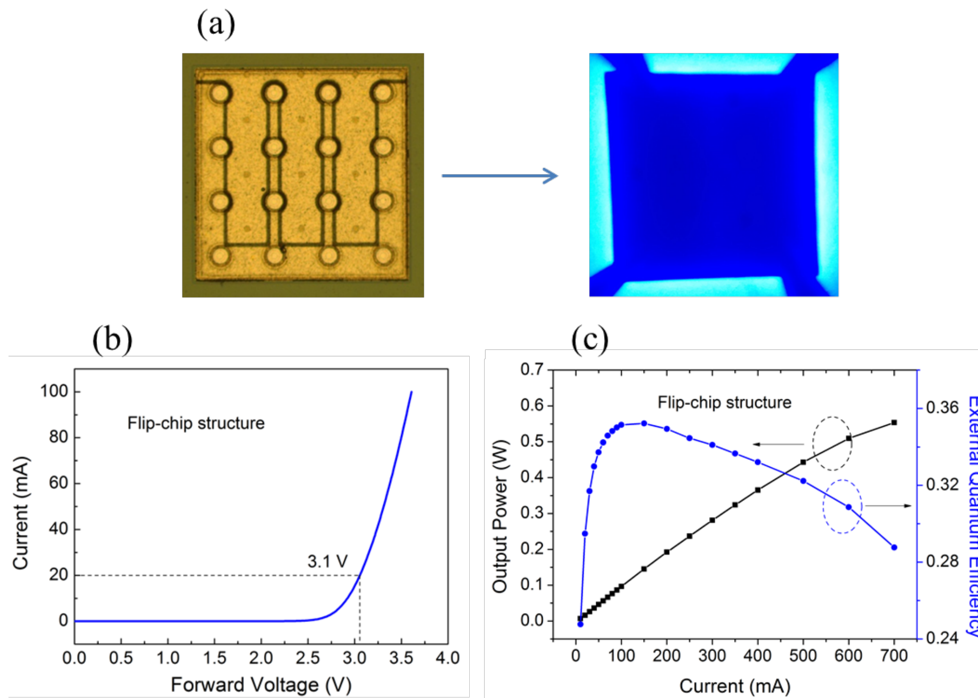

Figure 4.8 (a) the appearance of fabricated flip-chip structure, before and after being lighted up, (b) *I-V* characteristics, (c) output power and EQE for the fabricated devices.

As shown in Figure 4.9 are the characterization results for vertical structure LEDs. Figure 4.9 (a) shows the appearance of the fabricated chips, as left one is before and right one is after being lighting up. For the vertical LEDs, the n-contact is on the front and the p-contact is the copper substrate on the backside. Figure 4.9 (b) shows the current-voltage characteristics with the forward voltage at 2.9 V at injection current of 20 mA. Figure 4.9 (c) shows the optical output power and EQE for vertical structure LEDs. The largest current applied for vertical structure LED can be up to 2 A for one device with the mesa size of 1×1 mm^2.

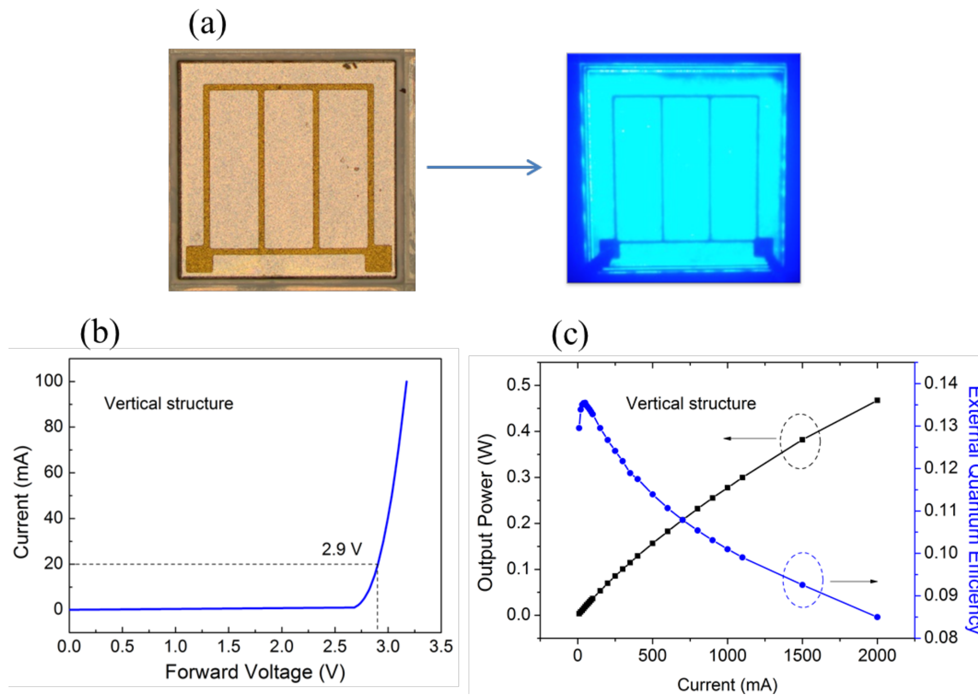

Figure 4.9 (a) the appearance of fabricated vertical structure LED, before and after being lighted up, (b) *I-V* characteristics, (c) output power and EQE for the fabricated devices.

From the device characterization results shown above, our capability to fabricate all different structure LEDs is demonstrated, which provides a sound platform for our following work. The performance of flip-chip and vertical LEDs is superior to top-up LEDs, in which structure light is reflected and extracted out from the backside. Thus, the mirror becomes the most critical part in the fabrication process and thus high quality p-type electrodes with good ohmic contact and high reflectivity need to be studied carefully. Generally, the ohmic contact between p-GaN and metals are difficult to form due to the following two reasons [88]. Firstly, the highly doped p-type GaN is very difficult to achieve due to the high activation energy of the Mg acceptors. Then, the work functions of metals are normally smaller than the value of p-GaN, which is 7.5 eV [89]. In order to improve the performance of these two structure LEDs, the reflective ohmic contact will be studied in the following part.

4.2 Device design using decoupled contact and mirror

4.2.1 Introduction

During the last decades, high-performance InGaN/GaN-based LEDs are gradually replacing incandescent and florescent light bulbs and applied in many fields, such as automobiles lighting, building lights and LCD backlighting [72]. However, the limited LEE still hinders further improvement of LED efficiency [90, 91]. For flip-chip structure LEDs, the photons are reflected by the reflective contact and emitted out from the sapphire side, in which the reflector on p-GaN is especially important [92, 93]. There are many options of metal stacks for the reflector of p-GaN, such as Ni/Ag/Pt [91], Ni/Ag/Ti/Au [93], Ni/Au/W/Ag [94] and Ni/Ag/Ru/Au [95]. For the used metal combinations, Ni is in direct contact with p-GaN, which is essentially significant to form ohmic contact [37, 41, 96]. The second layer deposited usually processes a high reflectivity in the visible spectral range, in which Ag is most usually used [97]. In the traditional fabrication process for flip-chip structure LEDs, the metal stack for the reflector is deposited on top of the p-GaN and the following rapid thermal annealing (RTA) process in oxygen atmosphere is conducted to realize ohmic contact. However, the reflectivity of mirror is severely reduced after undergoing high temperature annealing since Ag agglomerates and intermixes with other metals [93, 98], which will considerably deteriorate the performance of LED chips. A two-step deposition method has been proposed [93] to solve the intermixing issue of Ag with Au in the Ni/Ag/Au reflector where the Ni/Ag layer was deposited and annealed first, followed by intact Au layer deposition. Though the intermixing problem of Ag has been solved, the agglomeration problem continues due to the annealing process that the whole Ag has gone through. However, the reflectance of mirror reported was below 90% at 450 nm, which needs further optimization for high power LEDs.

In this part, we propose the idea of decoupling contact and mirror during the mirror fabrication process innovatively. An extremely thin Ni/Ag layer is deposited and annealed on top of p-GaN for ohmic contact formation. Then, thick Ag/Ti/Au layer is deposited without any annealing to act as reflection layer. The Ag layer in the contact is too thin to cause the agglomeration while it is enough to form the ohmic contact with Ni. The bulk Ag layer in the mirror remains intact with high reflectivity since it does not go through the high temperature annealing process. The reflectivity of the proposed mirror can reach 95% at 450 nm and the optical output power of the corresponding LED has been increased by more than 70% when compared with the LEDs fabricated through the conventional method at 350 mA. The underlying physics of decoupling contact and mirror are studied in detail through sheet resistance measurement and secondary ion mass spectrometry (SIMS) analysis.

4.2.2 Experiments

The LED chips are fabricated from the as-grown epi-wafers through a standard fabrication process. For the reference devices, traditional Ni/Ag/Ti/Au (1 nm/150 nm/100 nm/65 nm) mirror was deposited by e-beam evaporator and then annealed at 500 ℃ in N_2:O_2 (4:1) ambient for 5 mins. For the proposed devices, the contact layer consists of Ni (1 nm)/Ag (X nm) was initially deposited on top of p-GaN and annealed in the same condition as the reference, in which X equals to 0, 1, 3 and 5. Subsequently, the reflector layer consists of Ag/Ti/Au (150-X nm/100 nm/65 nm) was deposited without further annealing process. The surface morphologies were examined by the SEM (JEOL JSM-5600LV). The reflectivity was measured by UV/Vis/NIR Spectrophotometer System (PerkinElmer Lambda 950). The current-voltage (*I-V*) characteristics of the LED chips were measured using a LED quick tester (M2442S-9A Quatek Group) and the optical output power was measured by an Ocean Optics spectrometry (QE65000), which was attached with an integrating sphere. The sheet

resistance of the thin Ni/Ag contact layer was measured with a four-probe sheet resistance measurement system, and the element profile of the metal stacks were measured by the ToF-SIMS.

4.2.3 Results and discussions

The optimized thickness of Ag in the contact layer was analyzed through checking the surface morphologies of annealed surfaces by SEM, which is as shown in Figure 4.10. Low contact resistance and smooth surface morphology are required for an ideal contact. As shown in Figures 4.10 (a)-(d), the surface morphologies of the contact layers with Ag thickness of 0, 1, 3, and 5 nm after annealing are compared and the original smooth surface becomes roughened with the appearance of cluster structures and the density and size of the cluster structures increase with the increase thickness of Ag. The clusters are generated due to Ag agglomeration during the annealing process, which is determined by the thickness of Ag. As can be seen in Figure 4.10 (a), the surface is very flat and smooth for the sample without Ag in the contact layer. Even Ni can form clusters after annealing as reported in other reference[99], 1 nm Ni may be too thin to form clusters after annealing or the size of the clusters is too small to be noticed under SEM images. The optimized Ag thickness for the contact layer is 1 nm, which shows least Ag agglomeration centers as shown in Figure 4.10. The Ni contact layer only forms Schottky contact with p-GaN. The electrical properties of LEDs with various contact layers will be examined later.

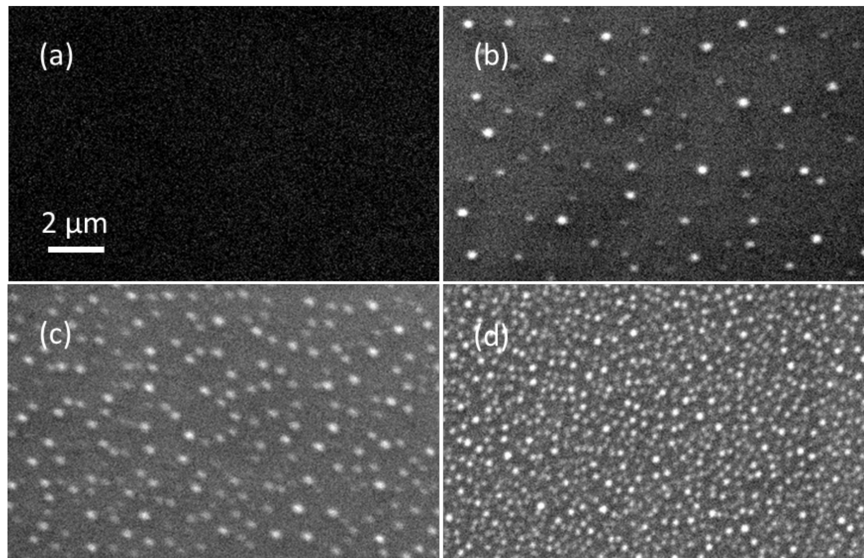

Figure 4.10 SEM images of the samples with a thin annealed (a) Ni (1 nm)/Ag (0 nm), (b) Ni (1 nm)/Ag (1 nm), (c) Ni (1 nm)/Ag (3 nm), and (d) Ni (1 nm)/Ag (5 nm) contact layer on top.

After the realization of ohmic contact layer, the reflector consists of thick Ag/Ti/Au is deposited on top. Figure 4.11 (b) shows the surface morphology of the proposed contact layer, along with the reflector constructed by the conventional method as shown in Figure 4.11 (a) for comparison. The conventional Ni/Ag/Ti/Au mirror undergoes a severe degradation, in which the large number of clusters features the surface morphology as shown in Figure 4.11 (a). In contrast, using the decoupling contact and mirror, the morphology is greatly improved, which exhibits much smoother surface and significantly reduced clusters both in density and size. SIMS depth analysis has also been conducted for the two reflectors to examine the element profiles as shown in Figure 4.11 (c) and (d). For the reference in Figure 4.11 (c), severe intermixing of different elements happens where Ni and Ag diffuse up to the surface and Ti and Au diffuse down to the interface between the contact layer and p-GaN. It is difficult to recognize the boundary of the mirror since it the mixed with the

contact layer. In contrast with the reference, the intermixing phenomenon is trivial in the reflector with the element profiles shown in Figure 4.11 (d), in which Ni is confined in the region where it is deposited and coincides with the Ag peak. The rest of the Ag layer is also pure without any observable out-diffusion phenomenon and the Ti and Au layers are also intact as deposited. The well-defined Ag layer makes positive impact on the performance of the mirror, which will be demonstrated by the reflectance measurement next. The schematic diagrams for the one-step mirror and the decoupled mirror are illustrated in Figure 4.12.

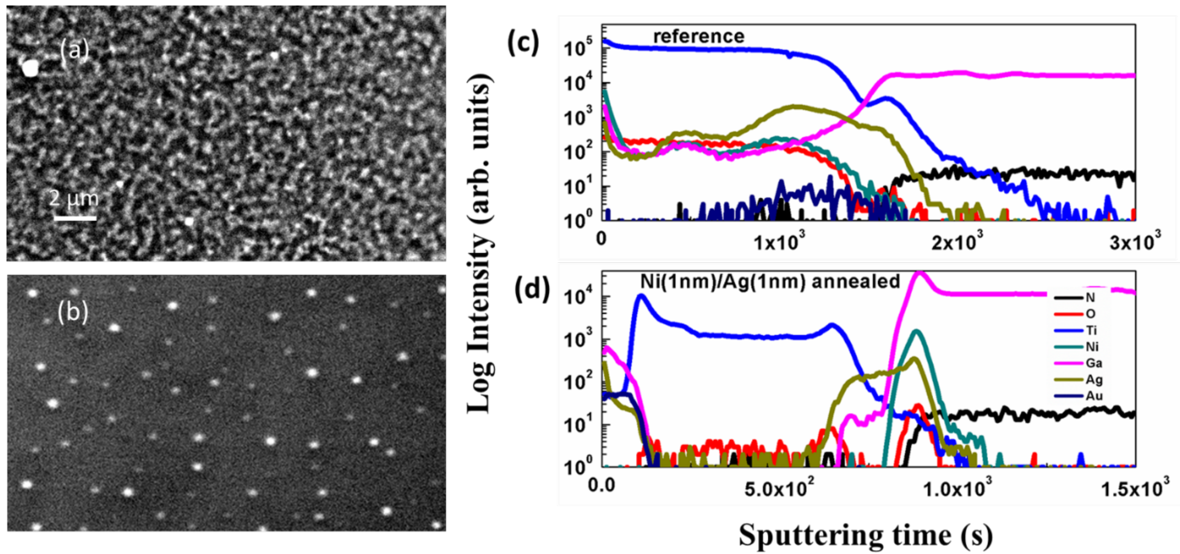

Figure 4.11 SEM images of the samples with (a) conventional mirror and (b) proposed mirror with annealed Ni (1 nm)/Ag (1 nm) as contact layer, and SIMS depth profiles of the samples with (c) conventional mirror and (d) proposed mirror with annealed Ni(1nm)/Ag(1nm) as contact layer.

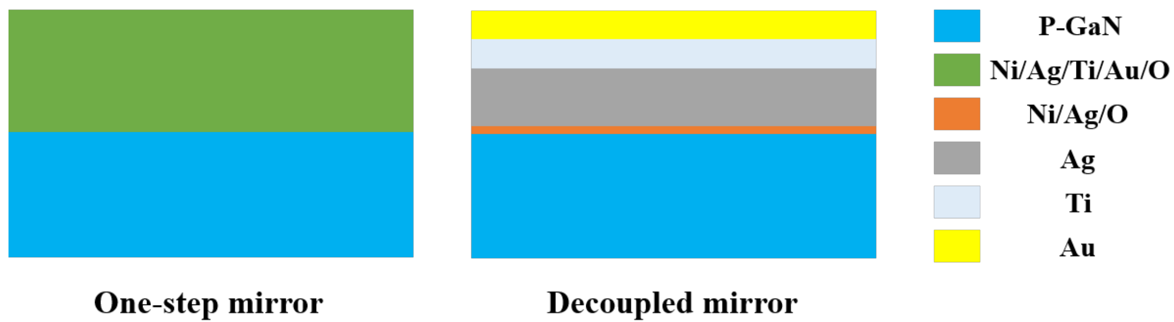

Figure 4.12 Illustration for one-step mirror and decoupled mirror.

Figure 4.13 reveals that the reflectivity of the decoupled contact mirror is much higher than that of the conventional Ni/Ag/Ti/Au mirror in the spectral range from 420 nm to 480 nm. For example, the reflectivity of the mirror with thin Ni (1 nm)/Ag (1 nm) contact layer is 95% at 450 nm, and the value is 62% in the conventional mirror for comparison. What's more, the thinner thickness of Ag in the contact layer, the higher the reflectivity. This result is in consistent with the SEM surface morphology and the SIMS depth analysis discussed above. The output powers of LEDs with the decoupled mirrors are shown in Figure 4.14, along with the performance of LED with the conventional contact mirror. The output power of the LEDs with the decoupled mirror is greatly increased when compared with that of the reference LED. For instance, at forward current of 350 mA, the optical power has been increased from 128 mW for the reference LED to 222 mW for the LED with the decoupled contact mirror of which the contact layer is Ni (1 nm)/Ag (1 nm), which is largely due to the improved reflectance of the decoupled contact mirror.

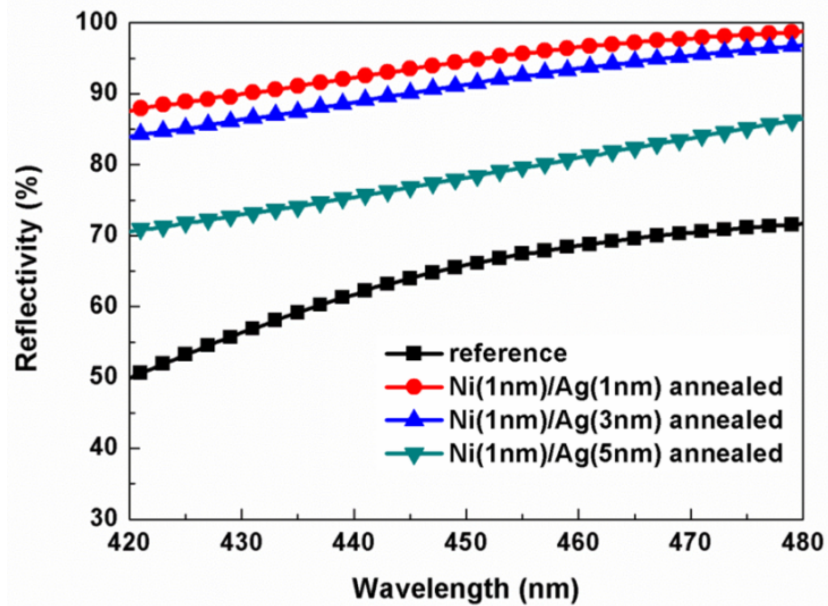

Figure 4.13 Reflectivity measured for the samples of the conventional contact mirror and the decoupled contact mirrors with thin annealed layer of Ni (1 nm)/Ag(1 nm), Ni (1 nm)/Ag (3 nm) and Ni (1 nm)/Ag (5 nm), respectively.

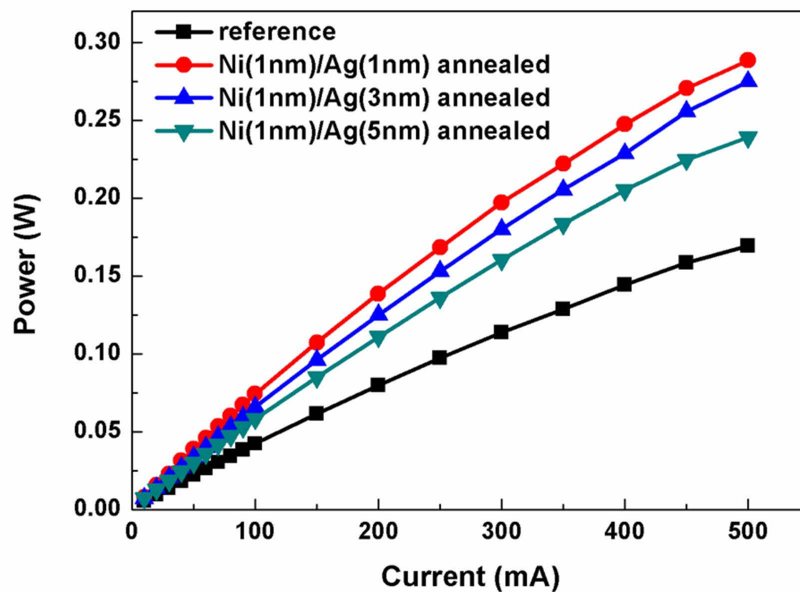

Figure 4. 14 Output power measured for LEDs with the conventional contact mirror and the decoupled contact mirrors with thin annealed layer of Ni (1 nm)/Ag (1 nm), Ni (1 nm)/Ag (3 nm) and Ni (1 nm)/Ag (5 nm), respectively.

In addition to the high reflectance, the electrical performance is also a very important factor for LEDs. As shown in Figure 4.15, the forward voltage of the LEDs with the optimized decoupled contact mirror is comparable to and even better than that of the reference LED at current beyond 350 mA. This indicates that the decoupled contact mirror also meets the requirement of good electrical performance besides high output power. It is implied that the electrical property starts to degrade as the Ag thickness increases in the thin Ni/Ag contact as shown in Figure 4.15. The forward voltage increases significantly, which is mainly due to the increase of the turn-on voltage. It is critical to uncover the mechanism behind the electrical degradation and understand the reason of the ohmic contact formation in the decoupling contact and mirror.

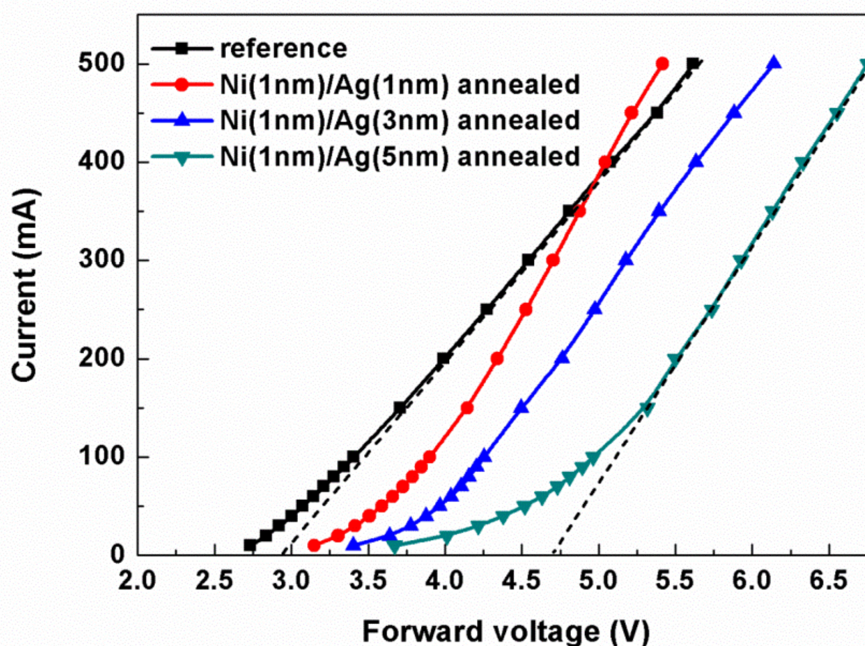

Figure 4.15 Current-voltage (I-V) curves measured for the LEDs with the conventional contact mirror and the decoupled contact mirrors with thin annealed layer of Ni (1 nm)/Ag (1 nm), Ni (1 nm)/Ag (3 nm) and Ni (1 nm)/Ag (5 nm), respectively. The intercepts of the dashed lines on the X-axis indicate the turn-on voltages.

The four-probe sheet resistance measurement is conducted on the thin Ni/Ag contact layers both before and after annealing. As shown in Table 4.1, the thin Ni/Ag layer shows low sheet resistance from 4.65 kΩ/ down to 87 Ω/, which is typical for thin metal layers before the annealing process. However, sheet resistance increases to around 100 kΩ/ for all the three contact layers after annealing. The great increase of the sheet resistance implies that the contact layers are no more metals but possibly metal oxides since the annealing process is conducted in the O_2 ambient.

SIMS depth profile analysis is performed to examine the composition of the contact layers as shown in Figure 4.16. For the three decoupled contact layers, as the Ag thickness increases, Ni and Ag are inter-diffused into each other. The Ni distribution is obviously broadening with the increase of Ag thickness. Meanwhile, the O distribution coincides with those of Ni and Ag at the interface region. Based on the experimental results above, we propose the following contact formation mechanism to explain the electrical characteristics of our decoupled contact mirrors. When the Ni/Ag contact layer is deposited and annealed in O_2 ambient, they will be fully oxidized due to thin thickness of metals. As is well known, thin Ni oxide forms ohmic contact (tunneling Schottky contact) with the p-GaN at the existence of Ag since Ag helps the out diffusion of Ga atoms from p-GaN, which leaves large amount of Ga vacancies in the p-GaN and is beneficial to the ohmic contact formation. However, Ag oxide also forms a Schottky contact with the p-GaN, which adds additional voltage drop for the devices to turn on. When the Ag oxide is as thin as 1 nm, due to the tunneling effect the additional turn-on voltage is low. Therefore the forward voltage for the device with Ni (1 nm)/Ag (1 nm) contact layer is comparable to and even better than that of the device with the conventional contact mirror at high current beyond 350 mA. As the thickness of Ag increases in the Ni/Ag contact layer, thicker Ag oxide Schottky contact layer

is formed, which will add larger turn-on voltage as shown in Figure 4.15. As an illustration for the case of thick Ni/Ag contact layer, if we assume the Schottky barrier height is solely determined by the difference of work functions and no tunneling effect is considered, since the work functions of Ag oxide and p-GaN are 5.6 eV and 7.5 eV, respectively, the Schottky barrier height will be 1.9 eV. This is in good agreement with the increase of the turn-on voltage for the device with 1 nm Ni/5 nm Ag contact layer as shown in Figure 4.16. Therefore, as an optimized Ni/Ag contact, a thin layer of Ag is desired which on one side can assist the Ga out diffusion and Ga vacancy formation, and on the other side can avoid the formation of the thick Ag oxide layer and reduce the turn-on voltage.

Besides the forward voltage, low reverse leakage current is also critically important for high-performance of LEDs. At 3 V reverse bias, the leakage currents for the reference, Ni (1 nm)/Ag (1 nm), Ni (1 nm)/Ag (3 nm), Ni (1 nm)/Ag (5 nm) samples are 4.8×10^{-8} A, 1×10^{-9} A, 5×10^{-9} A, 7×10^{-9} A, respectively. The lowest reverse leakage current was observed in the proposed sample with Ni (1 nm)/Ag (1 nm), which has the superior electrical performance.

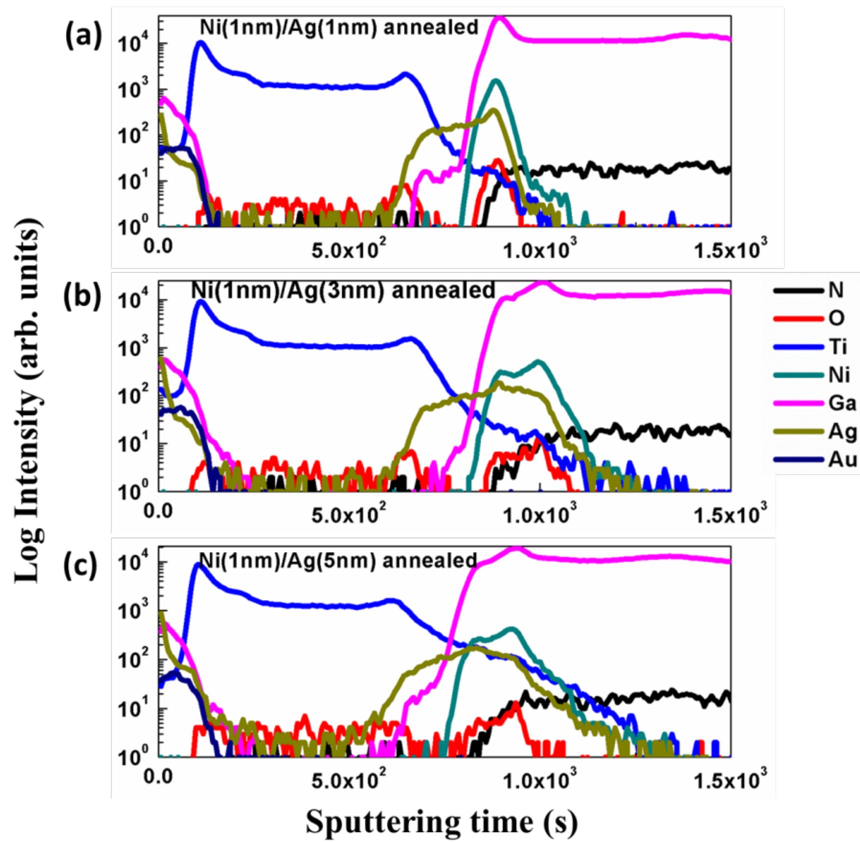

Figure 4.16 SIMS depth profiles of the decoupled contact mirrors with thin annealed layer of (a) Ni (1 nm)/Ag (1 nm), (b) Ni (1 nm)/Ag (3 nm) and (c) Ni (1 nm)/Ag (5 nm), respectively.

Table 4. 1 Sheet square resistance of thin contact layers on top of p-GaN before and after annealing (Ω/□).

Type	Non-annealed	Annealed
Ni (1 nm)/Ag (1 nm)	4.65k	100.9k
Ni (1 nm)/Ag (3 nm)	2.04k	97.98k
Ni (1 nm)/Ag (5 nm)	87	97.24k

4.2.4 Conclusions

A novel decoupled contact mirror concept for the Ni/Ag/Ti/Au reflector of InGaN/GaN LEDs has been proposed and demonstrated. Both high reflectivity and low forward voltage can be achieved at the same time through the proposed decoupled contact

mirror, which significantly improves the optical power performance of the LEDs. Through SEM and SIMS measurements, the effectiveness of the proposed contact mirror on suppressing the Ag agglomeration and the Ag intermixing has been proved. The mechanism of the decoupling of the contact and the mirror has also been investigated in detail. This new method provides an effective way to fabricate high performance contact mirrors, which will contribute to the application of high efficient solid-state lightings.

4.3 Device design using modulated ohmic contact

4.3.1 Introduction

The efficiency of InGaN/GaN-based flip-chip LEDs increases greatly with the improvement of the LEE, which is realized through designing different types of reflective ohmic contact mirror [72, 91, 94]. For LEDs with this kind of structure, the light is reflected by the mirror on p-GaN and extracted from the sapphire side, in which the mirror is extraordinarily important. Since silver has larger reflectivity when compared with different metallic reflectors in the visible wavelength range, it is usually used as the reflective contact mirror [100]. However, poor adhesion and work function mismatch between silver and p-GaN are two obstacles preventing the direct use of silver as mirror layer [93, 101]. A thin Ni layer inserted between silver and GaN is great choice to alleviate the adhesion problem and make up for the work function mismatch after undergoing high temperature annealing [97]. However, the silver is very easy to oxidize and agglomerate after annealing, which severely deteriorates the mirror performance as a tradeoff [102]. Besides Ni, indium tin oxide (ITO) layer can also be inserted between p-GaN and silver to be used as ohmic contact layer for its superior performance, such as high electrical conductivity, high transparency in the visible spectral and stable chemical properties [103]. Nevertheless, the role of ITO layer in those LEDs is not carefully investigated and the underlying physics for ohmic contact formation

has not been discussed.

In this work, we design a set of experiment with the incorporation of a thin ITO layer on the p-GaN surface and investigate the interfacial layer that forms between the p-GaN and pure silver. With the optimized parameter in this study, we have achieved high performance mirror with high reflectivity, which is almost the same as the pristine silver layer, and low forward voltage, which is comparable with Ni/Ag or thick ITO/Ag combinations. The formation of $InGa_xN_yO_z$ interfacial layer is analyzed using various characterization methods and a model is proposed to illustrate the physics for ohmic behavior.

4.3.2 Experiments

Standard LED chips are fabricated using epi-wafers grown by MOCVD through a series of standard fabrication techniques. First, one wafer was cut into four pieces, while three pieces of the wafer were deposited with ITO of 1 nm, 5 nm and 10 nm, respectively, and the last one was kept as the reference. Then, the samples underwent annealing at 630 ^oC in oxygen ambient for 1 minute. After that, a layer of Ag (200 nm)/Ti (50 nm) was sputtered on top as the reflective mirror of the contact. The mesa size was defined as 1×1 mm^2 and etched by inductively coupled plasma (ICP). Ti/Ag/Ti/Au layer were deposited as the electrodes for the devices by e-beam evaporator. The samples for reflectivity measurement were prepared by depositing thin ITO layers/Ag mirror on top of double-side polished sapphire substrates, and the measurements were conducted using a Perkin Elmer Lambda 950 UV/VIS/NIR Spectrophotometer system. The current-voltage (*I-V*) characteristics were measured by a SC-200-mm probe station and the optical output power was measured using an ocean optics spectrometer, which is attached with an integrating sphere. Surface morphologies of ITO layers with different thicknesses were characterized using atomic force microscopy (AFM) (scanning Probe Microscope Model DI dimension V), surface sheet

resistance was measured through four-probe method by a sheet resistance & resistivity equipment, and the binding energies of elements in the surface material were achieved by a home-made X-ray photoelectron spectroscopy and Ultraviolet photoelectron spectroscopy (XPS and UPS) system.

4.3.3 Results and discussions

Figure 4.17 (a) shows the reflectivity of thin ITO layers with various thicknesses after silver deposition. The reflectivity of the mirror with 1 nm ITO insertion layer is almost the same as that of the pristine silver mirror. As the thickness of ITO insertion layer increases to 5 nm and 10 nm, the reflectivity of the mirror starts to decrease. Even though the change of the reflectivity value is small here due to the thin thickness of ITO insertion layers, it clearly shows the trend that with thicker ITO insertion layer, the reflectivity of the mirror degrades. Therefore, the ITO insertion layer should be made as thin as possible for better optical performance. The optical performance of the mirrors with thin ITO insertion layers here is much better than that of annealed Ni/Ag mirror, for which the reflectivity is even lower than 80% at 450 nm [104]. The *I-V* characteristic of flip-chip LEDs with different thicknesses of ITO insertion layers is shown in Figure 4.17 (b). From the *I-V* curve, we can see that without ITO insertion layer, the forward voltage is much higher, indicating the poor ohmic contact formation between silver mirror and p-GaN. When the thin ITO layer is inserted, the *I-V* performance is greatly improved even when the thickness is just 1 nm. The lowest forward voltage among the three samples with ITO layers happens when the thickness of ITO insertion layer is 5 nm. The mechanism about why the ITO with 5 nm can achieve the best electrical performance will be discussed in the following part.

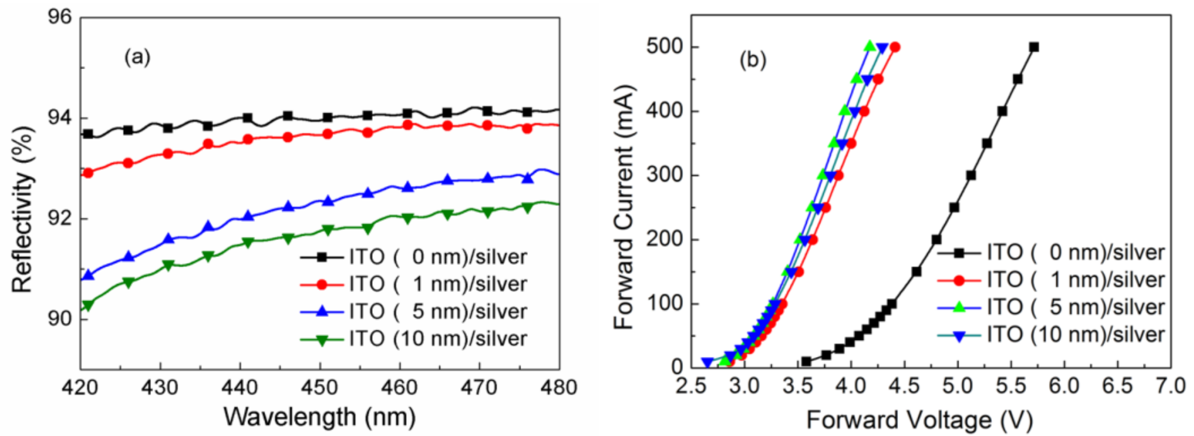

Figure 4.17 (a) Reflectivity for ITO thin layers with different thicknesses after annealing and silver mirror deposition and (b) *I-V* curve of flip-chip LEDs with different thicknesses of ITO.

Figure 4.18 (a) shows the optical output power enhancement ratio of LEDs with various thin ITO insertion layers when compared with the reference from 100 mA to 500 mA, while the inset shows the value with current from 30 mA to 100 mA. For the lower current range in the inset, the optical power for LED with 10 nm ITO is lower than other samples for its lowest mirror reflectivity. With increasing current, the LED without ITO layer gradually becomes smaller than others, since the sample has largest forward voltage and thus more heat will be generated in the process [105]. Among the three samples with different ITO insertion layers, the one with 1 nm ITO has the largest optical output power, which is consistent with the reflectivity of the ITO mirrors shown in Figure 4.17 (a). Figure 4.18 (b) shows the wall-plug efficiency enhancement ratio for samples with different ITO layers when compared with the reference, with inset showing the curve at low current from 30 mA to 100 mA. All the samples with ITO layers present obviously superior performance than the one without ITO layer in the whole injection current range. At operation current, for all the samples with ITO layers, the one with 5 nm shows better performance than other results due to reduced forward voltage. Apparently, the insertion of thin ITO layers between silver and

p-GaN surface changes the electrical property while maintains the high optical performance of the silver mirror and thus leads to the improved overall device performance. The optimized thickness of ITO is 5 nm instead of 1 nm or 10 nm. Thus, the mechanism behind the phenomenon is worth to be investigated.

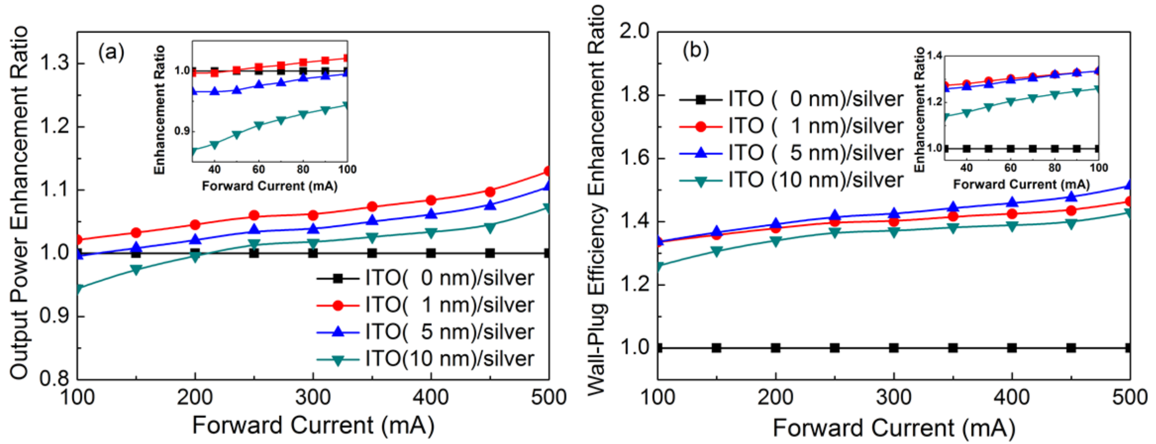

Figure 4.18 (a) Optical output power and (b) wall-plug efficiency enhancement ratio for samples with different ITO layers when compared with the reference, with inset showing the same curve at low current range from 30 mA to 100 mA.

Figure 4.19 shows the atomic force microscopy (AFM) images of the thin ITO layers deposited on p-GaN surface before and after annealing. For the 1 nm ITO layer before annealing in Figure 4.19 (a), the surface is featured by step-flow structures [106], which originates from the p-GaN surface and indicates the conformal deposition of the thin ITO layer. When the ITO layer increases to 5 nm and 10 nm, the surface morphologies turn into grain structures as shown in Figures 4.19 (b) and (c). The conformality is lost and the granular nature of ITO layers starts to dominate when the thickness of ITO increases. After annealing, the surface morphology of the sample with 1 nm ITO layer maintains the step-flow characteristic as shown in Figure 4.19 (d), while the surface morphology of the sample with

5 nm ITO layer turns from granular structures into step-flow structures as shown in Figure 4.19 (e). Even for the sample with 10 nm ITO layer, the surface morphology also experiences changes from granular characteristic to step-flow nature as shown in Figure 4.19 (f). The change in the surface morphology after annealing allows us to reasonably assume that: during annealing (1) the process of interfacial atomic inter-diffusion and inter-mixing takes place, and (2) for 1 nm and 5 nm ITO layers, the atomic inter-diffusion and inter-mixing is thorough, which means the whole ITO layer has turned into the interfacial layer and no pure ITO layer is left, and (3) for the 10 nm ITO layer only underlying part of the layer turns into the interfacial layer and the rest of the top ITO layer is left intact. The conjecture of the formation of the interfacial layer by the atomic inter-diffusion and inter-mixing has been supported by other experimental results as follows.

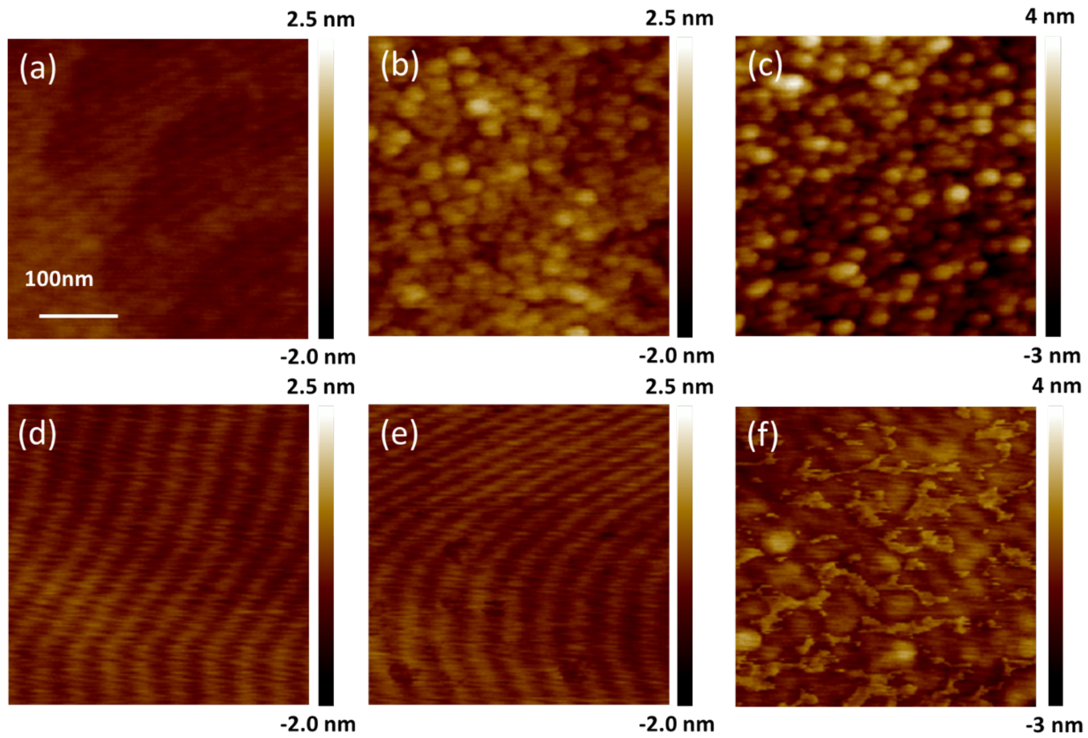

Figure 4.19 AFM images of p-GaN surface after ITO deposition with 1 nm ITO (a) before and (d) after annealing, 5 nm ITO (b) before and (e) after annealing, 10 nm ITO (c) before and (f) after annealing.

The sheet resistances of the thin ITO layers deposited on p-GaN surface before and after annealing are listed in Table 4.2. Before annealing, the sheet resistance for the sample with 1 nm ITO layer is around 2.9 MΩ/□, while it is around 150 KΩ/□, for the samples with 5 nm and 10 nm ITO layers. The sheet resistance of 2.9 MΩ/□ is at the same order of magnitude with the value of p-GaN, which implies that the probe may penetrate the 1 nm ITO layer during the measurement. The sheet resistance of 150 KΩ/□ is the typical value for the unannealed ITO thin layers. After annealing, the sheet resistances for all the three samples become much smaller. For the sample with 1 nm ITO layer the sheet resistance is around 116 KΩ/□, more than one order of magnitude lower than that before annealing. This strongly

indicates that a highly conductive interfacial layer is formed on the p-GaN surface during the annealing through atomic inter-diffusion and inter-mixing. The sheet resistance becomes even smaller as the ITO layer thickness increases, which may imply that the interfacial layer becomes more conductive due to the larger amount of ITO supply during the interfacial layer formation. We have to bear in mind that for the sample with 10 nm ITO, a certain thickness of ITO has been left as shown in Figure 4.19 (f), which also contributes to the conductivity and thus results in the lowest sheet resistance together with the interfacial layer

Table 4.2 Sheet resistance of ITO layers on top of p-GaN before and after annealing (Ω/□).

Type	Non-annealed	Annealed
ITO (1 nm)	2.858 M	115.9 K
ITO (5 nm)	153.5 K	22.88 K
ITO (10 nm)	168.2 K	1.556 K

In order to uncover the chemical properties of the interfacial layer, XPS analysis was performed on the samples after annealing. Wide-scan spectrum of the binding energies for all the samples is shown in Figure 4.20 (a). For the sample without ITO layer, only Ga 2p and N 1s signals, which originate from the clean GaN surface, are observed. For samples deposited with 1 nm and 5 nm ITO thin layers, the signals from Ga 2p and N 1s can still be seen even their signal intensities become weaker with the increase of ITO thickness. Besides, signals from O 1s, Sn 3d and In 3d have also been observed. For the sample with 10 nm ITO layer, signals from O 1s, Sn 3d and In 3d are clearly observed while the signal of Ga 2p is very weak and the signal of N 1s is hardly observed. From these results, it can be deduced that when the ITO thickness is more than 10 nm, the surface part is still pure ITO layer and the only the bottom part participates in the atomic inter-diffusion and inter-mixing process with the underlying GaN layer and converts into the interfacial layer. When the ITO thickness

is as thin as 1 nm and up to 5 nm, the process of atomic inter-diffusion and inter-mixing consumes the whole ITO layer and the surface region of the underlying p-GaN and transforms them into the interfacial layer. The details in the binding energy change for Ga 2p, N 1s and In 3d of the samples are shown in Figures 4.20 (b), (c) and (d), respectively. It can be seen from Figures 4.20 (b) and (c) that the binding energies for Ga 2p and N 1s for the samples coated with 1 nm and 5 nm ITO layers shift to lower energy compared to the sample without ITO coating. On the other hand, the binding energies for In 3d for the samples coated with 1 nm and 5 nm ITO layers are quite close to each other but much larger than that for the sample coated with 10 nm ITO layer, as shown in Figure 4.20 (d). The changes in the binding energy of Ga 2p, N 1s and In 3d for samples coated with 1 nm and 5 nm ITO layers show that the interfacial layer composes of Ga, In, N, and other elements with inter-atomic chemical bonds, when compared with the samples without ITO coating and coated with 10 nm ITO. The changes in the binding energy are in favor of the formation of ohmic contact. For example, the shift of the binding energy of Ga 2p in the interfacial layer to lower energy with increasing thickness reflects that the surface Fermi level shifts to the valence band edge and results in reduction in the band bending of p-GaN [107, 108].

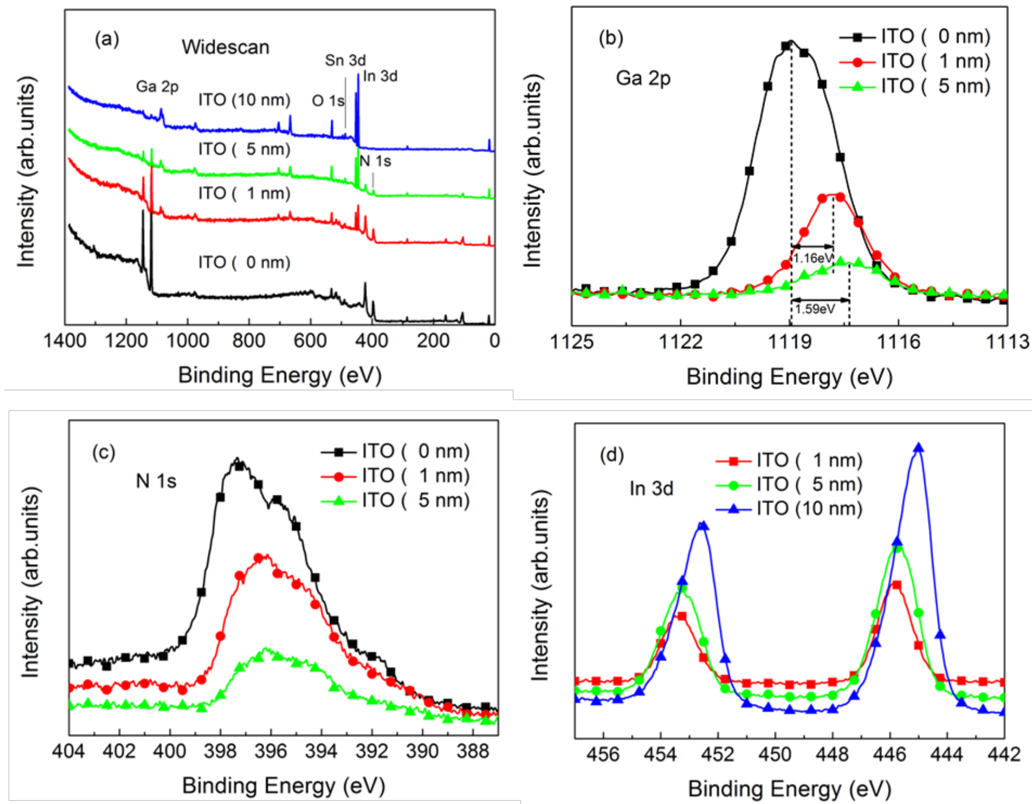

Figure 4.20 XPS wide scan of all the elements (a), Ga 2p core spectra (b), N 1s core spectra (c) and In 3d core spectra (d) for the samples with different ITO thickness after annealing.

Based on the analysis above, we put up a theoretical model as an explanation for the ohmic contact, which is formed between silver and p-GaN with the help of thin inserted ITO layers. As shown in Figure 4.21, illustrations of all the elements for the contact mirrors are depicted to show the distribution of elements. As shown in Figure 4.21 (a), the interface is sharp and smooth, since no inter-diffusion happens without undergoing annealing after silver deposition. In Figures 4.21 (b) and (c), the atomic inter-diffusion and inter-mixing between the p-GaN and ITO are complete, which means the thin ITO layers are totally inter-mixed with p-GaN. In the process, Ga atoms diffuse out to form a thin interfacial layer composed of $InGa_xN_yO_z$ and leave Ga+ vacancies at the surface of p-GaN [109]. However, small islands

made of $InGa_xN_yO_z$ are formed instead of continuous film when the thickness of ITO is only 1 nm, as shown in Figure 4.21 (b). Some of the p-GaN is still in direct contact with silver, and this will add extra forward voltage when compared with the sample with 5 nm ITO. This can also explain the high sheet resistance of sample with 1 nm ITO when compared with that of 5 nm ITO. In Figure 4.21 (d), bottom part of ITO mixes with p-GaN and top part is left intact. The different profiles of the p-GaN surfaces with ITO layer of different thickness will result in different electrical properties as discussed in the following analysis.

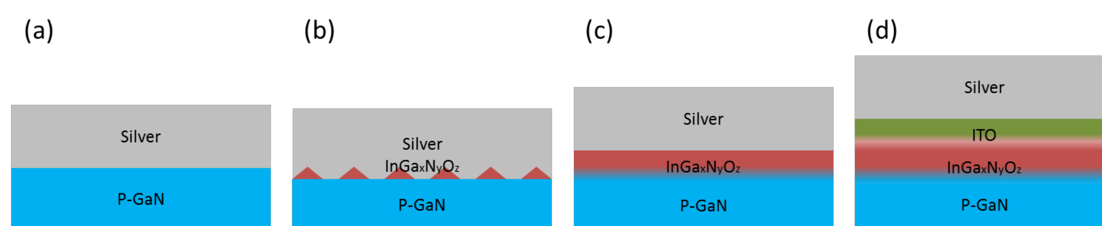

Figure 4.21 Schematic diagrams of element mixing for contact mirror with (a) no ITO layer, (b) 1 nm annealed ITO layer, with a formation of island-like $InGa_xN_yO_z$ layer, (c) 5 nm annealed ITO layer, with a formation of $InGa_xN_yO_z$ layer, and (d) 10 nm annealed ITO layer.

Figures 4.22 (a) and (b) show the energy band diagrams of samples with and without the interfacial layer at equilibrium state. Formation of ohmic contact between metal and p-GaN can only be realized when its work function is larger than p-GaN [37]. Since the work function of silver and p-GaN are 4.25 eV [110] and 7.5 eV [111], respectively, a Schottky contact is formed between them, as shown in Figure 4.22 (a), while the Schottky barrier height (SBH) is 3.25 eV. Thus, free carriers are not easy to pass through the interfacial layer. For the LED with a thin ITO layer deposited and annealed, Ga+ vacancies will be generated [109] on the top of p-GaN as stated. Binding energy of Ga 2p core level decreases as a result of Ga+ vacancies generation, as shown in Figure 4.20 (b). When compared with the sample

without ITO, the binding energy of Ga 2p core level shifts towards lower side by 1.16 eV for the sample with 1nm ITO, and 1.59 eV for the sample with 5 nm ITO. The difference of Ga 2p core level binding energy results in large energy band bending with the value larger than 3.25 eV [112]. In this case, the direction of the band bending for the contact changes from downward to upward, which facilitates the ohmic contact formation between the p-GaN and metal, as shown in Figure 4.22 (b). For the sample with 10 nm ITO layer, there still exists an unconsumed ITO layer between silver and the interfacial layer, which will add more parasitic resistance and result in higher forward voltage as shown in Figure 4.17 (b) due to small work function mismatch.

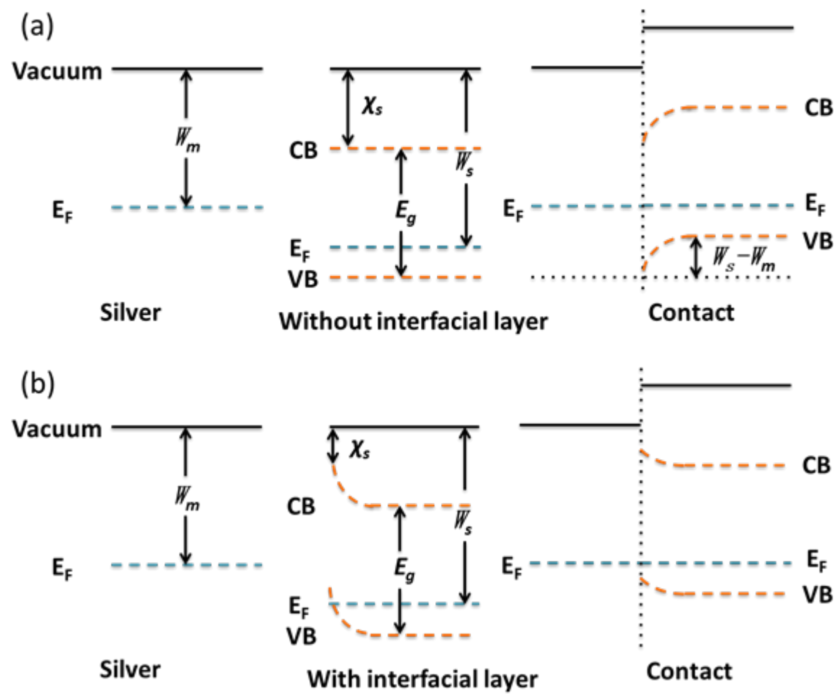

Figure 4.22 Schematic band diagrams of silver and p-GaN contact with (a) no interfacial layer, and (b) $InGa_xN_yO_z$ interfacial layer.

4.3.4 Conclusions

To summarize, a set of experiments have been designed with different ITO insertion

layers to promote the generation of $InGa_xN_yO_z$ interfacial layer through thermal annealing process. A complete $InGa_xN_yO_z$ layer is formed in the situation of optimized design, which interfaces directly with the p-GaN and intact silver, and maintains the high reflectivity of the intact silver and high-quality ohmic contact. InGaN/GaN-based LEDs, which adopt the optimized design, perform superior in both electrical and optical aspects and yield the highest wall-plug efficiency at operation current.

4.4 Summary

In this chapter, we have introduced the fabrication process in our group which provides a sound platform to produce device chips with high repeatability and high reliability. Three different chips are fabricated and characterized, which reveal our capability to achieve high-performance LEDs. Then, we utilized two methods to optimize the mirror contact to improve the performance of flip-chip structure LEDs. For the first method, a decoupled mirror contact is applied, in which the ohmic contact and the high reflective mirror are realized separately. For the second method, the ohmic contact is realized through modulating the $InGa_xN_yO_z$ interfacial layer, during which the ITO layer acts as sacrificial layer instead of the contact layer, and the high reflectivity mirror is also achieved since the thickness of ITO is very thin.

Chapter 5

Development towards InGaN/GaN-based microwall LEDs

In this chapter, firstly we elaborate the advantages of microwall LEDs, in which semi-polar or non-polar facet is exposed, followed by the description of selective area growth (SAG) method. Then, some preliminary results about GaN microwall growth are reported, in which the growth process is modulated by both temperature and NH_3 flow rate and both structural and optical properties are characterized. After discussion about the preparation process for GaN microwall substrates, the full-structure microwall LED epi-wafer is grown and some related experimental results are presented.

5.1 Microwall structured LEDs grown by selective-area growth

Typically, InGaN/GaN-based LED epi-layers are grown on foreign substrates, such as sapphire, 6H-SiC and Si [113], and polar structures are typically formed. This kind of LEDs suffer from polarized electric field, which decreases the spatial overlap of electron and hole, and thus sacrifice the IQE and contribute to the efficiency droop [114, 115]. In addition, the Auger recombination is more severe for higher carrier concentration since the critical thickness of quantum well is limited due to the lattice mismatch between GaN and InGaN [116]. However, for the InGaN/GaN-based LEDs grown on the semi-polar or non-polar facet, the efficiency droop will be greatly reduced benefiting from the decrease of the polarized electric field [117]. The internal strain can also be alleviated, and thus the critical thickness of quantum well is increased, which results in a smaller carrier concentration and alleviates Auger recombination effect [52]. Although the homo-epitaxial free-standing GaN substrate is the best choice to grow InGaN/GaN-based LEDs with high crystalline quality [118, 119], the substrate with specific exposed planes is very expensive and not easily accessible [120].

In order to grow semi-polar or non-polar InGaN/GaN-based LEDs economically, selective area growth (SAG) method is developed to provide an effective path towards various LED structures with different crystal facets exposed on c-plane sapphire substrates

[121]. Figure 5.1 shows the GaN pyramid structure grown by this method, which was firstly reported by Kato et al. [122]. During the growth process, the openings are made on top of the substrate with dielectric material as the mask, and the growth is precisely controlled through the openings. The mechanism for the selective growth is due to the particularly low supersaturation of the reactant on the dielectric mask, when compared with the openings. After filling the space, the morphology is controlled by the growth parameters, such as pressure, temperature and precursor flow rate, and determined by the growth rate of different crystal facets.

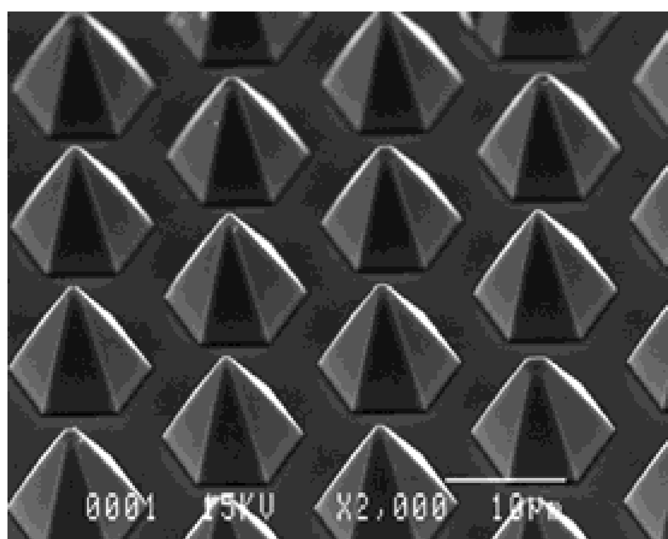

Figure 5.1 Selective area growth of GaN. [121]

5.2 Structural and optical properties of microwalls

5.2.1 Introduction

For the planar structure InGaN/GaN-based LEDs, the external quantum efficiency decreases with increasing current, which is widely known as efficiency droop and this phenomenon hindered their application in most lighting aspects [46]. Many mechanisms accounting for the phenomenon have been put up, such as Auger recombination [123], large

polarized electric field [124] and current crowding effect [125]. In order to address this problem, microwall LEDs, which expose semi-polar or non-polar facet and accommodate larger thickness of quantum wells, have great potential to alleviate the efficiency droop. If different morphologies of GaN microwall templates can be prepared economically and flexibly, and the material quality for different structures can be understood scientifically, it would become much easier for us to achieve microwall LEDs, and thus alleviate the efficiency droop.

In this work, we adopted the SAG method to grow semi-polar and non-polar GaN microwall structures, which were modulated by growth temperature and NH_3 flow rate. Stress, defects and optical properties were characterized, respectively. The mechanisms for different morphologies and different properties grown under different conditions were explained in detail.

5.2.2 Experiments

As shown in Figure 5.2, starting substrates were prepared by a series of fabrication techniques. First, a thin nucleation layer of GaN was grown on top of sapphire substrate, followed by a 4 μm-thick undoped GaN. Then, a 200 nm-thick SiO_2 was deposited by plasma enhanced chemical vapor deposition (PECVD) system. The 5/5 μm strips/openings were oriented to the <1 -1 0 0> direction, which were prepared by photolithography and etched by reactive ion etching (RIE) system. After the substrates were prepared, they were loaded back to the MOCVD system. In all cases, the growth pressure was 250 torr, the carrier gas was H_2 and the growth time was half an hour. Continuous growth method was applied, in which TMGa and NH_3 were injected into the chamber at the same time. The growth temperature and the flow rate of TMGa and NH_3 are listed in Table 5.1. The surface morphologies and the material quality were featured by a series of characterization techniques. SEM was used

to investigate the surface morphologies. Raman spectra at different locations of microwall structures were characterized to study the in-plane stress by a LabRAM HR Evolution Raman Spectrometer. The crystal qualities were evaluated by the rocking curves through ω scan of (002) and (102) reflecting planes using a Philips HRXRD system and PL measurements were carried out to investigate their optical properties through nanometrics PL-thickness mapper system.

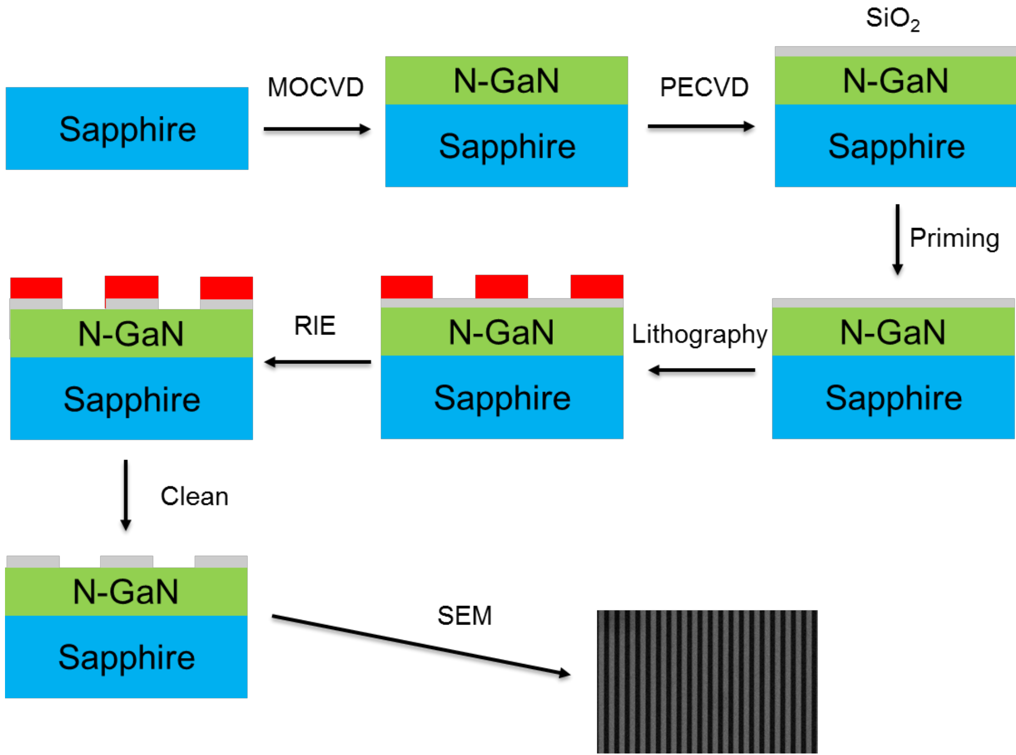

Figure 5.2 Schematic illustration of the process used to prepare the starting substrates for GaN microwall growth.

Table 5.1 Sets of experiments carried out and parameters used in this work.

Exp.set	**Temp(ºC)**	**NH3 (sccm)**	**V/III ratio**
A	1135-1285	4000	800
B	1185	400-4000	80-800

5.2.3 Results and discussions

5.2.3.1 Effect of growth temperature

A series of temperatures, from 1135 °C to 1285 °C (thermocouple reading in the susceptor) with 50 °C as the interval, have been applied in the growth process for experiment set A. Figure 5.3 shows SEM morphologies of GaN microwalls grown under different temperatures. From Figure 5.3 (a) to Figure 5.3 (d), the structures seen from the top view of all the samples with different temperatures are shown, accompanied by their cross section views as shown from Figure 5.3 (e) to Figure 5.3 (h). For sample grown at 1135 ℃, Figure 5.3 (a) shows the top view of the morphology, from which we can see a narrow line and some random pits, while Figure 5.3 (e) shows a nearly triangle cross-section. The poor crystal quality is indicated from the random pits generated on the triangle GaN microwalls. When the temperature increases by 50 ℃ as shown in Figures 5.3 (b) and (f), the surface become much smoother and defects are greatly decreased. The width of the top line becomes wider than that in Figures 5.3 (a) and (e) and the cross section of the triangle gradually transforms to trapezoid. According to Wulff's law [126], the slowest growth rate of the crystal plane determines the shape of the structure. At low temperature, the diffusion of the hydrogen was slow and most of them stayed on the semi-polar facet, which passivated the growth of the semi-polar plane [127]. With increasing temperature, the passivated atoms on the semi-polar plane became more active, parts of the passivation effect was released and the relative growth

rate was increased when compared with c-plane [128]. When the temperature is further increased to 1235 °C, as shown in Figures 5.3 (c) and (g), the top width becomes larger and the cross section even transforms to rectangle when the temperature increases to 1285°C, as shown in Figures 5.3 (d) (h) [129, 130].

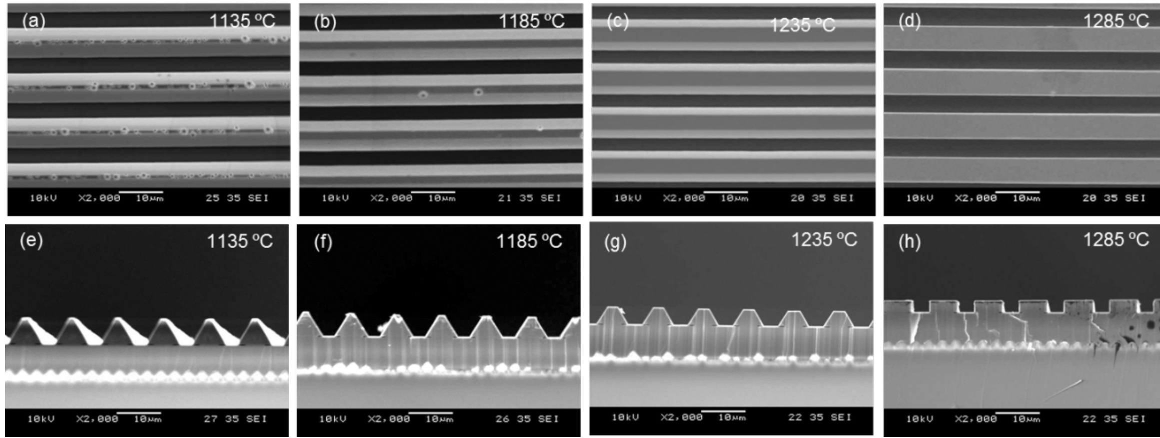

Figure 5.3 SEM images grown by continuous MOCVD techniques under different temperatures for both top views at (a) 1135 °C, (b) 1185 °C, (c) 1235 °C, (d) 1285 °C and cross section views at (e) 1135 °C, (f) 1185 °C, (g) 1235 °C, (h) 1285 °C.

Raman spectroscopy has been widely employed to determine the material quality and monitor the in-plane stress for III-nitride semiconductors [131]. The E_2 (high) phonon peak is used to indicate the in-plane stress [132] and the value is believed to be 567.6 cm^{-1} in strain free GaN [133]. The strain inside the structure can be calculated according to [134] $\sigma = \frac{\Delta\omega}{4.3}(cm^{-1}GPa^{-1})$, where σ is the biaxial stress and Δω is the offset of the E_2 phonon peak when compared with the strain free samples. Figure 5.4 shows the normalized Raman spectrum with E_2 (high) phonon peaks for all the samples grown under different temperatures, in which A means the bottom GaN, B means the sidewall GaN and C means

the top GaN. All the peaks at different locations have a value larger than 567.6 cm^{-1} which means thermal compressive stress dominates in the GaN structures [135, 136]. However, when compared with the bottom GaN, the Raman shifts on the microwall structures have smaller values, which indicate the relaxation of the in-plane strain for the newly grown GaN microwalls. As shown in Figure 5.4 (a), we can see that top GaN shows smaller Raman shift than that of the slanted sidewall, which means the relaxation of the stress is more obvious on the top of GaN strips. Different strain distribution on different facets is explained by elastic moduli principle [137, 138]. The same trend continues with increasing temperature as shown from Figures 5.4 (b) to (d).

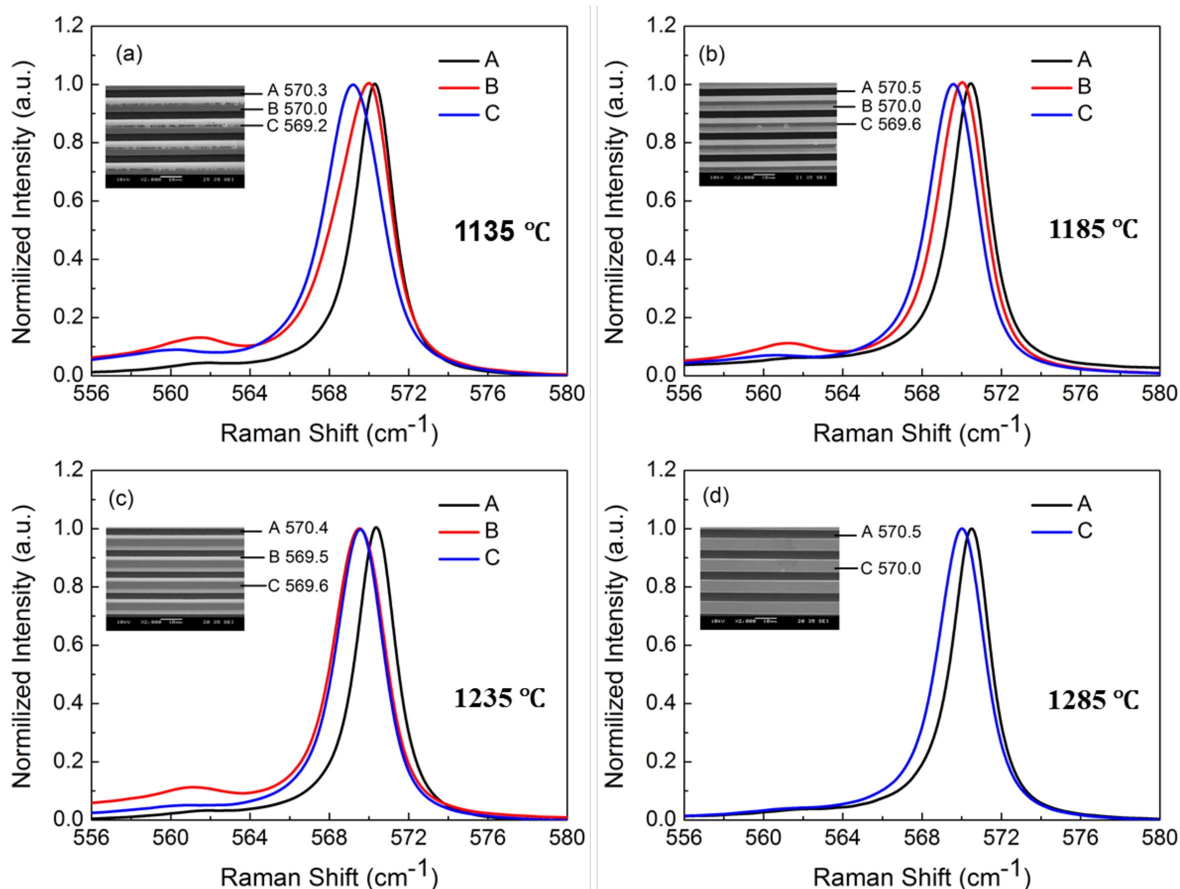

Figure 5.4 Raman spectrum of E_2 (high) phonon peaks for samples grown at (a) 1135℃, (b) 1185℃, (c) 1235℃ and (d) 1285 ℃ respectively.

Figure 5.5 shows the HRXRD rocking curves of the GaN microwalls grown at different temperatures. The approximate peaks for (002) and (102) are 17.3 degree and 24.1 degree respectively, which indicate the wurtzite structure of the crystal. As we know [59], the rocking curve for the asymmetric (102) reflecting plane can directly reveal material's reliable structural quality, because its FWHM corresponds to all threading dislocations including edge dislocations. Meanwhile, the FWHM of the rocking curve for the symmetric (002) reflecting plane only reflects the screw and mixed-type dislocations [60]. The FWHMs for (102) reflecting plane are 0.1 and 0.09 for the samples grown at 1185 ℃ and 1285 ℃, respectively, which means the dislocations generated at high temperature are reduced. From

the peaks as shown in Figure 5.5 (a), the value is 17.24 for GaN at low temperature and 17.36 for GaN at high temperature, which means more compressive strain is generated when compared with the triangle structures at low temperature [139]. The strain analysed through the rocking curves is also consistent with the Raman analysis stated above.

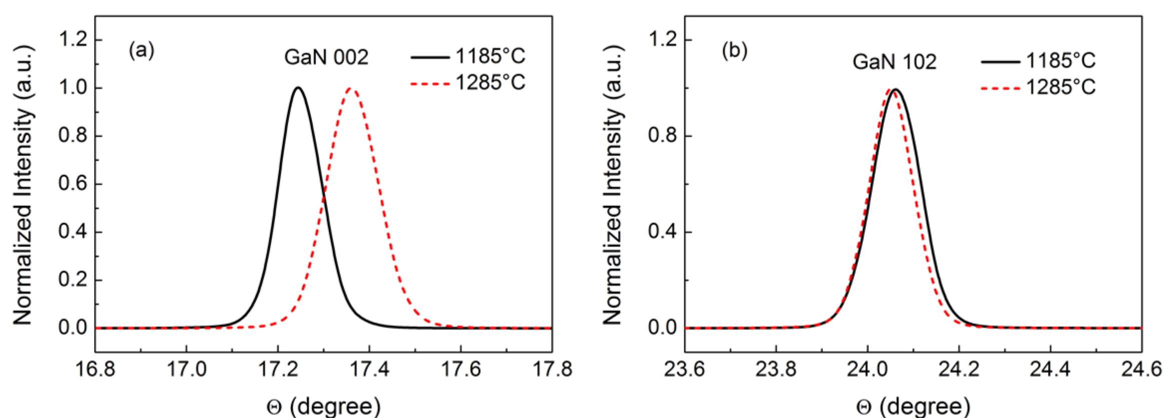

Figure 5.5 HRXRD rocking curves of (a) the symmetrical (002) reflection and (b) the asymmetrical (102) reflection planes for GaN microwalls grown at temperature of 1185 ℃ and 1285 ℃.

Figure 5.6 presents the room-temperature PL spectra for all the GaN microwalls grown at different temperatures, with a planar structure grown at 1285 ℃ as the reference. Typically, near-band-edge (NBE) emission, stacking faults emission, donor-acceptor pair (DAP) recombination and their phonon replicas are observed in GaN samples [140]. For the planar structure reference, there are two peaks appeared, which dominate at 3.445 eV and 3.364 eV, and they correspond with the NBE emission and DAP emission. For the microwall samples, at 1135 ℃, the PL spectrum peaks at 3.412 eV [141], which corresponds to the basal stacking fault emission. With increasing temperature, the emission peaks have a redshift, with the peak value ranging from 3.349 eV to 3.364 eV, which is mainly originated from the DAP emission, since more oxygen will be incorporated as donors with increasing temperature.

After increasing the temperature further, the NBE emission is enhanced resulting from the improved material quality as indicated from the XRD rocking curves.

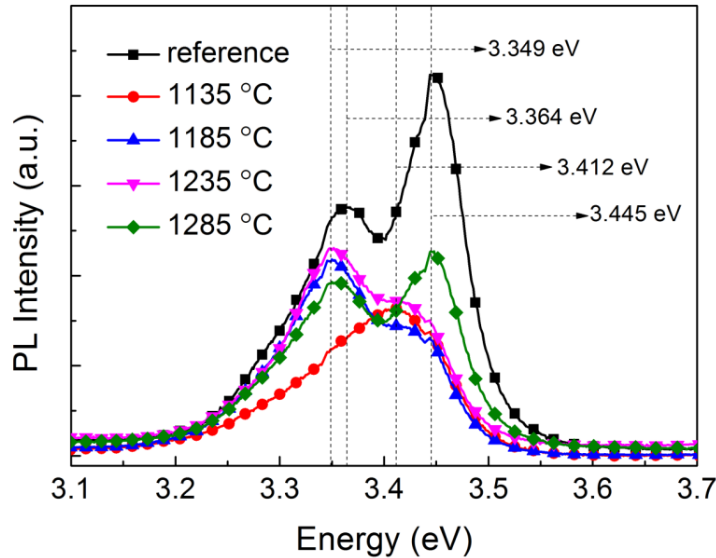

Figure 5.6 Room temperature photoluminescence for samples grown under different temperatures, with planar structure grown as reference.

5.2.3.2 Effect of NH_3 flow rate

In experiment set B, the flow rates of NH_3 for microwall growth are 400, 700, 1000 and 4000 sccm, respectively. Figure 5.7 shows the SEM morphologies of GaN microwalls grown under different NH_3 flow rates. From Figures 5.7 (a) to (d), the structures seen from the top view of all the samples with different NH_3 flow rates are shown, accompanied by their cross section views from Figures 5.7 (e) to (h). From Figures 5.7 (e) to (h), the morphologies evolve from a rectangle structure to a triangle structure, with increasing NH_3 flow rate. From Figure 5.7 (e), it can be indicated that growth rate of the semi-polar plane has surpassed those of the polar and non-polar planes. When we increase the flow rate of NH_3, the top of the microwall becomes a little slanted, which means that passivation effect

[128] is much easier to happen due to high NH_3 flow rate in which more H is decomposed from the NH_3. When the flow rate is further increased, the passivation effect is more severe which will decrease the growth rate of semi-polar plane. More semi-polar planes will be exposed and the top surface becomes narrower compared with that of smaller NH_3 flow rate. At last, the shape became nearly triangle when the flow rate increases to 4000 sccm.

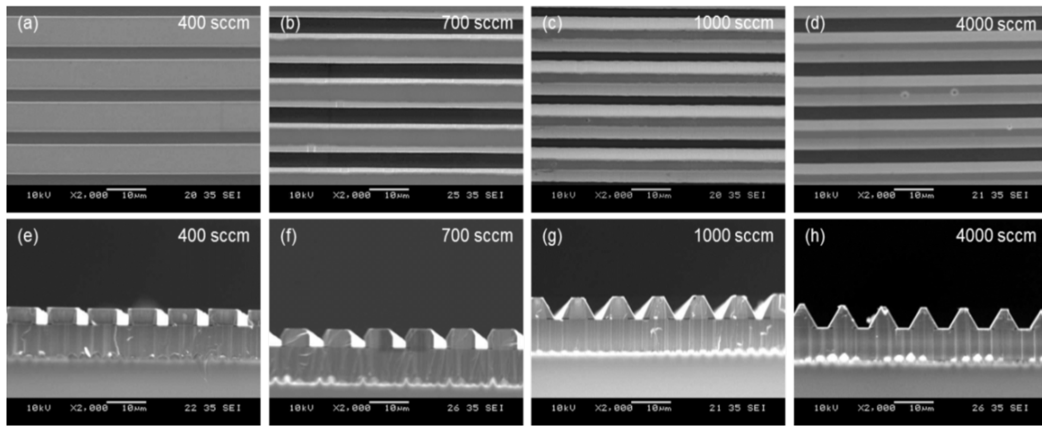

Figure 5.7 SEM images grown by continuous MOCVD techniques under different NH_3 flow rates for both top view (a) 400 sccm, (b) 700 sccm, (c) 1000 sccm, (d) 4000 sccm and cross section view (e) 400 sccm, (f) 700 sccm, (g) 1000 sccm, (h) 4000 sccm.

Figure 5.8 shows the Raman spectra for all the samples with different NH_3 flow rates with all the E_2 phonon peaks. All the peaks are shifted to the positive direction when compared with the strain-free GaN, which indicates that the thermal compressive strains are generated for all the samples. The peaks at the bottom GaN substrate ranges from 570 cm^{-1} to 570.5 cm^{-1}, while the newly grown structures always show a smaller value when compared with the bottom GaN. The strain in the semi-polar facet is larger than that in the polar facet. This result is consistent with the above analysis grown under different temperatures.

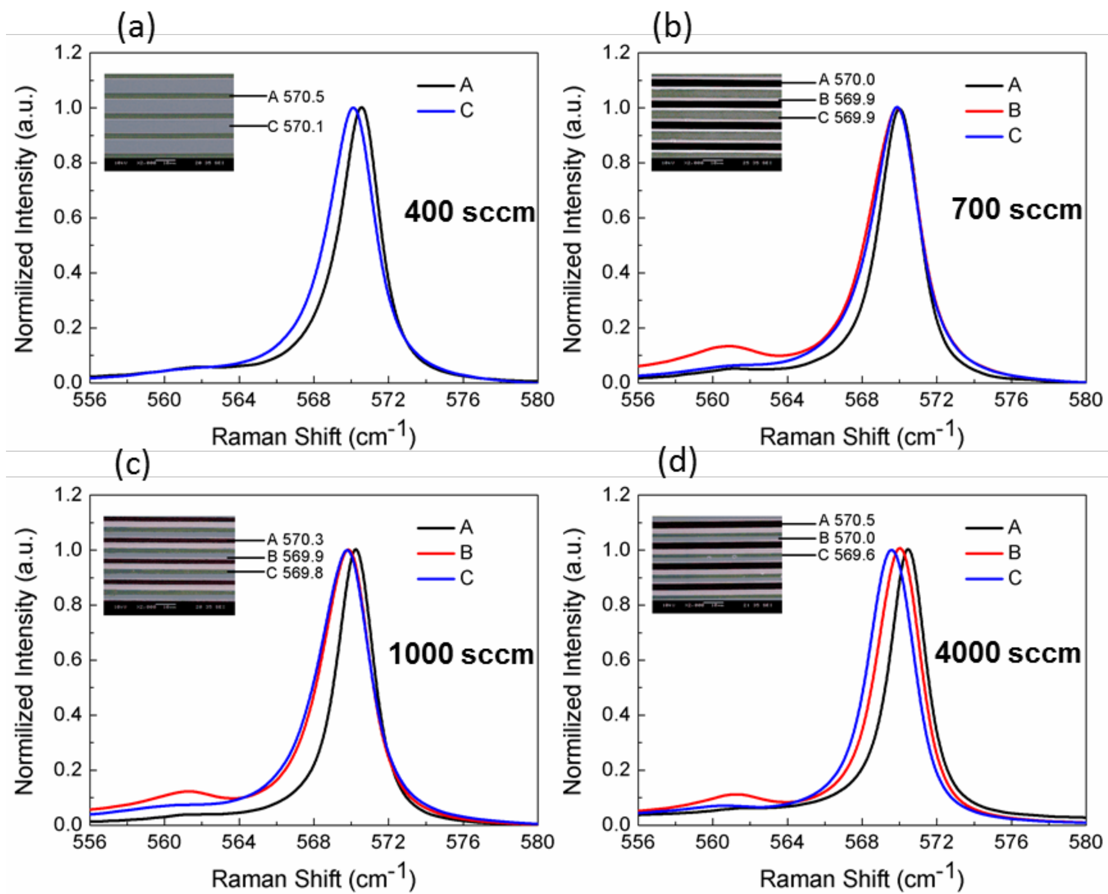

Figure 5. 8 Raman spectra of E2 (high) phonon peaks for samples grown with NH_3 at (a) 400 sccm, (b) 700 sccm, (c) 1000 sccm and (d) 4000 sccm, respectively.

Figure 5.9 shows the rocking curves of the GaN microwalls grown at different NH_3 flow rates. The FWHMs for (102) reflecting plane at different flow rates are 0.1 degree and 0.1 degree, respectively. From the results, we can conclude that dislocations do not change when the NH_3 flow rate changes. From the peaks as shown in Figure 5.9 (a), GaN with rectangle structures presents larger diffraction angle, which means more compressive strain is generated when compared with the triangle structures and this result is consistent with the Raman analysis.

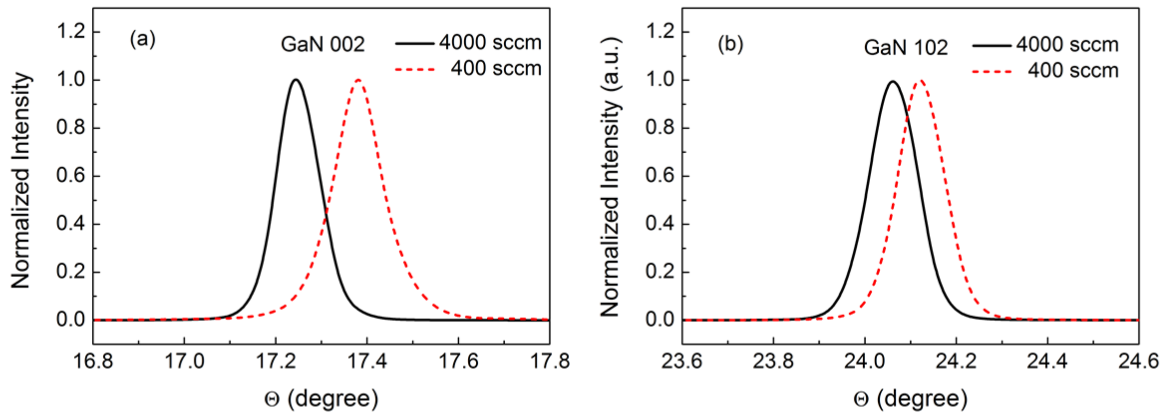

Figure 5.9 HRXRD rocking curves of (a) the symmetrical (002) reflection and (b) the asymmetrical (102) reflection planes for GaN microwalls grown under flow rate of NH_3 at 4000 sccm and 400 sccm.

As shown in Figure 5.10, the intensity of PL for samples increases with increasing NH_3 flow rate, while the peak energy shifts to a smaller value. GaN is often unintentionally n-doped due to oxygen donors arising either from diffusion from the sapphire substrate or from incorporation of impurities during growth [142]. For the samples with NH_3 flow rate of 400 sccm, the PL intensity is very low which is caused by defects and N vacancies generated in the process. Most of the photons are absorbed by the non-radiative recombination centers. When the NH_3 flow rate is increased to 700 sccm, the intensity increases and two peaks appear, with one peak at 3.445 eV as the NBE emission and the other peak at 3.412 eV, which may be caused by DAP. When the flow rate increased further, the material quality increased further and the peak from DAP shifts further to smaller value. For improved material quality, the peak caused by the DAP emission changes down to 3.349 eV when the NH_3 flow rate increased further. The red shift of all the peaks is due to the incorporation depth of the donors.

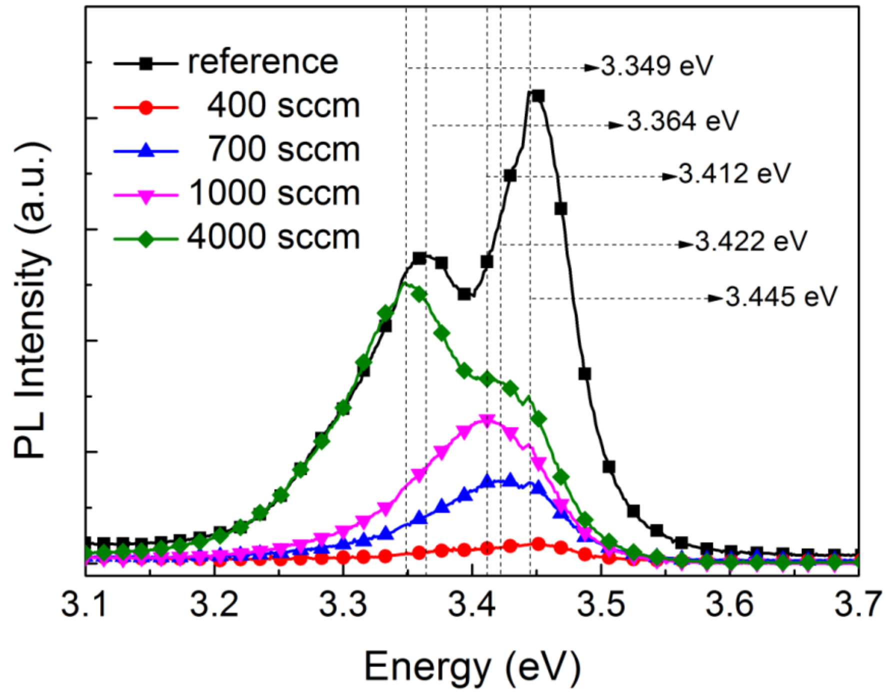

Figure 5.10 Room-temperature photoluminescence for all the samples with different NH_3 flow rates.

5.2.4 Conclusions

In summary, GaN microwalls with different morphologies have been achieved through SAG method in MOCVD system. When the growth temperature or injected NH_3 flow rate is modulated, the morphologies changes accordingly. The spatial strain distribution, defects generated and optical properties were analyzed by Raman spectrum, PL and HRXRD, respectively. Based on the results, the strain was mostly dependent on the morphology, the optical properties were determined by the temperature and NH_3 flow rate, and the defects generated were mostly determined by the temperature.

5.3 Semi-polar microwalls

5.3.1 Introduction

Semi-polar InGaN/GaN quantum wells have better properties, which make them

attractive alternatives to the commonly used polar QWs in LEDs. First, the intrinsic electric field across the QWs caused by the spontaneous and piezoelectric polarizations is greatly reduced [143]. The field reduction is expected to increase the spatial overlap of electrons and holes, and thus decrease the detrimental impact of the non-radiative and Auger recombination. Secondly, they have a good In uptake for the quantum wells due to its lower chemical potential than polar or nonpolar surface, which makes the high performance green or green-yellow LEDs possible [144]. However, the current challenge for widely adopting the semi-polar and non-polar LEDs is the small size and high price of semi-polar GaN substrates which are typically 10*10 mm^2 in size and not easily accessible[145]. In order to develop a cost effective approach for achieving semi-polar GaN LED devices, the SAG method was applied to grow the semi-polar facet LEDs [143, 146, 147].

In order to study how the quantum wells grown on semi-polar facets affect the performance of InGaN/GaN-based LEDs, a full-structure microwall LED wafer is grown and both structural and optical properties are characterized in this work.

5.3.2 Experiments

Based on the growth method for GaN microwall templates prepared in last part, the microwall LEDs are grown. The strip is featured along <11-20> direction, for which only triangular structures can be formed [121]. After the GaN triangle strips were formed, the following procedure for the growth was the same as that used in planar structures except that the process started from the MQWs, as mentioned in Chapter 3. The contacts for the as-grown epi-wafers were formed through putting indium ball on top. The structural property was captured by the SEM, and the EL spectrum was captured through the ocean-optics spectrometer, which was attached with an integrating sphere.

5.3.3 Results and discussions

Figure 5.11 shows the surface morphology of as-grown full microwall LED devices, from which we can see the surface is very smooth. The triangular surface indicates the exposed facet is totally semi-polar. For all the triangular structures, they are connected at the bottom, implying good integration of all the microwalls.

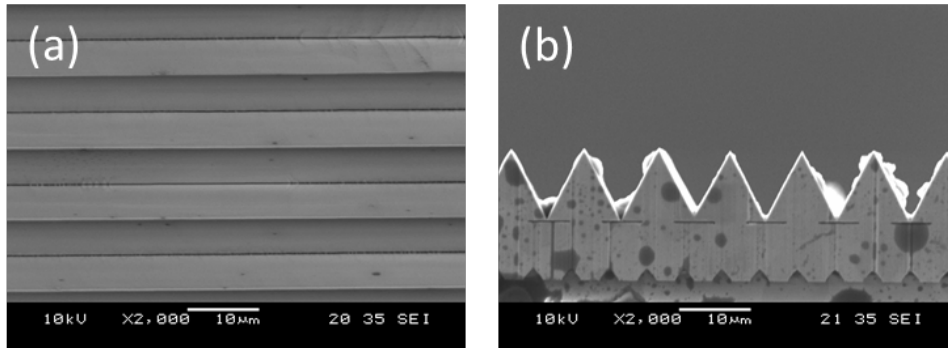

Figure 5.11 SEM morphologies for the grown semi-polar microwall structures, from (a) the top view and (b) the cross section view.

Figure 5.12 shows EL measured in the integrating sphere, with the inset showing the lighted area at different positions. The measured EL shows that the FWHM is 95 nm, which is very broad and includes many different colors. The emission color at different positions can be directly seen from the light due to the randomness of the indium contact. Since the growth of the quantum wells are the same with that of the normal growth process, the wavelength is red shifted which means that the In intake is increased due to the semi-polar property [144].

In order to study the EQE behavior and color emitting property, we will fabricate the epi-wafers to devices in the future to get more understanding about this kind of LEDs.

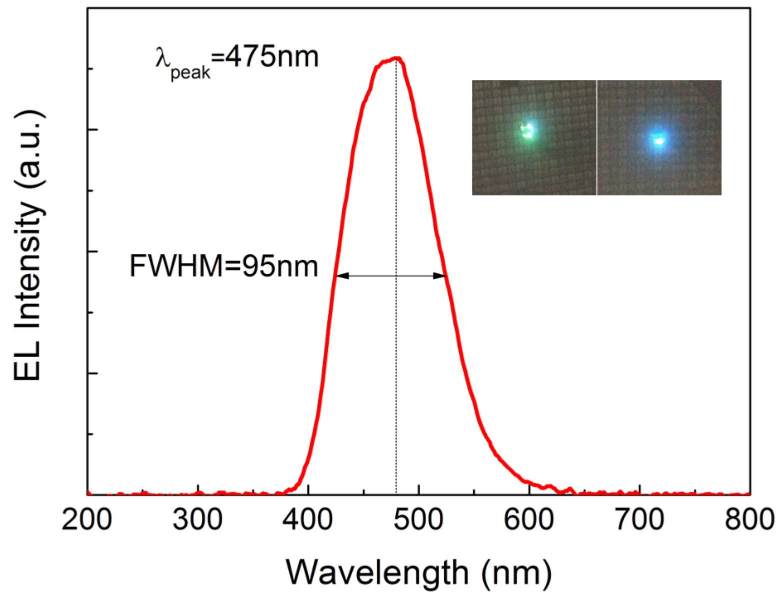

Figure 5.12 Electroluminescence of as-grown microwall LED, with inset showing the lighted up appearance at two different positions.

5.3.4 Conclusions

In conclusion, the full-structure microwall LEDs have been prepared. The surface morphology was captured by SEM, while the optical property was analyzed through the electroluminescence. The measured EL indicates more indium intake happens in the samples.

5.4 Summary

In summary, we have reviewed the problems arose during the fabrication of c-plane InGaN/GaN-based LEDs, and SAG method is proposed to realize the semi-polar and non-polar LED growth. Then, some preliminary work for the microwall structures is introduced, from which we achieved different morphologies through modulating the growth temperature and NH_3 flow rate. At last, an as-grown microwall wafer is characterized, which is a good basis for future studies.

Chapter 6

Conclusions and Future plan

6.1. Conclusions

In this thesis, InGaN/GaN-based LEDs have been studied from growth design to fabrication process and from planar structure to microwall structure. In order to improve the performance of the LEDs, we have designed different structures of epi-wafers. Besides, the fabrication process is optimized to enhance the performance of LED chips. Novel structure LEDs are also designed and optimized to further improve their properties. The major contribution of my work can be summarized as follows:

For the design of the epi-wafers, we have theoretically demonstrated the super performance of the tandem LEDs, when compared with the conventional LEDs. Both of the efficiency droop and the electrical performance are enhanced and the underneath physics is more uniform carrier distribution and relatively decreased forward voltage. Besides the tandem LEDs, the Mg-doped LEDs are also grown, which present decreased forward voltage and improved thermal electrical stability. The improved electrical performance is due to the decreased depletion length and relatively increased acceptor concentration.

During the fabrication process, the performance of the LED chips is improved due to the optimization of the reflective mirror through two methods. In the first method, we use the decoupled way to realize the high performance mirror, in which the ohmic contact is realized by the thin annealed Ni/Ag layer and high reflectivity is realized by pure silver deposition. Another method to realize reflective ohmic contact is by designing the thickness of $InGa_xN_yO_z$ interfacial layer. The optimized design allows the formation of a full $InGa_xN_yO_z$ layer that interfaces directly with the p-GaN and pure silver, which helps preserve the high-reflectivity of the pure silver and realize high-performance ohmic contact.

For the novel structures, microwall structure LEDs are designed and grown. Some preliminary work for the GaN microwall growth was presented, in which different

morphologies were achieved through modulating the growth parameters, such as temperature and NH_3 flow rate. Besides, an as-grown microwall LED device has been grown successfully, followed by a series of characterization process, which is a good basis for future studies.

6.2. Future plan

Although a systematic work has been studied to improve the performance of LEDs during the last few years, there are still more work need to be done in the future.

Since the heavily p-doped GaN is very difficult to realize due to high activation energy, high performance tandem LEDs as demonstrated in the theoretical research are not easy to achieve. Therefore, it is very important to find a replacement for the Mg dopant, which has low activation energy and helps achieve high p-doping level.

For the polar InGaN/GaN-based LEDs, polarization charges are generated at the interfaces between different layers. If the growth direction can be converted from the Ga-polar to N-polar, the polarization charges will have opposite symbol and the polarized electric field is changed over the quantum wells. If we can convert the Ga-polar to N-polar from the electron-blocking layer (EBL), the material quality of MQWs will not be degraded and the electric field generated in the MQWs will be counteracted by the charges induced by the polarization inverted EBL, which will in turn result in improved performance.

During the fabrication process for the top-up structure LEDs, if we can replace the conventional Ni/Au transparent conductive layer with a single graphene layer and realize ohmic contact at the same time, the transmission can be greatly enhanced, which results in superior LED performance.

During the fabrication process, the mesa etching is a necessary process, which exposes n-GaN for electrode deposition. However, a slanted sidewall existed after the etching

process. If we can optimize the angle through the simulation and realize it through etching, the performance of LED can also be improved.

Before discussion about how the microwall LEDs are grown, microwall LEDs can be fabricated through top-down method, in which parameters such as slanted angle of sidewalls and period can be designed to optimize their performance. Besides, nano-particles can be coated on top of the sidewalls with dielectric material as spacer to realize the surface plasmon effect and thus enhance the output power.

Microwall InGaN/GaN-based LEDs realized by MOCVD growth are novel and can contribute a lot to LED performance. However, the research in this field is very limited. In the future, study can be focused on the following three aspects, including the efficiency droop property, current spreading effect and white-light generation.

Appendix A

Epitaxial growth, material characterization and numerical simulation for InGaN/GaN-based light-emitting diodes

In this chapter, the components of metal-organic chemical vapor deposition (MOCVD) system and epitaxial growth mechanism of III-nitride materials are described. In addition, different characterization techniques are introduced. Besides, the simulation methodology, advanced physical models of semiconductor devices (APSYS) [46], is introduced, which is used to study the underlying physics of LED devices with different structures.

A.1 Metal-organic chemical vapor deposition (MOCVD)

During the last two decades, MOCVD has gradually become a commercially epitaxial growth method to grow III-nitride materials due to low cost, simple operation and suitability for mass production [148].

Figure A.1 shows the appearance of AIXTRON CCS MOCVD system in our research group. In this section, we firstly introduce the reaction precursors used in the growth process. The functions and properties of each precursor or carrier gas are described. Then, the gas diagram is shown and how the gas handling system can precisely control the reaction gases is explained, followed by the description of the close-coupled showerhead (CCS) chamber. At last, the growth mechanism and reaction process for the system are presented, followed by the introduction of in-situ process monitor by the interferometer.

Figure. A1 Appearance of 3×2″ AIXTRON CCS MOCVD system in our group.

A.1.1 Reaction precursors

Before we introduce how the epitaxial growth process happens, we first briefly describe the precursors and gases, which provide reaction sources and transport channels for the formation of III-nitride semiconductors. According to their properties, they are classified into the following types, group III precursors, group V precursors, doping precursors and carrier gases.

A.1.1.1 Group III precursors

Group III precursors are used to provide metal elements required in the growth process. There are mainly two types of precursors, the trimethyl (TM)($3CH_3$) and triethyl (TE) ($3CH_3CH_3$) alkyls series which are combined with metallic atoms (Ga, Al, In) [149]. The TM sources are frequently used because of their higher vapor pressure and greater stability [150]. The TE sources are normally used at lower pressure since they pyrolyze without producing CH_3 radicals and thus decrease the carbon incorporation in the epitaxial layers [151]. For all the functions of each precursor, TMGa is used for GaN/AlGaN material

growth, TEGa is used for InGaN/GaN quantum well growth, TMIn is used for indium incorporation of InGaN quantum well and TMAl is used for AlGaN growth.

A.1.1.2 Group V precursor

NH_3 is the group V precursor, which provides nitrogen source for III-nitride material growth [152]. Due to the high volatility of nitrogen during GaN growth, it is rather difficult to produce the required high quality films with a low N-vacancy level, which could lead to a high residual n dopant concentration in the as-grown intrinsic GaN materials [132]. A high partial pressure of NH_3 during the growth is always required to reduce the N vacancy concentration in 2D growth.

A.1.1.3 Doping precursors

Silane provides silicon for n-doping, while Cp_2Mg provides Mg for p-doping [153]. At room temperature, silane is a pyrophoric gas and must be handled very carefully to avoid spontaneous combustion in air [154]. Cp_2Mg provides Mg dopant for p-type III-nitride growth, but the Mg activation energy is very high as mentioned previously. The other problem for the p-doping is the memory effect, which is probably due to adsorption of these precursors (Cp2Mg) on the wall or quartz parts of the reactor [155]. This makes the abrupt changes of doping profile very difficult and special attention should be paid for run-to-run reproducibility after the p-doping process.

A.1.1.4 Carrier gases

H_2 is used as carrier gas for most of the growth process. In some special cases, N_2 is also used as carrier gas, such as in the growth of InGaN/GaN-based quantum wells, since H_2 carrier gas hinders the incorporation of indium [156].

A.1.2 Gas diagram and handling system

Figure A.3 shows the gas diagram for the MOCVD system, which describes how the

precursors run in the gas lines. In the diagram, A is N_2 purifier, B is H_2 purifier, C is NH_3 purifier, D is Hygrometer, E is the Hydride source channel, F is the MO source channel, G is the MO bubbler, H is the Gas supply for hydride sources, I is the Gas supply for run lines, J is the Hydride run line, K is the Hydride vent line, L is the Gas supply for auxiliary gas pipes, M is the Purging gas line- reactor sight glass, N is the MO1 run line, O is the MO1 vent line, P is the MO run bypass, Q is the MO2 run liner, R is the MO2 vent line, S is the Gas supply for venting, T is the Gas supply for MO2 sources, U is the Gas supply for MO1 sources and V is the MO vacuum (for changing the MO bubbler).

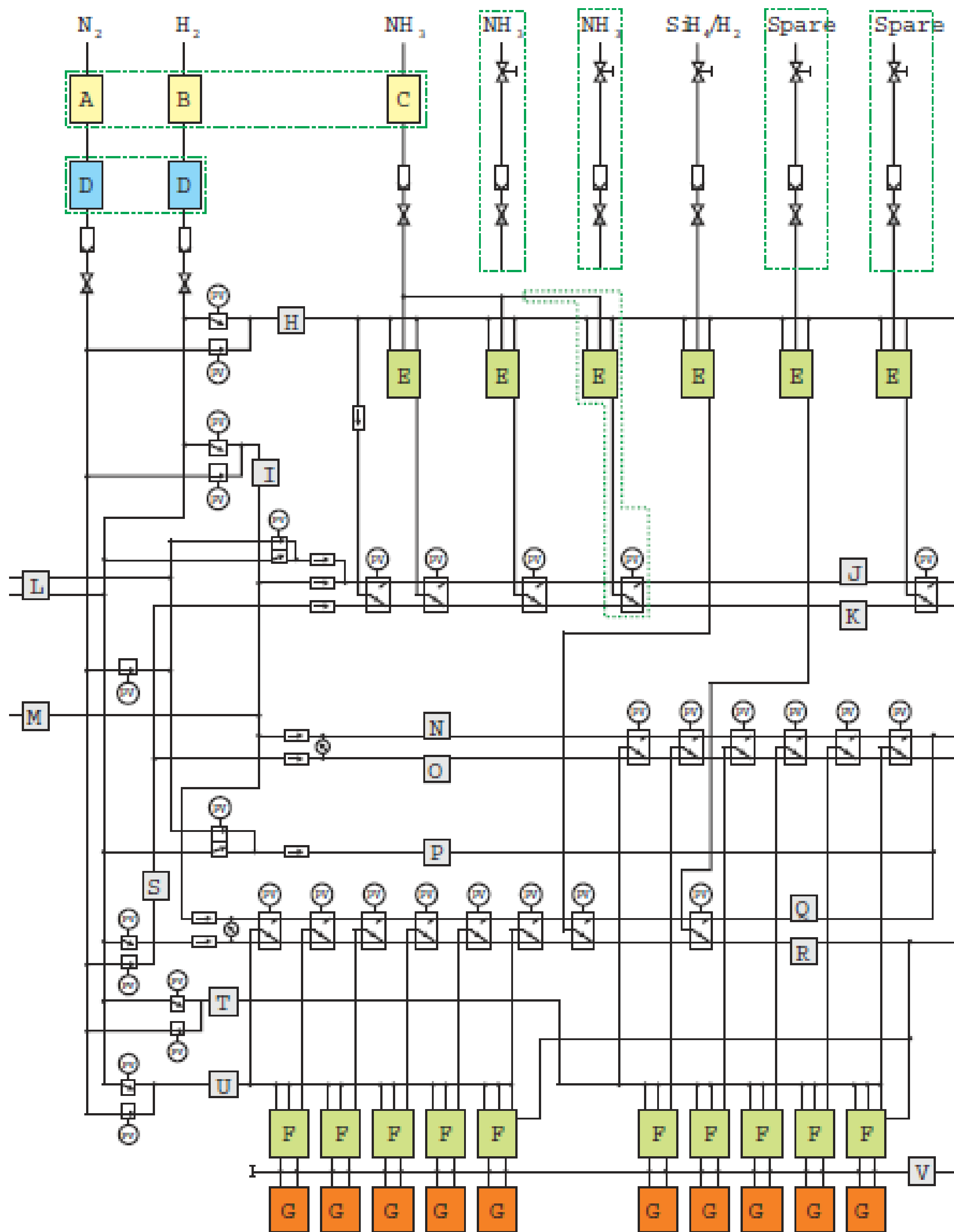

Figure. A2 Gas diagram for III-nitride material growth. [157]

Besides the gas diagram, the gas handling system is introduced with the purpose of delivering the reactant into the growth chamber precisely without transients due to the change of the pressure or gas flows.

For gas phase source, the mass flow controller (MFC) can be used to control the molar mass flow rates precisely. For solid or liquid phase sources, such as MO precursors, the exact amount of materials is controlled by the MFC, as well as the pressure and temperature controller. The carrier gas flows into the bubbler to transport MO precursor vapors and the MO push gas dilutes the mixture of carrier gas and MO precursor to prevent the precipitating and contaminating from the gas line. More H_2 or N_2 will flow through the MO run line to further dilute the MO precursors and take the mixture into the reactor. As shown in Figure A3, a general method of calculating the MO source flow in the system is given.

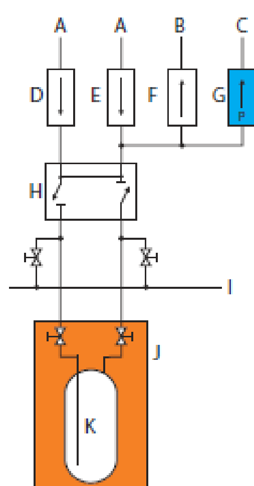

Figure. A3 Gas lines for an MO source with double dilution. [157]

A is the carrier gas supply, B is the run/vent line, C is the pressure controller, D is the source input MFC with the flow rate of F_{source}, E is the dilution MFC with the flow rate of F_{dilute}, F is the inject MFC with the flow rate of F_{inject}, G is the pressure controller, H is a 4/2 pneumatic valve, I is the MO vacuum, J is the thermal heat bath to hold the MO bubblers and K is the MO bubbler.

$$F = F_{inject} \times \frac{F_{source}}{F_{source} + F_{dilute}} \quad \text{(A.1)}$$

Here, F is the effective flow rate of the precursors which can be precisely tuned for the

reaction process through the combination of F_{source}, F_{dilute} and F_{inject}.

A.1.3 Chamber design

The close-coupled showerhead (CCS) MOCVD system from Aixtron Company was used to grow III-nitride materials for our research. For CCS technology [158], the chamber is vertically designed, the main body is made of stainless steel and the main gas flow is injected into the reactor over the entire substrate surface via the small holes in the showerhead, as shown in Figure A4 (a). The distance between the showerhead and the substrate is very small, and the process gas is introduced into the reactor through many small holes, in which way a more uniform process gas distribution over the substrates can be achieved. During the injection process, reactants are separated by many small tubes, as shown in Figures A4 (a) and (b). The substrates lie on a rotating susceptor heated by a resistance heater, as shown in Figure A4 (c). Separate heating zones enable the temperature profile to be adjusted in such a manner that the susceptor always has the same temperature over its entire surface as shown in Figure A5.

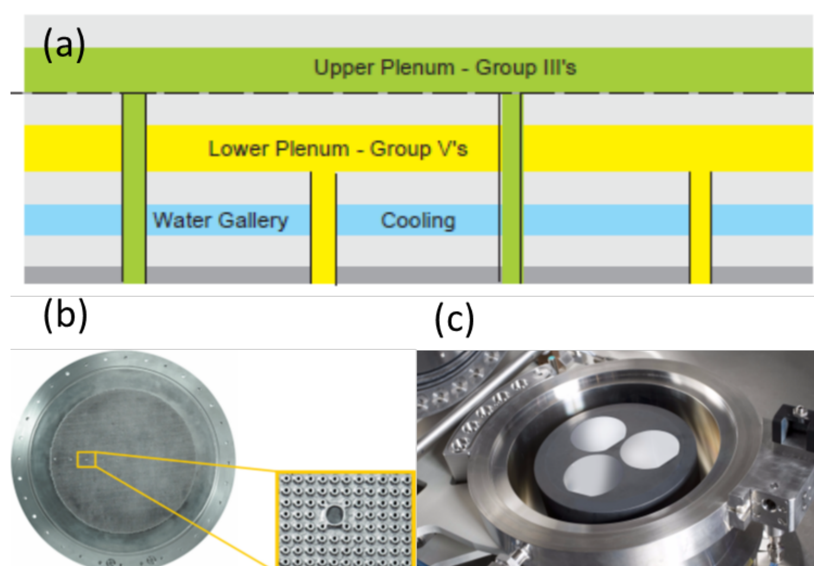

Figure. A4 (a) The cross section and (b) the detailed view for the showerhead, (c) the holder for substrates. [157]

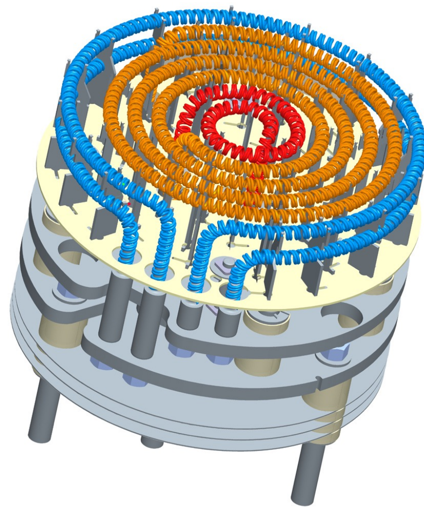

Figure. A5 Tungsten filament for substrate heating, with three colors denoting three heating zones. [157]

A.1.4 Growth mechanism and reaction process

The schematic diagram in Figure A6 shows the fundamental reaction mechanism for III-nitride materials grown through the MOCVD system [159].

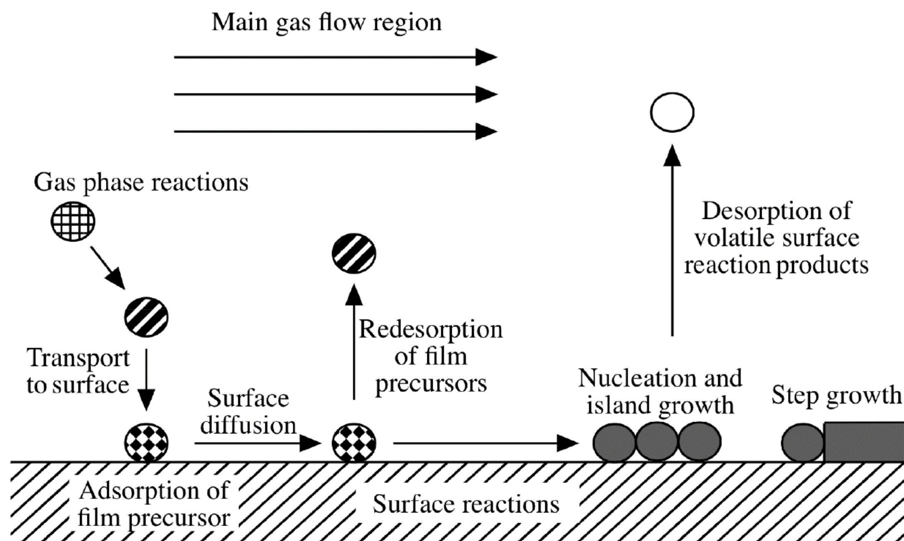

Figure. A6 General reaction process in MOCVD. [159]

During a growth process, the main gas flow, which is composed of reaction gas and carrier gas, is injected into the chamber, and transported to the surface of the heated and rotated substrate. Gas molecules will break up and release desired atoms, which will react and form nucleation islands, accompanied with pyrolysis process, as well as physical processes. Then the formed islands will gradually expand, merge to each other and form planar structures.

The basic MOCVD reaction describing the GaN deposition process can be described by the following reaction [160]:

Ga(CH3)3(v) + NH3(v) -->GaN(s) + 3CH4(v), where (v)=vapor and (s)=solid (A.2)

Conventional GaN growth in MOCVD usually occurs over a wide temperature range (600°C–1100°C), during which the growth is limited by mass transport of the group III reactant to the growing interface. Because the diffusion process is slightly temperature dependent, there exists a slight increase in the growth rate when the growth temperature increases. Growth optimization is typically done by empirical studies of external parameters such as growth temperature, V/III ratio, substrate tilt and mass flow rates.

During this process, there are also some precursors or reaction products being desorbed back into the gas flow, which will be pumped out through filter and scrubber system.

A.1.5 In-situ reflectance monitor

The Interferometer as shown in Figure A7 uses Fabry-Perot interferometry to monitor and analyze the MOCVD growth of thin-film materials [161]. For the blue emitting material, GaN, the film extinction coefficient is low ($k < 0.01$) for the red probe wavelength (635nm) used in the AIXTRON Ltd. interferometer. Therefore, attenuation of the probe intensity due to absorption is negligible and any significant changes in the reflected intensity from that

predicted by theory is likely to be due to factors other than absorbance. This gives us an advantage in the interpretation of GaN growth as the growth of this material, typically, proceeds in a very unusual manner. As shown in Figure A8, a and b correspond to the deposition and annealing of the nucleation layer, respectively. In a, the nucleation layer is initially a continuous and smooth film, and in b, this image shows that the reduction in reflectivity is due to the formation of a number of discrete islands with the sapphire substrate exposed between them. c, d, e, and f correspond to the deposition of the high temperature buffer layer to a thickness of 70, 200, 450 and 1700 nm, respectively. The transition from three-dimensional to pseudo-two dimensional growth can be clearly seen. As the islands coalesce, and the roughness reduces, the reflectivity is seen to increase. The surface morphologies of samples grown on sapphire substrate at different stages can be observed using AFM as shown in Figure A9.

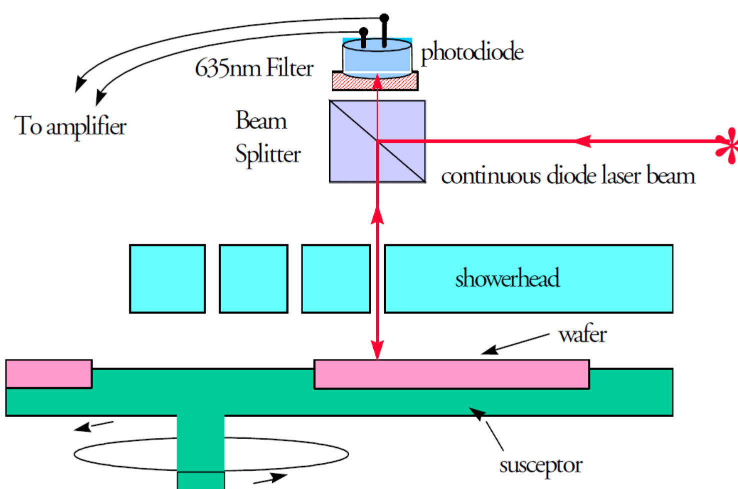

Figure. A7 Schematic diagram for the setup of interferometer.

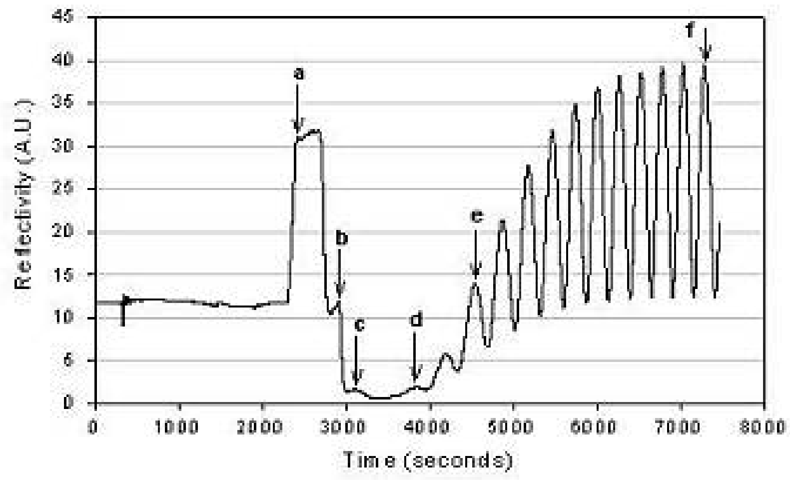

Figure. A8 Variation of reflectivity with time for the deposition of GaN on sapphire.[161]

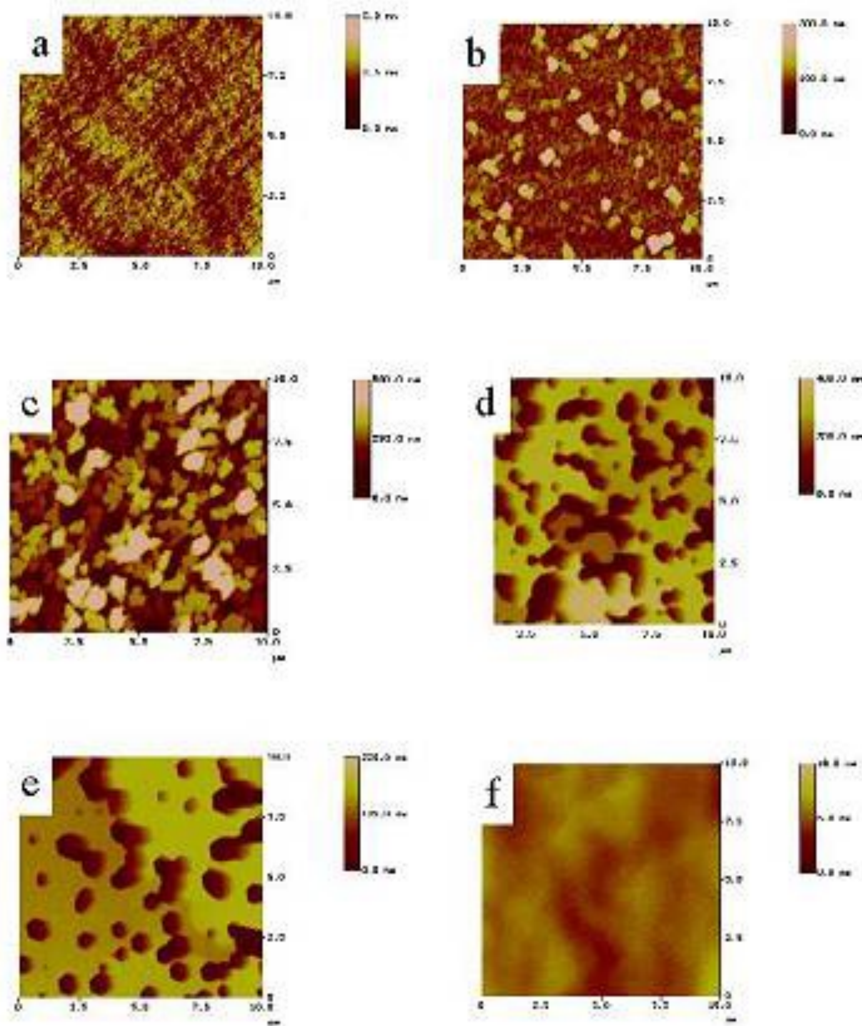

Figure. A9 AFM images of GaN film at different growth stages. [161]

A.2 Material characterization techniques

A.2.1 Scanning electron microscopy (SEM)

SEM is one of the mostly used microscopes, which generates images by scanning the electron beams on the sample and measuring the signals that contain information about the surface morphologies by the detector [162]. For my thesis work, the SEM was used to study the morphology of both the annealed mirror surface and the as-grown GaN epi-wafers, which was important for us to understand the underneath mechanism for the improved mirror

performance and different as-grown GaN morphologies.

A.2.2 Atomic force microscopy (AFM)

AFM is used to characterize local properties of material surfaces. The surface morphologies are achieved through measuring the reflecting laser by moving a tip across the samples [163], which is realized through three imaging modes, which are contact mode, tapping mode and non-contact mode. For my work, the tapping mode was used to capture the surface roughness of the as-grown epi-wafers and mirror contacts.

A.2.3 High-resolution x-ray diffraction (HRXRD)

HRXRD rocking curve is used to characterize the structural properties of semiconductors, including stress, dislocations and defects. The mechanism for the XRD measurement is based on Bragg's law, which means the diffracted emission peak happens at one specific angle where the constructive interference occurs. However, the defect generated in the semiconductor crystals can broaden the emission peaks, and its density can be calculated through measuring the FWHM of its x-ray rocking curves. Figure A10 (a) and (b) show typical x-ray rocking curves of GaN measured along symmetrical (002) and asymmetrical (102) reflection planes, respectively. This measurement was used to feature the material quality for as-grown epi-wafers grown by MOCVD system.

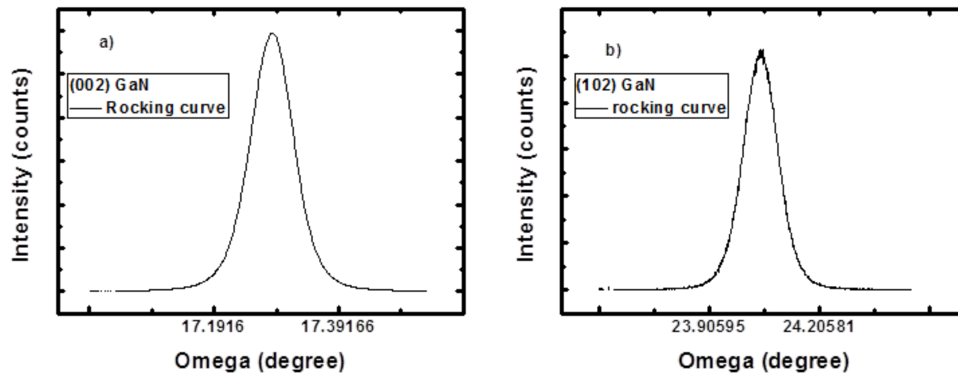

Figure. A10 Typical rocking curves of GaN measured along (a) (002) and (b) (102) reflection planes.

A.2.4 Photoluminescence (PL) spectroscopy

PL spectroscopy is used to characterize the optical properties of semiconductors. It is one kind of light emission from materials after absorption of photons. There are many mechanisms for PL emission in III-nitride materials, such as free exciton recombination, exciton bound to a neural donor or acceptor, one LO phonon replica and donor-acceptor pairs [164]. The peaks of the PL spectrum can be used to identify the emission mechanisms, while the intensity and the FWHM can be used to characterize their crystal qualities. In this thesis, PL spectroscopy was used to characterize the property of epi-wafers grown by MOCVD system.

A.2.5 Raman spectroscopy

Raman spectroscopy is widely used to measure the in-plane strain and stress of III-nitride semiconductors [131]. There are six active phonon modes existed and among them E_2 high and A_1(LO) [133] modes can be used to measure the strain states of the semiconductors. Usually, the blue shift of the phonon frequencies for the measured modes is attributed to the compressive strain, while the redshift is caused by the tensile strain [136]. For the A_1(LO)

mode, it is also affected by the free carriers' concentration and long-range electrostatic forces [132, 165, 166]. During my research, Raman spectroscopy was used to measure the in-plane stress of GaN microwall structures, which could be indicated from the position and offset of the Raman shift when compared with the strain-free samples.

A.2.6 Secondary ion mass spectroscopy (SIMS)

SIMS is used to measure the element depth profile along a definite direction. During a time of flight (ToF) SIMS measurement process, the specimen surface is sputtered by a focused primary ion beam, and the mass/charge ratio of these ejected secondary ions is measured by a mass spectrometer, which determines the elemental, isotopic or molecular composition of the surface to a depth of 1-2 nm [167, 168]. SIMS is the most sensitive surface analysis technique with elemental detection limits ranging from parts per million to parts per billion. During my work, SIMS was applied to measure the element depth profile for mirrors both before and after annealing, which sheds light on the mechanism of better performance in the proposed structures.

A.2.7 X-ray photoelectron spectroscopy (XPS)

XPS characterization is used to investigate the chemical composition on the sample surface [169]. During the XPS achieving process, the sample is irradiated by a beam of X-rays and photoelectrons with different kinetic energies generated in the process are ejected out and measured simultaneously [170, 171]. The peaks and energy intensities appeared in the spectrum enable the identification and quantification of all the surface elements, except that hydrogen and helium are not easily detectable by using laboratory-scale x-rays. During my PhD work, XPS was applied to check the elemental surface states of the p-GaN after ITO annealing and measured results provided me evidence to explain the optimized performance of mirror in the proposed sample.

A.3 Numerical simulation technique

A.3.1 Advanced physical models of semiconductor devices (APSYS)

In addition to the experimental characterization techniques mentioned above, simulation was also applied to study the optical and electrical performance of InGaN/GaN-based LEDs, which was realized through a 2D/3D modelling method by APSYS software. Based on many advanced physical models, including drift-diffusion model, spontaneous emission spectrum, heat flux equation and ray-tracing methods, the simulated results are calculated through finite element analysis [172, 173]. Many important results, such as optical power, carrier distribution and band diagrams at different current levels can be achieved from the simulation, which will not only be very helpful for us to understand the underlying physics of peculiar LED performances, but also provide us guideline about how to improve the performance of LED devices.

List of Publications

1 **Binbin Zhu**, Swee Tiam Tan, Shunpeng Lu, Yiping Zhang, Weigao Xu, Namig Hasanov, Qihua Xiong, Hilmi Volkan Demir, "Structural and Optical Properties for GaN Microwalls", **in preparation.**

2 **Binbin Zhu**, Zi-Hui Zhang, Swee Tiam Tan, Shunpeng Lu, Yiping Zhang, Xuejun Kang, Ning Wang, Namig Hasanov, and Hilmi Volkan Demir, "Effect of Mg doping in the barriers on the electrical performance of InGaN/GaN-based light-emitting diodes", IEEE Photonics Journal, **under review**.

3 **Binbin Zhu**, Swee Tiam Tan, Wei Liu, Shunpeng Lu, Yiping Zhang, Shi Chen, Namig Hasanov, Xuejun Kang, and Hilmi Volkan Demir, "Modulating ohmic contact through $InGa_xN_yO_z$ interfacial layer for high-performance InGaN/GaN-based light-emitting diodes", IEEE Photonics Journal, vol. 8, pp. 1-8, 2016.

4 **Binbin Zhu**, Wei Liu, Shunpeng Lu, Yiping Zhang, Namig Hasanov, Xueliang Zhang, Yun Ji, Zi-Hui Zhang, Swee Tiam Tan, Hongfei Liu, and Hilmi Volkan Demir, "Decoupling contact and mirror: an effective way to improve the reflector for flip-chip InGaN/GaN-based light-emitting diodes", Journal of Physics D: Applied Physics, vol. 49, p. 265106, 2016.

5 Ke Zheng, Junliang Zhao, Zi-Hui Zhang, Yun Ji, **Binbin Zhu**, Tan Swee Tiam, Hilmi Volkan Demir, Teo Kie Leong, Xiao Wei Sun, "An optically readable InGaN/GaN RRAM", Electron Devices, IEEE Transactions on, 2016.

6 Xin Zhao, Weizhen Liu, Rui Chen, Yuan Gao, **Binbin Zhu**, Hilmi Volkan Demir, Shijie Wang, Handong Sun, "Exciton energy recycling from ZnO defect levels: towards electrically driven hybrid quantum-dot white light-emitting-diodes,"

Nanoscale, 2016.

7 Hasanov, N., **B. Zhu**, V.K. Sharma, S. Lu, Y. Zhang, W. Liu, S.T. Tan, X.W. Sun, and H.V. Demir, "Improved performance of InGaN/GaN flip-chip light-emitting diodes through the use of robust Ni/Ag/TiW mirror contacts," Journal of Vacuum Science & Technology B, 2016. **34**(1): p. 011209.

8 Zhang, Y.P., Z.-H. Zhang, W. Liu, S.T. Tan, Z.G. Ju, X.L. Zhang, Y. Ji, L.C. Wang, Z. Kyaw, and N. Hasanov, **B. Zhu**, S. Lu, X. W. Sun, and H. V. Demir, "Nonradiative recombination—critical in choosing quantum well number for InGaN/GaN light-emitting diodes," Optics Express, 2015. **23**(3): p. A34-A42.

9 Zhang, Z.-H., W. Liu, S.T. Tan, Z. Ju, Y. Ji, Z. Kyaw, X. Zhang, N. Hasanov, **B. Zhu**, and S. Lu, Y.P. Zhang, X. W. Sun, and H. V. Demir, "On the mechanisms of InGaN electron cooler in InGaN/GaN light-emitting diodes," Optics Express, 2014. **22**(103): p. A779-A789.

10 Zhang, Z.-H., W. Liu, S.T. Tan, Y. Ji, L. Wang, **B. Zhu**, Y. Zhang, S. Lu, X. Zhang, and N. Hasanov, X.W. Sun, and H.V. Demir, "A hole accelerator for InGaN/GaN light-emitting diodes," Applied Physics Letters, 2014. **105**(15): p. 153503.

11 Zhang, Z.-H., Y. Ji, W. Liu, S.T. Tan, Z. Kyaw, Z. Ju, X. Zhang, N. Hasanov, S. Lu, and Y. Zhang, **B. Zhu**, X.W. Sun, and H.V. Demir, "On the origin of the electron blocking effect by an n-type AlGaN electron blocking layer," Applied Physics Letters, 2014. **104**(7): p. 073511.

12 Lu, S., W. Liu, Z.-H. Zhang, S.T. Tan, Z. Ju, Y. Ji, X. Zhang, Y. Zhang, **B. Zhu**, and Z. Kyaw, N. Hasanov, X. W. Sun, and H. V. Demir, "Low thermal-mass LEDs: size effect and limits," Optics Express, 2014. **22**(26): p. 32200-32207.

13 Kyaw, Z., Z.-H. Zhang, W. Liu, S.T. Tan, Z.G. Ju, X.L. Zhang, Y. Ji, N. Hasanov, **B.**

Zhu, and S. Lu, Y.P. Zhang, X. W. Sun, and H. V. Demir, " On the effect of N-GaN/P-GaN/N-GaN/P-GaN/N-GaN built-in junctions in the n-GaN layer for InGaN/GaN light-emitting diodes," Optics Express, 2014. **22**(1): p. 809-816.

14 Kyaw, Z., Z.-H. Zhang, W. Liu, S.T. Tan, Z.G. Ju, X.L. Zhang, Y. Ji, N. Hasanov, **B. Zhu**, and S. Lu, Y.P. Zhang, J. H. Teng, X. W. Sun, and H. V. Demir, "Simultaneous enhancement of electron overflow reduction and hole injection promotion by tailoring the last quantum barrier in InGaN/GaN light-emitting diodes," Applied Physics Letters, 2014. **104**(16): p. 161113.

15 Ju, Z.G., W. Liu, Z.-H. Zhang, S.T. Tan, Y. Ji, Z. Kyaw, X.L. Zhang, S.P. Lu, Y.P. Zhang, and **B.B. Zhu**, N. Hasanov, X. W. Sun, and H. V. Demir, "Advantages of the Blue InGaN/GaN Light-Emitting Diodes with an AlGaN/GaN/AlGaN Quantum Well Structured Electron Blocking Layer," ACS Photonics, 2014. **1**(4): p. 377-381.

16 Ju, Z., W. Liu, Z.-H. Zhang, S.T. Tan, Y. Ji, Z. Kyaw, X. Zhang, S. Lu, Y. Zhang, and **B. Zhu**, N. Hasanov, X. W. Sun, and H. V. Demir, "Improved hole distribution in InGaN/GaN light-emitting diodes with graded thickness quantum barriers," Applied Physics Letters, 2013. **102**(24): p. 243504.

Conference

1 Xin Zhao, Weizhen Liu, Rui Chen, Yuan Gao, **Binbin Zhu**, Hilmi Volkan Demir, Shijie Wang, Handong Sun*, "Realization of Quantum-Dot Hybrid White Light-emitting-diodes via FRET from ZnO Nanowires Surface Defects", at the IPS Meeting , Singapore, 7th -8th Mar, 2016.

2 **Zhu, B.**, W. Liu, Z.-H. Zhang, S.T. Tan, X.W. Sun, and H.V. Demir. "Tandem InGaN/GaN light-emitting diodes." at the IEEE Photonics Conference (IPC), Hyatt Regency Reston, Reston, Virginia USA, 4th – 8th Oct, 2015.

Patent

1. LIU Wei, Zabu KYAW, ZHANG Zi-Hui, **ZHU Binbin**, JU Zhengang, TAN Swee Tiam, ZHANG Xueliang, Hilmi Volkan DEMIR, "LIGHT-EMITTING DEVICE AND METHOD OF FORMING THE SAME", International application No. PCT/SG2015/05010

Bibliography

1. Johnson, W.C., J. Parson, and M. Crew, Nitrogen compounds of gallium. iii. The Journal of Physical Chemistry, 1932. **36**(10): p. 2651-2654.
2. Maruska, H.P. and J. Tietjen, The preparation and properties of Vapor-Deposited single-crystal-line GaN. Applied Physics Letters, 1969. **15**(10): p. 327-329.
3. Van de Walle, C.G., C. Stampfl, and J. Neugebauer, Theory of doping and defects in III–V nitrides. Journal of crystal growth, 1998. **189**: p. 505-510.
4. Toth, M., K. Fleischer, and M. Phillips, Direct experimental evidence for the role of oxygen in the luminescent properties of GaN. Physical Review B, 1999. **59**(3): p. 1575.
5. Maruska, H., D. Stevenson, and J. Pankove, Violet luminescence of Mg-doped GaN. Applied Physics Letters, 1973. **22**(6): p. 303-305.
6. Ilegems, M. and R. Dingle, Luminescence of Be-and Mg-doped GaN. Journal of Applied Physics, 1973. **44**(9): p. 4234-4235.
7. Maruska, H., W. Rhines, and D. Stevenson, Preparation of Mg-doped GaN diodes exhibiting violet electroluminescence. Materials Research Bulletin, 1972. **7**(8): p. 777-781.
8. Amano, H., et al., Metalorganic vapor phase epitaxial growth of a high quality GaN film using an AlN buffer layer. Applied Physics Letters, 1986. **48**(5): p. 353-355.
9. Nakamura, S., T. Mukai, and M. Senoh, Insitu monitoring and Hall measurements of GaN grown with GaN buffer layers. Journal of applied physics, 1992. **71**(11): p. 5543-5549.
10. Nakamura, S. and M.R. Krames, History of Gallium–Nitride-Based Light-Emitting Diodes for Illumination. 2013.
11. Amano, H., et al., P-type conduction in Mg-doped GaN treated with low-energy electron beam irradiation (LEEBI). Japanese Journal of Applied Physics, 1989. **28**(12A): p. L2112.
12. Nakamura, S., et al., Thermal annealing effects on p-type Mg-doped GaN films. Japanese Journal of Applied Physics, 1992. **31**(2B): p. L139.

13. Nakamura, S., M. Senoh, and T. Mukai, P-GaN/N-InGaN/N-GaN double-heterostructure blue-light-emitting diodes. Japanese Journal of Applied Physics, 1993. **32**(1A): p. L8.
14. Nakamura, S., et al., High-brightness InGaN blue, green and yellow light-emitting diodes with quantum well structures. Japanese Journal of Applied Physics, 1995. **34**(7A): p. L797.
15. Morkoç, H., Handbook of Nitride Semiconductors and Devices, Materials Properties, Physics and Growth. Vol. 1. 2009: John Wiley & Sons.
16. Morkoç, H., Handbook of nitride semiconductors and devices, vol. 1. ISBN-13, 2008: p. 978-3527408399.
17. Dikme, Y., MOVPE and Characterization
of GaN-based Structures on
Alternative Substrates.
18. Liu, L. and J.H. Edgar, Substrates for gallium nitride epitaxy. Materials science & engineering. R, Reports, 2002. **37**(3): p. 61-127.
19. Ambacher, O., Growth and applications of group III-nitrides. Journal of Physics D: Applied Physics, 1998. **31**(20): p. 2653.
20. https://en.wikipedia.org/wiki/Indium_nitride.
21. h t t p : / / w w w . i o ffe . r u / S V A / N S M / S e m i c o n d /.
22. Strite, S., M. Lin, and H. Morkoc, Progress and prospects for GaN and the III–V nitride semiconductors. Thin Solid Films, 1993. **231**(1-2): p. 197-210.
23. Strite, S. and H. Morkoç, GaN, AlN, and InN: a review. Journal of Vacuum Science & Technology B, 1992. **10**(4): p. 1237-1266.
24. Davydov, V.Y., et al., Absorption and emission of hexagonal InN. Evidence of narrow fundamental band gap. physica status solidi (b), 2002. **229**(3): p. r1-r3.
25. University of Ulm, “Lecture Notes in Optoelectronics, Scholz F.,” http://www-opto.e-technik.uni-ulm.de/lehre/cs/.
26. Ambacher, O., et al., Two dimensional electron gases induced by spontaneous and piezoelectric polarization in undoped and doped AlGaN/GaN heterostructures. Journal of applied physics, 2000. **87**(1): p. 334-344.
27. HARMAND, M.J.-C., et al., MOVPE growth of III-nitride nanostructures: From self-assembled growth to selective area growth.

28. Takeuchi, T., H. Amano, and I. Akasaki, Theoretical study of orientation dependence of piezoelectric effects in wurtzite strained GaInN/GaN heterostructures and quantum wells. Japanese Journal of Applied Physics, 2000. **39**(2R): p. 413.
29. SCHUBERT, E.F., LIGHT-EMITTING DIODES. Cambridge University Press, 2006.
30. Zhao, H., et al., Growths of staggered InGaN quantum wells light-emitting diodes emitting at 520–525 nm employing graded growth-temperature profile. Applied Physics Letters, 2009. **95**(6): p. 061104.
31. Bernardini, F. and V. Fiorentini, Spontaneous vs. piezoelectric polarization in III-V nitrides: conceptual aspects and practical consequences. arXiv preprint cond-mat/9908087, 1999.
32. Neugebauer, J. and C.G. Van de Walle, Role of hydrogen in doping of GaN. Applied physics letters, 1996. **68**(13): p. 1829-1831.
33. Kozodoy, P., et al., Heavy doping effects in Mg-doped GaN. Journal of Applied Physics, 2000. **87**(4): p. 1832-1835.
34. http://www.durhambats.org.uk/leds.shtml.
35. Energy Savings Potential of Solid-State Lighting in General Illumination Applications. DOE report, 2012.
36. http://www.ledhorticulture.com/wp-content/uploads/2016/07/bf45938bf570e54212546a03f10a3296.jpg.
37. Song, J.O., J.-S. Ha, and T.-Y. Seong, Ohmic-contact technology for GaN-based light-emitting diodes: Role of p-type contact. Electron Devices, IEEE Transactions on, 2010. **57**(1): p. 42-59.
38. http://www.irepairhome.com/led-light-fixtures.htm.
39. Jang, H.W. and J.-L. Lee, Mechanism for ohmic contact formation of Ni/Ag contacts on p-type GaN. Applied physics letters, 2004. **85**(24): p. 5920-5922.
40. http://www.visionxusa.com/Automotive_Lights/t4/articles.html.
41. González-Hernández, R., et al., Theoretical study of Ni adsorption on the GaN (0001) surface. Applied Surface Science, 2010. **256**(22): p. 6495-6498.
42. http://www.displayblog.com/2009/09/22/samsung-un55b8500-55-inch-1080p-lcd-tv-with-led-backlight/.
43. http://www.lighting.philips.com/main/products/horticulture.html.
44. https://en.wikipedia.org/wiki/Li-Fi.

45. http://www.hqewled.com/news/detail_9211.html.
46. Zhang, Z.-H., et al., On the effect of step-doped quantum barriers in InGaN/GaN light emitting diodes. Journal of Display Technology, 2013. **9**(4): p. 226-233.
47. Shen, Y., et al., Auger recombination in InGaN measured by photoluminescence. Applied Physics Letters, 2007. **91**(14): p. 1101.
48. Kuo, Y.-K., J.-Y. Chang, and M.-C. Tsai, Enhancement in hole-injection efficiency of blue InGaN light-emitting diodes from reduced polarization by some specific designs for the electron blocking layer. Optics letters, 2010. **35**(19): p. 3285-3287.
49. Kim, M.-H., et al., Origin of efficiency droop in GaN-based light-emitting diodes. Applied Physics Letters, 2007. **91**: p. 183507.
50. Xie, J., et al., On the efficiency droop in InGaN multiple quantum well blue light emitting diodes and its reduction with p-doped quantum well barriers. Applied Physics Letters, 2008. **93**(12).
51. Liu, J., et al., Barrier effect on hole transport and carrier distribution in InGaN/GaN multiple quantum well visible light-emitting diodes. Applied Physics Letters, 2008. **93**(2): p. 1102.
52. Verzellesi, G., et al., Efficiency droop in InGaN/GaN blue light-emitting diodes: Physical mechanisms and remedies. Journal of Applied Physics, 2013. **114**(7): p. 071101-071101-14.
53. Cho, J., E.F. Schubert, and J.K. Kim, Efficiency droop in light-emitting diodes: Challenges and countermeasures. Laser & Photonics Reviews, 2012: p. 408-421.
54. https://en.wikipedia.org/wiki/Tunnel_diode.
55. Takeuchi, T., et al., GaN-based light emitting diodes with tunnel junctions. Japanese Journal of Applied Physics, 2001. **40**(8B): p. L861.
56. Krishnamoorthy, S., F. Akyol, and S. Rajan, InGaN/GaN Tunnel Junctions For Hole Injection in GaN Light Emitting Diodes. arXiv preprint arXiv:1403.3932, 2014.
57. Grandjean, N., J. Massies, and M. Leroux, Nitridation of sapphire. Effect on the optical properties of GaN epitaxial overlayers. Applied physics letters, 1996. **69**(14): p. 2071-2073.
58. Mo, C., et al., Growth and characterization of InGaN blue LED structure on Si(111) by MOCVD. Journal of Crystal Growth, 2005. **285**(3): p. 312-317.

59. Kim, K., et al., Effects of growth rate of a GaN buffer layer on the properties of GaN on a sapphire substrate. Journal of applied physics, 1999. **85**(12): p. 8441.
60. Heying, B., et al., Role of threading dislocation structure on the x-ray diffraction peak widths in epitaxial GaN films. Applied Physics Letters, 1996. **68**(5): p. 643-645.
61. Görgens, L., et al., Characterization of InGaN thin films using high-resolution x-ray diffraction. Applied physics letters, 2000. **76**(5): p. 577.
62. Öztürk, M., et al., Structural analysis of an InGaN/GaN based light emitting diode by X-ray diffraction. Journal of Materials Science: Materials in Electronics, 2010. **21**(2): p. 185-191.
63. Xu, J. and T. Wang, Efficiency droop improvement for InGaN-based light-emitting diodes with gradually increased In-composition across the active region. Physica E: Low-dimensional Systems and Nanostructures, 2013.
64. Cao, B., et al., Enhancing light output of GaN-based LEDs with graded-thickness barriers and wells. 2013.
65. Wang, C., et al., Hole transport improvement in InGaN/GaN light-emitting diodes by graded-composition multiple quantum barriers. Applied Physics Letters, 2011. **99**(17): p. 171106-171106-3.
66. Sheng Xia, C., et al., Droop improvement in blue InGaN/GaN multiple quantum well light-emitting diodes with indium graded last barrier. Applied Physics Letters, 2011. **99**(23): p. 233501-233501-3.
67. Wang, C., et al., Efficiency droop alleviation in InGaN/GaN light-emitting diodes by graded-thickness multiple quantum wells. Applied Physics Letters, 2010. **97**(18): p. 181101-181101-3.
68. Akyol, F., S. Krishnamoorthy, and S. Rajan, Tunneling-based carrier regeneration in cascaded GaN light emitting diodes to overcome efficiency droop. Applied Physics Letters, 2013. **103**(8): p. 081107.
69. Zhang, Z.-H., et al., A PN-type quantum barrier for InGaN/GaN light emitting diodes. Optics express, 2013. **21**(13): p. 15676-15685.
70. Vurgaftman, I. and J. Meyer, Band parameters for nitrogen-containing semiconductors. Journal of Applied Physics, 2003. **94**(6): p. 3675-3696.
71. Zhang, Z.-H., et al., InGaN/GaN light-emitting diode with a polarization tunnel junction. Applied Physics Letters, 2013. **102**(19): p. 193508-193508-5.

72. Tan, S.T., et al., Advances in the LED materials and architectures for energy-saving solid-state lighting toward "lighting revolution". Photonics Journal, IEEE, 2012. **4**(2): p. 613-619.
73. Feng, L., et al., Deep saturation of junction voltage at large forward current of light-emitting diodes. Journal of Applied Physics, 2007. **102**(9): p. 094511.
74. Zhang, Z.-H., et al., Improved InGaN/GaN light-emitting diodes with a p-GaN/n-GaN/p-GaN/n-GaN/p-GaN current-spreading layer. Optics express, 2013. **21**(4): p. 4958-4969.
75. Krames, M., et al., Status and Future of High-Power Light-Emitting Diodes for Solid-State Lighting. Journal of Display Technology, 2007. **3**(2): p. 160-175.
76. Li, Y., et al., Elucidating negative capacitance in light-emitting diodes using an advanced semiconductor device theory. Journal of Applied Physics, 2011. **109**(12): p. 124506.
77. Chen, N., et al., Capacitance–Voltage and Current–Voltage Measurements of Nitride Light-Emitting Diodes. Electron Devices, IEEE Transactions on, 2007. **54**(12): p. 3223-3228.
78. Ji, Y., et al., Enhanced hole transport in InGaN/GaN multiple quantum well light-emitting diodes with a p-type doped quantum barrier. Optics letters, 2013. **38**(2): p. 202-204.
79. Meneghini, M., et al., A combined electro-optical method for the determination of the recombination parameters in InGaN-based light-emitting diodes. Journal of Applied Physics, 2009. **106**(11): p. 114508.
80. Fiorentini, V., F. Bernardini, and O. Ambacher, Evidence for nonlinear macroscopic polarization in III–V nitride alloy heterostructures. Applied physics letters, 2002. **80**(7): p. 1204-1206.
81. Zhu, C., et al., Negative capacitance in light-emitting devices. Solid-State Electronics, 2009. **53**(3): p. 324-328.
82. Xia, Y., et al. Discrete steps in the capacitance-voltage characteristics of GaInN/GaN light emitting diode structures. in MRS Proceedings. 2004. Cambridge Univ Press.
83. Xi, Y. and E. Schubert, Junction-temperature measurement in GaN ultraviolet light-emitting diodes using diode forward voltage method. Applied Physics Letters, 2004. **85**(12): p. 2163-2165.

84. Xi, Y., et al., Junction temperature in ultraviolet light-emitting diodes. Japanese journal of applied physics, 2005. **44**(10R): p. 7260.
85. Nakamura, S., the blue laser diode.
86. Morkoc¸, H., Handbook of Nitride
Semiconductors and Devices. 2009. **3**.
87. Guo, X. and E.F. Schubert, Current crowding and optical saturation effects in GaInN/GaN light-emitting diodes grown on insulating substrates. Applied Physics Letters, 2001. **78**(21): p. 3337-3339.
88. LIM WOON CHI, J., Metal contacts to P-type gallium nitride. 2006.
89. Horng, R.-H., et al., Low-resistance and high-transparency Ni/indium tin oxide ohmic contacts to p-type GaN. Applied Physics Letters, 2001. **79**(18): p. 2925-2927.
90. Ju, I., et al., High-Power GaN-Based Light-Emitting Diodes Using Thermally Stable and Highly Reflective Nano-Scaled Ni–Ag–Ni–Au Mirror. Photonics Technology Letters, IEEE, 2011. **23**(22): p. 1685-1687.
91. Sang Kim, K., M. Gyun Suh, and S. Cho, Nanometer sized Ni-dot/Ag/Pt structure for high reflectance of p-type contact metal in InGaN light emitting diodes. Applied Physics Letters, 2012. **100**(6): p. 061113-1--061113-3.
92. Chang, L.-B., C.-C. Shiue, and M.-J. Jeng, Formation process of high reflective Ni⁄Ag⁄Au Ohmic contact for GaN flip-chip light-emitting diodes. Applied physics letters, 2007. **90**(16): p. 163515-1--163515-3.
93. Chang, L.-B., C.-C. Shiue, and M.-J. Jeng, High reflective p-GaN/Ni/Ag/Ti/Au Ohmic contacts for flip-chip light-emitting diode (FCLED) applications. Applied Surface Science, 2009. **255**(12): p. 6155-6158.
94. Kim, J.-Y., J.-M. Lee, and M.-K. Kwon, Formation of Low Resistance and High Reflectivity Reflector on p-Type GaN Using Ni/Au/W/Ag Ohmic Contact. Electrochemical and Solid-State Letters, 2012. **15**(6): p. H198-H201.
95. Jang, H.W. and J.-L. Lee, Low-resistance and high-reflectance Ni/Ag/Ru/Ni/Au ohmic contact on p-type GaN. Applied physics letters, 2004. **85**(19): p. 4421-4423.
96. Lee, J.-R., et al., Low resistance and high reflectance Pt/Rh contacts to p-type GaN for GaN-based flip chip light-emitting diodes. Journal of The Electrochemical Society, 2005. **152**(1): p. G92-G94.

97. Sheu, J., et al., High-transparency Ni/Au ohmic contact to p-type GaN. Applied physics letters, 1999. **74**(16): p. 2340-2342.
98. Son, J.H., et al., Effects of Ni cladding layers on suppression of Ag agglomeration in Ag-based Ohmic contacts on p-GaN. Applied Physics Letters, 2009. **95**(6): p. 062108-1--062108-03.
99. Wang, Y., et al., Effects of annealing and impurities on tensile properties of electrodeposited nanocrystalline Ni. Scripta materialia, 2004. **51**(11): p. 1023-1028.
100. Song, J.O., et al., Improvement of the luminous intensity of light-emitting diodes by using highly transparent Ag-indium tin oxide p-type ohmic contacts. IEEE Photonics Technology Letters, 2005. **17**(2): p. 291-293.
101. Hibbard, D., et al., Low resistance high reflectance contacts to p-GaN using oxidized Ni/Au and Al or Ag. Applied physics letters, 2003. **83**(2): p. 311-313.
102. Kim, J.-Y., et al., Thermally stable and highly reflective AgAl alloy for enhancing light extraction efficiency in GaN light-emitting diodes. Applied physics letters, 2006. **88**(4): p. 043507.
103. Minami, T., et al., Physics of very thin ITO conducting films with high transparency prepared by DC magnetron sputtering. Thin Solid Films, 1995. **270**(1): p. 37-42.
104. Kim, S., Effect of Interfacial properties of p-GaN/sputter-deposited NiAg-based electrode on optical properties of vertical GaN-based LEDs. Electrochemical and Solid-State Letters, 2009. **12**(12): p. H441-H444.
105. Uang, K.-M., et al., The use of transparent indium–zinc oxide/(oxidized-Ni/Au) ohmic contact to GaN-based light-emitting diodes for light output improvement. Thin solid films, 2006. **515**(4): p. 2501-2506.
106. Jie-Jun, W., et al., GaN substrate and GaN homo-epitaxy for LEDs: Progress and challenges. Chinese Physics B, 2015. **24**(6): p. 068106.
107. Yum, W.-S., et al., Highly reliable Ag/Zn/Ag ohmic reflector for high-power GaN-based vertical light-emitting diode. Optics express, 2012. **20**(17): p. 19194-19199.
108. Song, J.-O., et al., Ohmic and degradation mechanisms of Ag contacts on p-type GaN. Applied Physics Letters, 2005. **86**(6): p. 062104.
109. Kim, D., et al., A study of transparent indium tin oxide (ITO) contact to p-GaN. Thin Solid Films, 2001. **398**: p. 87-92.

110. Ganteför, G., et al., Photoelectron spectroscopy of silver and palladium cluster anions. Electron delocalization versus, localization. Journal of the Chemical Society, Faraday Transactions, 1990. **86**(13): p. 2483-2488.
111. Jang, J.-S., et al., Low-resistance Pt/Ni/Au ohmic contacts to p-type GaN. Applied physics letters, 1999. **74**(1): p. 70.
112. Hashizume, T., Effects of Mg accumulation on chemical and electronic properties of Mg-doped p-type GaN surface. Journal of applied physics, 2003. **94**(1): p. 431-436.
113. https://en.wikipedia.org/wiki/Metalorganic_vapour_phase_epitaxy#III-V_semiconductors.
114. Kim, M.-H., et al., Origin of efficiency droop in GaN-based light-emitting diodes. Applied Physics Letters, 2007. **91**(18): p. 183507.
115. Cingolani, R., et al., Spontaneous polarization and piezoelectric field in G a N/A l 0.15 Ga 0.85 N quantum wells: Impact on the optical spectra. Physical Review B, 2000. **61**(4): p. 2711.
116. Li, Y.-L., Y.-R. Huang, and Y.-H. Lai, Efficiency droop behaviors of InGaN∕ GaN multiple-quantum-well light-emitting diodes with varying quantum well thickness. Applied Physics Letters, 2007. **91**(18): p. 181113.
117. Ling, S.-C., et al., Low efficiency droop in blue-green m-plane InGaN/GaN light emitting diodes. Applied Physics Letters, 2010. **96**(23): p. 231101-231101-3.
118. Cao, X., et al., Blue and near-ultraviolet light-emitting diodes on free-standing GaN substrates. Applied physics letters, 2004. **84**(21): p. 4313-4315.
119. Cao, X., et al., Electrical characteristics of InGaN∕ GaN light-emitting diodes grown on GaN and sapphire substrates. Applied physics letters, 2004. **85**(1): p. 7-9.
120. Motoki, K., et al., Preparation of large freestanding GaN substrates by hydride vapor phase epitaxy using GaAs as a starting substrate. Japanese Journal of Applied Physics, 2001. **40**(2B): p. L140.
121. Beaumont, B., P. Vennéguès, and P. Gibart, Epitaxial lateral overgrowth of GaN. physica status solidi (b), 2001. **227**(1): p. 1-43.
122. Kato, Y., et al., Selective growth of wurtzite GaN and AlxGa1− xN on GaN/sapphire substrates by metalorganic vapor phase epitaxy. Journal of crystal growth, 1994. **144**(3-4): p. 133-140.

123. Iveland, J., et al., Direct Measurement of Auger Electrons Emitted from a Semiconductor Light-Emitting Diode under Electrical Injection: Identification of the Dominant Mechanism for Efficiency Droop. Physical review letters, 2013. **110**(17): p. 177406.
124. Schubert, M.F. and E.F. Schubert, Effect of heterointerface polarization charges and well width upon capture and dwell time for electrons and holes above GaInN/GaN quantum wells. Applied Physics Letters, 2010. **96**(13): p. 131102-131102-3.
125. Ryu, H.-Y. and J.-I. Shim, Effect of current spreading on the efficiency droop of InGaN light-emitting diodes. Optics express, 2011. **19**(4): p. 2886-2894.
126. Jung, B.O., et al., Morphology development of GaN nanowires using a pulsed-mode MOCVD growth technique. CrystEngComm, 2014. **16**(11): p. 2273-2282.
127. Lin, Y.-T., T.-W. Yeh, and P.D. Dapkus, Mechanism of selective area growth of GaN nanorods by pulsed mode metalorganic chemical vapor deposition. Nanotechnology, 2012. **23**(46): p. 465601.
128. Rishinaramangalam, A.K., et al., Controlled Growth of Ordered III-Nitride Core–Shell Nanostructure Arrays for Visible Optoelectronic Devices. Journal of Electronic Materials, 2015. **44**(5): p. 1255-1262.
129. Marchand, H., et al., Mechanisms of lateral epitaxial overgrowth of gallium nitride by metalorganic chemical vapor deposition. Journal of Crystal Growth, 1998. **195**(1): p. 328-332.
130. Hiramatsu, K., et al., Fabrication and characterization of low defect density GaN using facet-controlled epitaxial lateral overgrowth (FACELO). Journal of Crystal Growth, 2000. **221**(1): p. 316-326.
131. Tian, Y., et al., Direct growth of freestanding GaN on C-face SiC by HVPE. Scientific reports, 2015. **5**.
132. Davydov, V.Y., et al., Raman and photoluminescence studies of biaxial strain in GaN epitaxial layers grown on 6H–SiC. Journal of applied physics, 1997. **82**(10): p. 5097-5102.
133. Davydov, V.Y., et al., Phonon dispersion and Raman scattering in hexagonal GaN and AlN. Physical Review B, 1998. **58**(19): p. 12899.

134. Tripathy, S., et al., MicroRaman investigation of strain in GaN and AlxGa1− xN/GaN heterostructures grown on Si (111). Journal of applied physics, 2002. **92**(7): p. 3503-3510.
135. Zhao, D., et al., Stress and its effect on optical properties of GaN epilayers grown on Si (111), 6H-SiC (0001), and c-plane sapphire. Applied physics letters, 2003. **83**(4): p. 677-679.
136. Hushur, A., M.H. Manghnani, and J. Narayan, Raman studies of GaN/sapphire thin film heterostructures. Journal of Applied Physics, 2009. **106**(5): p. 54317.
137. Liu, Q., et al., Local stress analysis of epitaxial laterally-overgrown GaN. Japanese Journal of Applied Physics, 2000. **39**(10A): p. L958.
138. Liu, Q., et al., Stress analysis of selective epitaxial growth of GaN. Applied physics letters, 1999. **74**(21): p. 3122-3124.
139. Cremades, A., et al., Structural and optical properties of Si-doped GaN. Physical Review B, 2000. **61**(4): p. 2812.
140. Sedrine, N.B., et al., Photoluminescence studies of a perceived white light emission from a monolithic InGaN/GaN quantum well structure. Scientific reports, 2015. **5**.
141. Corfdir, P., et al., Exciton localization on basal stacking faults in a-plane epitaxial lateral overgrown GaN grown by hydride vapor phase epitaxy. Journal of Applied Physics, 2009. **105**(EPFL-ARTICLE-174834): p. 043102.
142. Häberlen, M., et al., Low temperature photoluminescence and cathodoluminescence studies of nonpolar GaN grown using epitaxial lateral overgrowth. Journal of Applied Physics, 2010. **108**(3): p. 033523.
143. Scholz, F., et al., GaInN-based LED structures on selectively grown semi-polar crystal facets. physica status solidi (a), 2010. **207**(6): p. 1407-1413.
144. Strittmatter, A., et al., Semi-polar nitride surfaces and heterostructures. physica status solidi (b), 2011. **248**(3): p. 561-573.
145. Gühne, T., et al., Cathodoluminescence spectroscopy of epitaxial-lateral-overgrown nonpolar (11-20) and semipolar (11-22) GaN in relation to microstructural characterization. Journal of applied physics, 2007. **101**(11): p. 113101.
146. Yang, G., et al., White-light emission from InGaN/GaN quantum well microrings grown by selective area epitaxy. Photonics Research, 2016. **4**(1): p. 17-20.

147. Rishinaramangalam, A.K., et al., Semipolar InGaN/GaN nanostructure light-emitting diodes on c-plane sapphire. Applied Physics Express, 2016. **9**(3): p. 032101.
148. Zhang, Z.-H., et al., On the origin of the electron blocking effect by an n-type AlGaN electron blocking layer. Applied Physics Letters, 2014. **104**(7): p. 073511.
149. MOCVD, CVD & ALD PRECURSORS.
150. Seshan, K., Handbook of thin film deposition. 2012: William Andrew.
151. Koleske, D.D., et al., Influence of MOVPE growth conditions on carbon and silicon concentrations in GaN. Journal of Crystal Growth, 2002. **242**(1): p. 55-69.
152. Neumayer, D.A. and J.G. Ekerdt, Growth of Group III Nitrides. A Review of Precursors and Techniques. Chemistry of Materials, 1996. **8**(1): p. 9-25.
153. Eliashevich, I., et al. InGaN blue light-emitting diodes with optimized n-GaN layer. in Optoelectronics' 99-Integrated Optoelectronic Devices. 1999. International Society for Optics and Photonics.
154. Xing, G. and Y.Z. Zhen, Selection of precursors and their influences on III-nitrides grown by MOCVD. Journal of Microwaves, Optoelectronics and Electromagnetic Applications (JMOe), 2002. **2**(5): p. 1-16.
155. Ohba, Y. and A. Hatano, A study on strong memory effects for Mg doping in GaN metalorganic chemical vapor deposition. Journal of Crystal growth, 1994. **145**(1): p. 214-218.
156. Piner, E., et al., Effect of hydrogen on the indium incorporation in InGaN epitaxial films. Applied physics letters, 1997. **70**(4): p. 461-463.
157. System Manual 3x2FT system.
158. http://www.aixtron.com/en/products/technologies/.
159. http://cnx.org/content/m25614/latest/#id9420398.
160. DenBaars, S.P., Gallium nitride materials technology. High-Temperature Electronics in Europe, 2000: p. 23.
161. AIXTRON LTD. MULTI-WAFER INTERFEROMETER.
162. https://en.wikipedia.org/wiki/Scanning_electron_microscope.
163. https://en.wikipedia.org/wiki/Atomic-force_microscopy.
164. Prall, C., et al., Photoluminescence from GaN layers at high temperatures as a candidate for in situ monitoring in MOVPE. Journal of Crystal Growth, 2014. **397**: p. 24-28.

165. Benyoucef, M., et al., Raman mapping, photoluminescence investigations, and finite element analysis of epitaxial lateral overgrown GaN on silicon substrates. Applied physics letters, 2002. **80**(13): p. 2275-2277.
166. Freitas Jr, J., et al., Growth of High Crystalline Quality HVPE-GaN Crystals with Controlled Electrical Properties. Crystal Growth & Design, 2015. **15**(10): p. 4837-4842.
167. http://www.chem.qmul.ac.uk/surfaces/scc/scat5_5.htm.
168. https://en.wikipedia.org/wiki/Secondary_ion_mass_spectrometry.
169. https://en.wikipedia.org/wiki/X-ray_photoelectron_spectroscopy.
170. http://xpssimplified.com/whatisxps.php.
171. Watts, J., X-ray photoelectron spectroscopy. Vacuum, 1994. **45**(6): p. 653-671.
172. Piprek, J., GaN-based Devices: Physics and Simulation. NUSOD 06 Tutorial MA2, 2006.
173. Inc., C.S., Crosslight Device Simulation Software -General Manual. 2010.